Selected Topics of Semiconductor Physics and Technology

Ausgewählte Probleme der Halbleiterphysik und Technologie

Vol. 130

Jia Chen

Compact laser-spectroscopic gas sensors using Vertical-Cavity Surface-Emitting Lasers

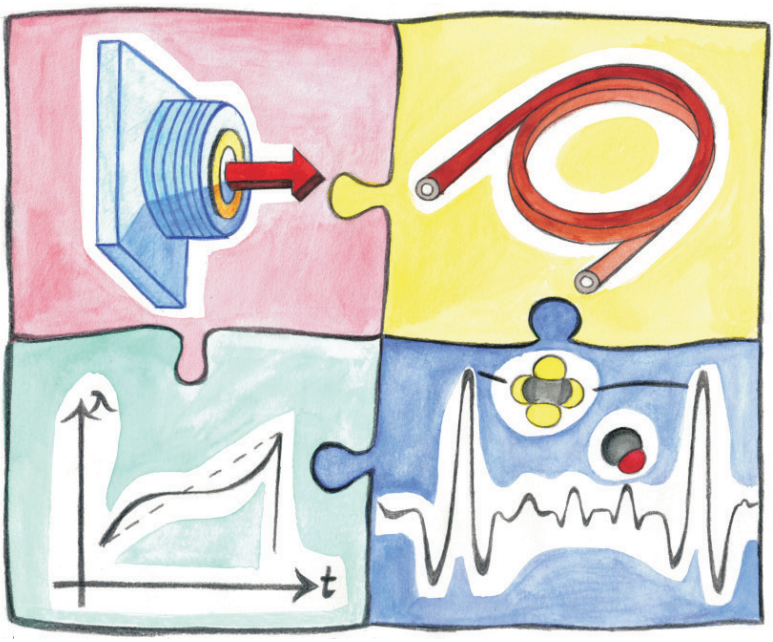

Editors:

G. Abstreiter, M.-C. Amann, M. Stutzmann, P. Vogl

Walter Schottky Institut, Technische Universität München

1. Auflage Juni 2011

Titelbild: The picture shows the essential components of the sensors developed in this thesis (from left to right, top to bottom): light source: vertical-cavity surface-emitting laser; optical gas cell: hollow capillary fiber; spectral sampling: nonlinear wavelength scanning and signal processing: harmonic spectrum of CO and CH_4 at 2.3655 µm wavelength.

Druck: Printy Digitaldruck, München (http://www.printy.de)

ISBN: 978-3-941650-30-5

Contents

1 Introduction

This dissertation is about laser spectroscopic gas sensing. One might ask why is gas sensing important and what information is correlated with the gas concentration? We are surrounded by a variety of gases, in daily life and in industrial processes. For example, persons sitting in a small closed room will very soon start become tired. One of the reasons for this is the build-up of a high concentration of carbon dioxide which causes their tiredness. The carbon dioxide concentration in the exhalation of a person (50,000 ppm) is 100 times stronger than the usual concentration of carbon dioxide in ambient air (400-600 ppm). In this case, the comfort of a person is correlated with the carbon dioxide concentration. Also, many gases are poisonous, therefore their concentration has to be monitored in workplace environments where these gases are worked with. The presence of carbon monoxide may also indicate a dangerous fire situation. For fire detection, carbon monoxide monitoring is a much better method than optical particle/smoke detection, because the latter does not distinguish between real smoke and false readings from insects or hair spray for example, thus producing high false alarm rates. At airports up to 50 % of all alarms are false alarms. Moreover, gases exhaled by a person can indicate his or her health condition. A prominent example is nitrogen oxide, which is an early indication for an asthma attack. Furthermore, the concentration information of exhaust gases e.g. CO, NO, O_2, CH_4 can help for process optimization, saving of energy and reduction of pollutants emission. The lambda probe is a mature technology used in the vehicle industries aimed at measuring the contents of exhaust gases. But better solutions have yet to be found to look at the exhausts from medium or small scale burners, for example those found in domestic heating appliances.

All in all, the knowledge of the gas concentrations can increase our comfort and protect us from poisoning and fire. It enables detection of diseases and efficient process control in industrial production. Gas sensors are therefore in widespread use everywhere: in office buildings, in households, and in industry. The techniques that are used are catalytic combustion types [1], electro-chemical cell [2] and metal oxide based sensors [3], which are cost-efficient, but suffer long-term stability problems and/or cross-sensitivity to other gases. Equipments using optical measurement principles are based on non-dispersive infrared spectroscopy. However, these techniques are not calibration-free. Among all the techniques for gas concentration measurement, tunable diode laser spectroscopy (TDLS) exhibits unique and excellent properties, like long term stability, inherent self monitoring and lowest possible cross-sensitivity to other gases. TDLS is developed over the last decades in parallel with progression of diode laser technology, which was basically driven by the optical communication technology.

The existing TDLAS analyzing equipments have the following applications:

- Process control in power plants, waste incinerators and emission monitoring. The companies offer these equipments are e.g. Norsk Electro Optikk, AS (Norway), Unisearch Associates Inc. (Canada) and Siemens Laser Analytics (Sweden).

- Measurement of isotopic composition in stable compounds. The companies are for example Picarro, who use cavity ring down spectroscopy and Aerodyne research, who use direct spectroscopy with multipass cell [4].

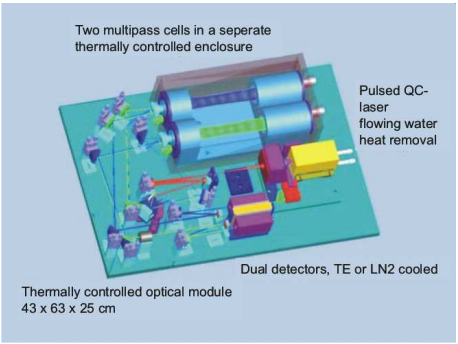

Fig. 1.1: An example for existing TDLAS equipment: isotopic composition measurement from Aerodyne research [5], which contains reference cells and many optical elements.

These equipments are large in dimensions, complex and of comparable high cost (Fig. 1.1). Attempts have been made to open a wider market for TDLS with cheaper equipment, e.g. oxygen breath monitoring from company Oxigraf or natural gas leak detection initialized by British Gas. However these attempts have not yet been really successful, partly because the laser diodes are still too expensive, and partly because the sensor design is not optimized towards a minimum number of components. Additional optics are needed for measurement of spectral features originating from the optical cells and the laser itself, and for determination of the wavelength actually scanned. To achieve certain detection sensitivity, large dimension optical cells are needed for long optical pathlength [6]. Also, complicated evaluation algorithms need PC-based computation to fulfill the real-time operation [5]. Possible issues due to laser and detector cooling systems exist especially for the mid-infrared range. These all lead to high-cost and high complexity of the sensor.

The successful development of long wavelength VCSELs [7, 8] during the last years may help to bring this technology into a broader application field. Optical elements can be eliminated and the missing functionality can be implemented by improved signal processing to achieve comparable sensitivity and reliability. Decisive parts of the novel VCSEL-based gas sensor technology are to be developed within this thesis.

The outline of this work is the following: an initial analysis of the problems, followed by an introduction to the fundamentals of the subject of this thesis, then four main chapters about the laser, optical cell, signal evaluation and the whole sensor set-up components. The fourth chapter looks at the suitability for TDLS applications of the VCSEL technology. The question of how fast the laser wavelength can be tuned is to be answered in this section. The fifth chapter looks at how a new design of optical cell is developed and makes a comparison between different optical cells, giving a figure of merit to each. This is followed by an explanation of the development of optimized measurement procedures and signal processing methods. In the seventh chapter, several application examples are given for the optimized sensor design, utilizing the components investigated in the previous chapters. And at the end, the optimized sensor concepts are proved in real applications.

2 Analysis of the requirements for development of an optical gas detector

TDLS exhibits excellent properties for gas sensing, like long term stability, inherent self monitoring and lowest possible cross-sensitivity to other gases. These properties predestine this method for a range of applications where highest reliability is demanded, e.g. in aviation and medical engineering. The successful development of VCSELs during the last years may help to bring this technology into broader application fields. These lasers have a significant advantage compared to conventional edge-emitters because of their low-cost potential and low power consumption. Decisive parts of the novel VCSEL-based gas sensor technology are to be developed within this thesis. The goal is to develop miniaturized and low cost TDLS sensors. To achieve this, one has

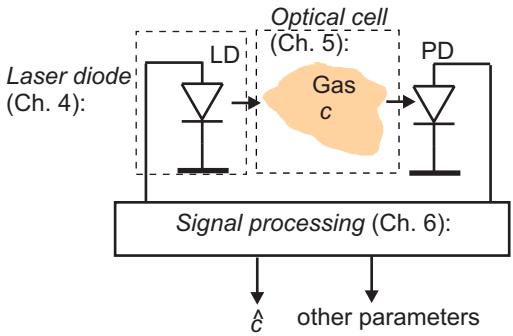

Fig. 2.1: Schematical overview of a sensor system. The three basic components are laser diode, gas cell and signal processing.

to understand the difficulties and challenges of building a laser-spectroscopic sensor. TDLS is a method for gas concentration determination by measuring gas absorption lines with high resolution. However, distortions always occur during the measurement process, including noise and unwanted spectral features. The conventional method for eliminating noise is averaging, but averaging will always result in time delay of the measurements. Therefore, there is a trade-off between sensing accuracy and response time. Also deterministic spectral features may exist, which cause errors and can not be removed by averaging. These can originate e.g. from multi-mode propagation in the gas cell geometry. The gas cell is a container needed for the interaction between light and gas. Usually a gas cell is constructed by optical elements like mirrors, lenses and windows. However, these elements can cause multi-mode propagation via physical effects like unwanted back-reflections or scattering. This multi-mode propagation then causes additional spectral features that distort the measurement of the gas spectrum ('cell background'). Since 10^{-5} absorbance should be resolved in a low-cost sensor, the demand on suppression of 'cell background' is very high. Anti-reflection (AR) coatings on optical surfaces alone are usually not sufficient. The traditional way of compensat-

ing these residual interferences in the measured spectra is to measure the background when the gas cell is purged with nitrogen and subsequent subtraction of it from the gas spectra [9]. This, however, is unsuitable for miniaturized sensors because it requires a very complex setup and also a continuous supply of non-absorbing gas such as nitrogen. Furthermore, the dead-times significantly limit the application areas of the sensor. In this thesis, other methods to avoid or compensate the background have to be developed. For this, the 'cell background' has to be investigated and analyzed in detail (Chap. 5).

One additional problem is the cell transparency. In harsh conditions, the cell could have low transmission due to contamination and only a small fraction of the light is detected. The detector noise is then a bigger proportion of the measured absorption signal and the signal-to-noise ratio decreases. Therefore, means to avoid this have to be developed, for example by using a diffuse reflector intended to be robust against thermal cycles. Also movement of waterdrops in a condensing environment may give an additional intensity noise that could further lower the signal-to-noise ratio. This all has to be characterized and examined in this thesis (Chap. 5).

Another difficulty is to achieve high sensitivity with miniaturized sensor design. Usually, short interaction length is provided by the compact single-reflective cells. Conventional multipass cells are very sensitive to alignment and require large sample volume. Hence alternatives are needed to realize the efficacy of such compact and sensitive sensors. New developments of gas-permeable fibers could provide for such a solution by using in-fiber gas sensing. But the difficulties are again the spectral background caused by the fiber itself and a possibly large gas exchanging time due to the small inner diameter of the fiber. These issues are examined and a solution is provided in Chap. 5.

A tunable laser is required for TDLS. A large tuning range of laser wavelength is very important. However, if the tuning speed is too fast, the laser wavelength may not follow instantaneously, because wavelength tuning is caused by a self-heating effect inside the laser. Therefore, it is important to know what is the speed limitation of the VCSEL wavelength tuning. If tuning does not immediately follow current, the scanned wavelength can not be predicted reliably. The measured spectrum may have distorted shape and the gas parameters can not be extracted. Furthermore, the laser aging problem gives uncertainty of the long-term operation of the sensor. The laser parameters like the linear-nonlinear current-to-wavelength tuning coefficient could vary during time. Ideally the sensor operation should not depend on these parameters. It would be ideal to develop a spectroscopic operation mode that allows for continuously monitoring of these parameters. Finally, there are spectral features caused by the laser diode itself ('laser background'), which has also to be understood and eliminated if possible (Chap. 4).

When the gas absorption spectrum is measured with required accuracy, the next question is how to extract the gas parameters from it. Since the new sensor should be reliable, miniaturized and have low power consumption, limited numerical calculation effort, but still reliable algorithms are required. Again as mentioned before, the measured spectrum is superimposed with noise, which has to be removed as much as possible using optimized signal processing. This is not straightforward, because conventional lowpass or bandpass filtering will also distort the measured spectrum if it should effectively remove noise. To overcome this, a more sophisticated signal-model, i.e. a description of the measured signals including noise has to be developed. Another difficulty is to find out the wavelength scale of the measured spectrum. If wavelength is known, the theoretical spectrum can be calculated with data from the HITRAN data

base [10]. However, the laser current and not laser wavelength is directly controlled. Conventionally, to find out the scanned wavelength, a reference etalon or external gas reference cell is used, which again increases the sensor complexity. One task of the work is to find methods sparing the extra reference etalon and the additional reference cell and extract all the parameters out of the measured spectrum (Chap. 6).

All in all, an important question is, what is theoretically the overall best sensing resolution achievable at a given optical pathlength and detection wavelength. Knowing this, all sensor implementations using a certain signal-processing and spectroscopic method could be compared with this optimum value. This would be very useful in finding limitations of existing designs and methods and may direct future research in the right direction. Furthermore, the best spectroscopic method may be found.

The problems can be grouped into three categories: laser diode (Chap. 4), optical cell (Chap. 5) and signal processing (Chap. 6).

3 Fundamentals

Laser spectroscopy determines the gas concentration by measuring gas absorption line. The gas properties such as composition, concentration, pressure and temperature are all encrypted in the spectrum. Using a monochromatic light source like a laser, the spectral features are recorded with high spectral resolution and then later analyzed. Each gas molecule has many absorption bands. The wavelength position and strength of different absorption bands of the different molecules in the near and mid-infrared range are shown in Fig. 3.1. The y-axis denotes the gas concentration where at 1 m path length a 10^{-5} absorbance is achieved. It is an indication for the strongest line in an absorption band. For the same molecule, the linestrength in the infrared range is typically higher at longer wavelength. For example for CO molecules, the absorption at 2.3 μm is 160 times stronger than the absorption at 1.5 μm (see Fig. 3.1).

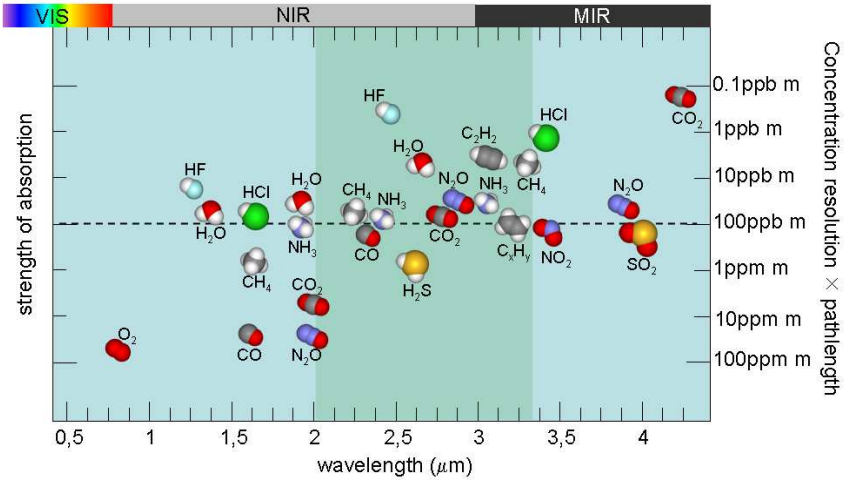

Fig. 3.1: The schematical figure of the absorption bands of the different molecules in the near and mid-infrared range (provided by A. Hangauer, data taken from [10]). The y-axis is the achievable concentration resolution that corresponds to 1 m path length and 10^{-5} absorbance resolution.

In the following, the physical reasons behind the observed absorption bands are explained and techniques for measuring the absorption spectrum as well as the laser diodes used are outlined and compared.

3.1 Absorption by molecules

Absorption and emission are correlated with transition between different states of a gas molecule. A photon enables an energy transition of a gas molecule to a higher energy level, which is called absorption. By deexcitation of a molecule, either photons are emitted ('fluorescence') or heat is generated when the deexcitation is caused by a molecule collision. A photon of wavelength λ, wavenumber ν or frequency f can only be absorbed, when a gas molecule has states i, j with energy levels E_i and E_j,

$$E_j - E_i = h\,f = \frac{h\,c}{\lambda} = h\,c\,\nu \tag{3.1}$$

and the molecule is in the 'lower state' i. Here h denotes the Planck constant and c the speed of light. Different gas molecules have different energy levels and therefore fundamentally different energy transitions are observed. Therefore, absorption lines are very characteristical for a special gas molecule. The different types of energy transitions as well as the physical reasons behind are discussed in the following sections.

3.1.1 Energy transitions of molecules

For molecules, there are general three classes for energy transitions shown in Fig. 3.2: coupled electron-vibration-rotation transitions (visible and ultra-violet range), rotation-vibration transitions (near infrared range and mid-infrared range) and rotational only transitions (far-infrared and radio frequency range).

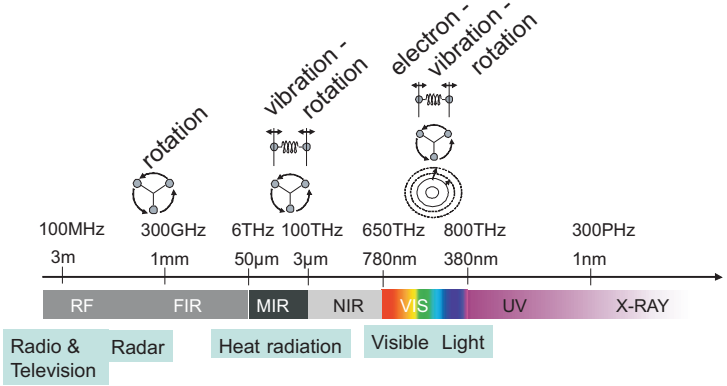

Fig. 3.2: Correlation between part of electro-magnetic spectrum and the type of molecular transition.

Electron transition

The passage of an electron in an atom or molecule from one energy state to another state (e.g. orbital change) is called electron transition. An electronic transition is accompanied by the emission or absorption of energy corresponding to the difference in energy between the two states. The energy difference is in the range of several eV up to the ionization energy, which corresponds to wavelength in the visible and UV range

[11]. Electron transition occur in conjunction with vibrational/rotational transitions, which is called 'Rovibronic coupling'. Single atoms only have electronic transitions, they do not have vibrational or rotational states.

Vibrational transition

A vibrational transition is a change in vibrational energy of the atoms of a gas molecule. The energies are in the range of several 100 meV up to the dissociation energy of the molecule [11]. To determine the vibration states of a two-atom gas molecule e.g carbon monoxide, the molecule can be approximately described with a harmonic oscillator model [11]. There the one-dimensional Schrödinger equation is solved with assuming parabolic energy potential $V(x) = \frac{1}{2}kx^2$ for approximation of the intermolecular potential. Then the following energy states are obtained:

$$E_v = \frac{h\sqrt{k}}{2\pi\sqrt{m}}(\nu + 1/2) \qquad \nu = 0, 1, \ldots \tag{3.2}$$

with k being a spring constant describing the intermolecular force. m is the reduced mass of C and O atoms, which is effectively given when the atoms are oscillating:

$$m = \frac{m_C\, m_O}{m_C + m_O} \tag{3.3}$$

This model is valid for molecules with two atoms and low vibrational excitation. In this case, the energy state is approximately linear to the state number, which means that the vibrational bands have a constant spectral frequency spacing. For higher energy states the parabolic approximation to the interatomar potential is no longer valid and deviations in the experimentally observed spectra and the prediction with the discrete state harmonic oscillator are obtained.

(a) Rotation of a carbon monoxide molecule.

(b) Vibration of a carbon monoxide molecule.

Fig. 3.3: Schematic illustration of vibration and rotation states of a carbon monoxide molecule. Vibrational states are approximately obtained by applying a discrete harmonic oscillator model. Unlike a classical harmonic oscillator, these only take discrete energies. Rotational states are obtained by using a rigid rotator model.

Rotational transition

A rotational transition is a change in angular momentum of a gas molecule. The most simple model that qualitatively describes the observed spectra is the rigid rotator model [11]. There the distance of the two atoms is considered to be independent on the rotation level. In order to determine the possible energy states of this rigid rotator, the Schrödinger equation is solved with the substitution potential energy $V = 0$ and reduced mass m of C and O atoms. The first assumption is made because the rotator is

considered rigid and no potential energy is associated with the rotator. The Schrödinger equation appropriate to this problem is therefore:

$$\frac{\mathrm{d}^2\Psi}{\mathrm{d}x^2} + \frac{\mathrm{d}^2\Psi}{\mathrm{d}y^2} + \frac{\mathrm{d}^2\Psi}{\mathrm{d}z^2} + \frac{8\,\pi^2\,m}{h^2}\,E\,\Psi = 0 \tag{3.4}$$

where $x^2 + y^2 + z^2 = r_0^2$ is a constant and r_0 the distance between the C and O atom. The solution of the Schrödinger equation is given by:

$$E_j = \frac{h^2}{8\,\pi^2\,I}\,j\,(j+1) \qquad\qquad j = 0, 1, 2, \ldots \tag{3.5}$$

with the moment of inertia I:

$$I = m\,r_0^2 \tag{3.6}$$

The corresponding wavefunctions $|\Psi_{j,\mu}(x, y, z)|^2$, $\mu = -j, .., j$ give the probability distribution of the rotator on the sphere with radius r_0. It clearly can be seen in Eq. (3.5), that the discrete energy state increases quadratically with quantum number j.

Combined vibration-rotation transitions of carbon monoxide molecules

Generally, vibrational transitions occur in conjunction with rotational transitions, which is called 'Rovibrational coupling'. In Fig. 3.4(a), the vibrational states of carbon monoxide are denoted with the symbols ν_0, ν_1, ..., corresponding to Eq. (3.2) with $\nu = 0, 1, \ldots$. The rotational states are superimposed with the vibrational states, whereas the energy difference between rotational states is usually much smaller than the vibrational state differences. The fundamental band is formed by the most probable transition $\nu_0 \rightarrow \nu_1$ (@ 4.6 μm) [10, 11, 12]. The first overtone band of carbon monoxide is the transition $\nu_0 \rightarrow \nu_2$ (@ 2.3 μm). At this wavelength also the other bands $\nu_1 \rightarrow \nu_3$, $\nu_2 \rightarrow \nu_4$, ... are present. Which one is dominating in the spectrum is strongly dependent on the number of molecules in the corresponding upper and lower states, which in turn strongly depends on temperature. At room temperature usually only the fundamental vibrational state is occupied, so the transition $\nu_0 \rightarrow \nu_2$ is dominating.

The different lines in one vibrational band, e.g. $\nu_0 \rightarrow \nu_2$ are formed by different rotational transitions additional to the vibrational transition. These lines are also called "rotational fine structure" (Fig. 3.4(b)) [11]. The absorption band of CO has two branches: the P and R branch. Transitions in the P branch correspond to rotational transitions $\Delta j = -1$ and those in the R branch correspond to $\Delta j = 1$ (Fig. 3.4(a)). Other values of Δj are not allowed, i.e. have a transition probability of zero. Which values are allowed is dependent on the molecule specific 'selection-rules'. In some diatomic molecules like NO also a Q-branch exists, which contains $\Delta j = 0$ transitions [10]. The Q-branch is visible as large peak in between the R and P branch in the spectrum. It is large because all Q-transitions have approximately the same energy difference and are thus overlapping.

For an electromagnetic wave to cause a vibrational transition the gas molecules needs to have an electric or magnetic moment. Otherwise the molecule would be not absorbing. Most strong molecular transitions are electric dipole transitions. However, also magnetic dipole or quadrupole transitions exist. Homonuclear diatomic molecules like O_2, N_2, H_2 have due to symmetry no electric dipole moment. They are thus typically not IR active, i.e. have no or extremely weak absorption lines in the infrared. The absorption band of O_2 at 760 nm corresponds to an electronic transition.

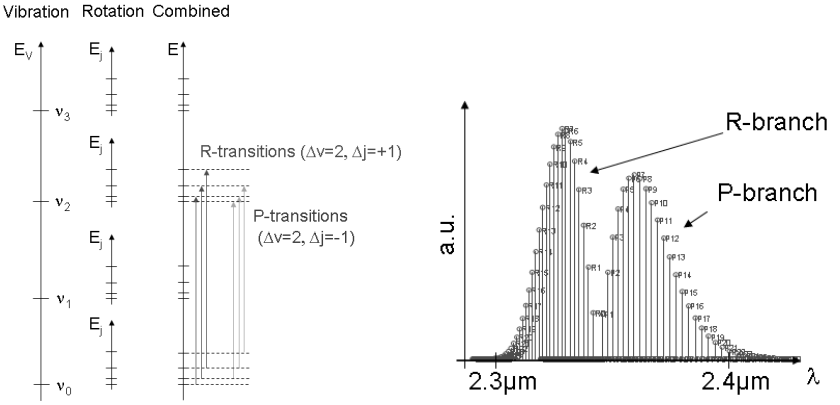

(a) Schema of the energy states of carbon monoxide molecule.

(b) The first overtone absorption band of carbon monoxide molecule.

Fig. 3.4: P branch ($\Delta j = -1$) and R branch ($\Delta j = +1$) by different rotational transitions in addition to the $\nu_0 \rightarrow \nu_2$ vibrational transition of the CO molecule.

The mathematical description of a single gas absorption transition line is given in the next section.

3.1.2 Lambert-Beer law

The gas transmission $T(\nu)$ for an optical path length l is described by the Lambert-Beer law [12]:

$$T(\nu) = e^{-\alpha(\nu)\,c\,l} = e^{-\sigma(\nu)\,n\,l} \tag{3.7}$$

$$\approx 1 - \alpha(\nu)\,c\,l = 1 - \sigma(\nu)\,n\,l \tag{3.8}$$

with $\alpha(\nu)$ being the wavelength-dependent gas absorption coefficient (unit: cm^{-1}) and $\sigma(\nu)$ (unit: cm^2) the absorption cross-section of the gas species. The concentration (mixing-ratio) is denoted as c and n (unit: $1/\mathrm{cm}^3$) is the number density (number per unit volume) of absorbing particles with $n = cp/(k_B T)$. Here k_B denotes the Boltzmann constant, p the pressure (unit: bar) and T gas temperature (unit: K). The negative logarithm of the transmission $-\log(T(\nu))$ is called absorbance. If the absorbance is very small, i.e. < 0.1, an approximation can be made that transmission is one minus absorbance. The relative error of this approximation is maximal 0.5 %. The approximation enables the linear relationship between the measured transmission $T(\nu)$ and the gas concentration c. $\sigma(\nu)$ can be expressed as the product of line profile $\Phi(\nu)$ with the integral normalized to one and line strength S, i.e.:

$$\sigma(\nu) = S\,\Phi(\nu) \tag{3.9}$$

Line profile $\Phi(\nu)$ and line strength $S = S(T)$ are discussed in the following sections. The absorption coefficient is given as

$$\alpha(\nu) = \sigma(\nu)\frac{p}{k_B T} = \frac{p}{k_B T} S\,\Phi(\nu) \tag{3.10}$$

The peak absorption coefficient α_c is the absorption coefficient at line center ν_c:

$$\alpha_c = \frac{p}{k_B T} S\,\Phi(\nu_c) \tag{3.11}$$

3.1.3 Absorption line width and absorption line profile

Spectral lines in absorption or emission spectra are never strictly monochromatic. Due to the finite lifetime of the states and the principle of energy uncertainty, also photons with slightly different frequency/wavelength can be absorbed. This is one of the reasons for the observed broadening of absorption lines. In the following, different line profiles are described and the corresponding line widths (half-width at half-maximum) are shown.

Conversion between wavelength, frequency and wavenumber To describe a gas spectrum, different units are used such as wavelength, wavenumber and frequency. The relationship between wavelength λ, frequency f and wavenumber ν is:

$$\nu = \frac{1}{\lambda} = \frac{f}{c} \tag{3.12}$$

The speed of light is denoted as c.

The halfwidth is sometimes written in terms of wavelength difference $\Delta\lambda$, or wavenumber difference $\Delta\nu$, or frequency difference Δf. The relationship between the three is the following:

$$\Delta\nu = -\frac{\Delta\lambda}{\lambda^2} = \frac{\Delta f}{c} \tag{3.13}$$

In spectroscopy usually frequency or wavenumber is the more natural unit than wavelength. Frequency difference is often an absolute value and is independent on the center frequency or the medium. However, $\Delta\lambda$ is different for different basis wavelength λ, if Δf is constant. This is also the reason for the typically larger line width in wavelength in the mid-infrared range compared to the near-infrared range.

Natural line profile and line width The 'absorption line' is not a line, but has a certain width [12]. The absorption profile can be obtained from a classical model of a damped harmonic oscillator, which gives a Lorentzian shape, it reads:

$$\Phi_L(\nu) = \frac{\gamma_L/\pi}{\gamma_L^2 + (\nu - \nu_c)^2} \tag{3.14}$$

ν_c is the center wavenumber corresponding to the transition. The line width is given by $\gamma_L = \gamma_{L,\mathrm{nat}}$ (unit: cm^{-1}), which is anti-proportional to the lifetime τ of the energy state [12]:

$$\gamma_{L,\mathrm{nat}} = \frac{\pi}{c\,\tau} \tag{3.15}$$

The lifetime of an energy state is given by the average time after the unperturbed gas molecule goes back to the lower energy state with an emission of a photon.

Doppler broadening (Gaussian profile) Doppler broadening is given when the gas molecules are moving [12]. The gas molecule "sees" another frequency of light because of the Doppler effect. Therefore, the light with higher or lower frequency corresponding to the transition is also absorbed. Since the molecule velocity in x-,y- or z- direction is Gaussian distributed, the Doppler frequency shift is also Gaussian distributed. The Gaussian profile $\Phi_G(\nu)$ thus describes the Doppler broadening, which is given as:

$$\Phi_G(\nu) = \frac{\sqrt{\log(2)}}{\sqrt{\pi}\gamma_G} \exp\left(-\log(2)\frac{(\nu-\nu_c)^2}{\gamma_G^2}\right) \tag{3.16}$$

ν_c is the center wavenumber corresponding to the transition. The halfwidth at half maximum for a Doppler broadened line γ_G (unit: cm^{-1}) is then theoretically derived as:

$$\gamma_G = \nu_c \sqrt{\log(2)\frac{2k_B T}{m\,c^2}} \tag{3.17}$$

with m being the mass of one molecule (unit: kg), k_B the Boltzmann constant and T the gas temperature (unit: K). The lighter the gas molecule and the larger the center wavenumber is, the broader is the line width. Hence, in visible and UV light range the Doppler broadening is much stronger than in the mid-infrared range. Among all stable gas molecules, the hydrogen molecule has the lowest mass and therefore the highest velocity, which results in the broadest linewidth due to Doppler broadening. If required, ν and γ_G can also be converted to wavelength or frequency according to Eq. (3.12).

Pressure broadening (Lorentzian profile) Pressure broadening is given by the finite lifetime of the upper energy state. At normal conditions the lifetime is much shorter than the natural lifetime and determined by collisions between gas molecules. This effect is more dominant if the gas pressure or temperature is higher. In addition to the natural linewidth, pressure broadening has to be included to the Lorentzian profile as well (Eq. (3.14)). The Lorentzian halfwidth is given by the sum of the natural linewidth and an empirical pressure broadening halfwidth. This is proportional to gas pressure p (unit: bar) and has a temperature dependence of T^{ζ} with $\zeta \approx 1/2$:

$$\gamma_L(c,p,T) = \gamma_{L,nat} + \gamma\, p \left(\frac{296K}{T}\right)^{\zeta} \approx \gamma\, p \left(\frac{296K}{T}\right)^{\zeta} \tag{3.18}$$

Practically, the pressure broadening coefficient γ (unit: cm^{-1}/bar) and the exponent ζ is dependent on the transition because it is strongly influenced by collision effects between the molecules. Thus it also depends on the type of the buffer gas or the other gases in the mixture. For air as buffer gas, γ is composed with an air-broadening coefficient γ_{air} and self-broadening coefficient γ_{self} (both unit: cm^{-1}/bar), with gas concentration c as weighting factor:

$$\gamma = \gamma_{air}(1-c) + \gamma_{self}\, c \tag{3.19}$$

Both coefficients are tabulated in HITRAN (High Resolution Transmission) molecular spectroscopic database, which is a database for absorption line parameters [10]. For

gas mixtures with more components and certain mixing-ratios, a completely different broadening behavior may occur. It can be clearly seen, that γ_L also depends on gas concentration c. If the self- and air- broadening coefficients are in the same order of magnitude and $c < 0.01$, the dependency can be neglected, i.e.:

$$\gamma_L(c, p, T) \approx \gamma_L(p, T) = \gamma_{air}\, p \left(\frac{296K}{T}\right)^{\zeta} \tag{3.20}$$

Otherwise, the effect of line broadening or narrowing by increasing gas concentration has also to be considered. Nevertheless, the integrated area of the absorption line is independent on all these broadening effects and proportional to the number density of absorbing molecules n.

Voigt profile If both pressure and Doppler broadening effects are present, the Voigt profile has to be used. That is the convolution of the Gaussian and Lorentzian profile:

$$\Phi_V(\nu) = (\Phi_G * \Phi_L)(\nu) \tag{3.21}$$

Unfortunately, no analytical closed form expression for the Voigt profile exists. An empirical formula for the Voigt half-width with maximum error of 0.02 % is [13]:

$$\gamma_V = 1/2 \left(\gamma_L\, 1.0692 + \sqrt{0.86639\, \gamma_L^2 + 4\, \gamma_G^2}\right) \tag{3.22}$$

Examples are given for absorption of carbon monoxide at 2.3655 μm and absorption of oxygen at 763 nm. As clearly can be seen in Tab. 3.1, line width caused by Doppler broadening for an oxygen absorption line at 763 nm is much higher than for the carbon monoxide absorption line at 2.3 μm because of its larger center wavenumber (Eq. (3.17)). Since the ratio of the Lorentzian and Voigt half-width is nearly one for both cases, it is clear that the Doppler broadening can be neglected for atmospheric pressure. For much lower pressures (millibar range), only the Doppler broadening has to be considered and pressure broadening can be neglected. In a transition region with moderate pressure, the Voigt profile has to be used. The life time τ can also be calculated from the natural linewidth as given in Eq. (3.15). τ is approximately 0.2 s for carbon monoxide, while it is around 4 s for oxygen.

	carbon monoxide @ 2.3 μm	oxygen @ 763 nm
γ_L	1.774 GHz (0.0591 cm^{-1})	1.475 GHz (0.04915 cm^{-1})
γ_G	0.1477 GHz (0.00492 cm^{-1})	0.478 GHz (0.01426 cm^{-1})
γ_V	1.787 GHz (0.0596 cm^{-1})	1.597 GHz (0.05323 cm^{-1})
$\gamma_{L,\text{nat}}$	0.81 Hz (2.7×10^{-11} cm^{-1})	0.04 Hz (1.36×10^{-12} cm^{-1})
γ_L/γ_V	99.3 %	92.3 %

Tab. 3.1: The line width in frequency and wavenumber units of a carbon monoxide and oxygen absorption line at room-temperature and atmospheric pressure. For pressure broadening only air broadening is considered, i.e. $\gamma = \gamma_{air}$.

Linestrength

The temperature dependent line strength S (see Eq. (3.9)) for a transition is given by:

$$S(T) = S(296K)\,\frac{Q(296K)}{Q(T)}\,\frac{\exp(-E_L/(k_B T))}{\exp(-E_L/(k_B 296K))}\,\frac{1-\exp(-h\,c\,\nu_c\,/(k_B T))}{1-\exp(-h\,c\,\nu_c/(k_B 296K))} \tag{3.23}$$

$Q(T)$ is the total internal partition sum for the gas molecule [10], E_L is the lower state energy of the transition and k_B is the Boltzmann constant. This temperature correction represents the fact that the observed absorption cross section $\sigma(\nu)$ is proportional to the probability of a single molecule being in the lower state times the probability that a single molecule is not in the upper state. The number of the gas molecule in lower state is proportional to the Boltzmann factor $\exp(-E_L/(k_B T))$. For lower E_L or higher gas temperature T, there are more gas molecules in the lower state and absorption corresponding to this energy transition is more likely to happen in a large ensemble of molecules. This also corresponds to a stronger observed linestrength S. The characteristic envelope of the CO spectrum shown in Fig. 3.4(b) is basically due this effect.

3.2 Tunable diode laser absorption spectroscopy

Tunable diode laser absorption spectroscopy is a spectroscopic method for gas detection. It is basically distinguished between direct spectroscopy or wavelength modulation spectroscopy, that is using a small sinusoidal wavelength modulation to detect the harmonic component of the spectrum. Other methods include photoacoustic spectroscopy, where the absorbed energy is directly detected by observing pressure waves emitted from the gas. For this method, however, calibration factors like the resonator Q-factor are needed, which can change over time and are especially temperature dependent.

3.2.1 Direct spectroscopy

Direct spectroscopy is schematically shown in Fig. 3.5(a). By ramping of the laser cur-

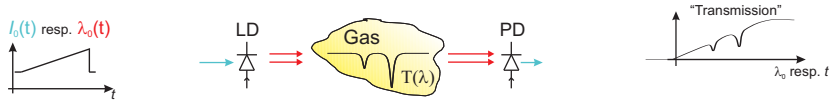

(a) Direct spectroscopy

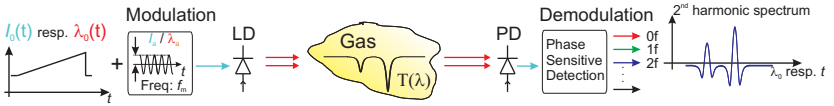

(b) Wavelength modulation spectroscopy (WMS)

Fig. 3.5: The schematical plot of direct spectroscopy and wavelength modulation spectroscopy

rent (or laser chip temperature), the emitting laser wavelength is tuned approximately

linearly. The measured gas absorptions are small dips on the large background resulted by the laser P-I-characteristic. The difficult detection of these dips is also the main drawback of this method.

3.2.2 Wavelength modulation spectroscopy

Wavelength modulation spectroscopy is an established method for sensitive absorbance measurements [14]. This is due to its advantages of efficient noise suppression, i.e. insusceptible to 1/f noise, and removal of the laser amplitude modulation [15] in the measured data. As shown in Fig. 3.5(b), in addition to a slow current (or wavelength) sweep, a small and significantly faster sinusoidal modulation with frequency f_m is applied (typically in the kHz range). The gas absorption converts the frequency modulation to an intensity modulation. Because the gas absorption spectrum is a strongly nonlinear function of wavelength, the resulting amplitude modulation is not sinusoidal any more, but contains harmonic components at multiple of the modulation frequency f_m. Using a lock-in amplifier, the detector signal is decomposed into its harmonic components. The formation of first-/second-harmonic spectrum is schematically shown in Fig. 3.6. The second-harmonic spectrum, i.e. second harmonic component

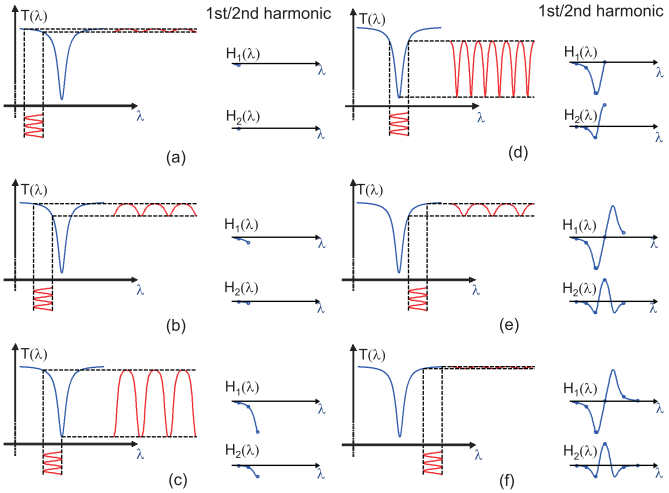

Fig. 3.6: The steps of creation of first-/second-harmonic gas spectrum. Here a constant laser intensity during wavelength tuning is assumed. A sinusoidal wavelength modulation with a shifted bias wavelength is converted to an intensity modulation by the gas absorption line. The intensity modulation is not sinusoidal anymore, but contains higher harmonics. The amplitude of the first and second harmonic of the detector signal are plotted against the bias wavelength, which forms the first- and second-harmonic spectrum.

of the gas absorption is usually used for signal evaluation. Although in theory any harmonic spectrum may be chosen, the influence of the laser AM on the second harmonic spectrum is small enough compared to the first harmonic while the amplitude

of the second harmonic is still relatively large compared to the higher harmonics. The

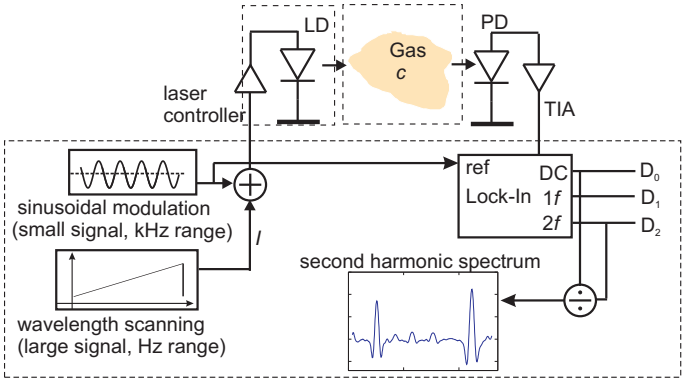

Fig. 3.7: The experimental setup of wavelength modulation spectroscopy

experimental setup of wavelength modulation spectroscopy is shown in Fig. 3.7. In the laboratory, the ramp signal and high frequency sinusoidal modulation are generated by the function generator and the sum of the two are injected to the laser controller, which controls the laser current. The detected intensity of the photodiode is converted into a current and amplified by a trans-impedance amplifier. Lock-In amplifier is a mixer and is used to decompose the detector signal into its harmonic components. To obtain the second-harmonic spectrum, the intensity at $2\,f_m$ is divided by the intensity at DC, so the effect of the varying laser intensity is removed. This is a significant advantage over direct spectroscopy.

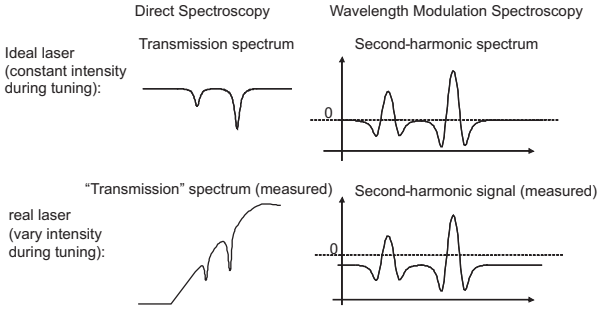

Fig. 3.8: Schematical comparison between direct spectroscopy and wavelength modulation spectroscopy. The non-constant laser intensity during tuning has almost no influence on the harmonic spectrum.

It can clearly be seen in Fig. 3.8, that the measured absorption by direct spectroscopy is a small signal overlapped with a large slope/offset because of the nonlinearity of the laser P-I-characteristic. It is practically difficult to detect a small signal from a large offset. In contrast, the second harmonic spectrum has only a slight negative slope on a small negative offset. This enables a simplified signal processing. A detailed signal

model for the measured spectra is given in section 6.1. The n-th harmonic transmission spectrum is mathematically described by [16]:

$$H_n(\lambda) = \frac{\epsilon_n}{2\pi} \int_{-\pi}^{\pi} T(\lambda + \lambda_a \cos(\theta)) e^{-j\,n\,\theta} d\theta \tag{3.24}$$

with $\epsilon_n = 1$ for $n = 0$ and $\epsilon_n = 2$ for $n > 0$ and λ_a the wavelength modulation amplitude. For the case of unsaturated Lorentzian absorption line (with center wavelength λ_c, peak absorbance $\alpha_c\, c\, l$, HWHM γ_L), $H_n(\lambda)$ has a closed form analytical expression based on Arndt's formula [17]:

$$T(\lambda) = 1 - \alpha_c\, c\, l \frac{\gamma_L^2}{\gamma_L^2 + (\lambda - \lambda_c)^2} \tag{3.25}$$

$$H_n(\lambda) = \alpha_c\, c\, l\, S_n((\lambda - \lambda_c)/\gamma_L, \lambda_a/\gamma_L) + \begin{cases} 0 & n \geq 0 \\ 1 & n = 0 \end{cases} \tag{3.26}$$

with Arndt's formula

$$S_n(x, m) = -\frac{\epsilon_n}{2\pi} \int_{-\pi}^{\pi} \frac{1}{1 + (x + m\,\cos(\theta))^2} e^{-j\,n\,\theta} d\theta \tag{3.27}$$

$$= \frac{-\epsilon_n\, i^n}{2\, m^n} \frac{\left(\sqrt{(1 - i\,x)^2 + m^2} - (1 - i\,x)^2\right)^n}{\sqrt{(1 - i\,x)^2 + m^2}} + c.c. \tag{3.28}$$

c.c. stands for conjugate complex and x and m are the normalized wavelength and normalized modulation amplitude, respectively. Here γ_L has a unit of wavelength.

3.3 Single-mode semiconductor tunable lasers

Only electrically pumped laser devices, which can be operated continuous wave at room temperature, are particularly suitable for compact and low-cost applications. Also a narrow emission linewidth i.e. a single mode laser source is required, to sample the gas absorption spectrum with high resolution. Two candidates can be considered for this application: VCSELs (vertical-cavity surface-emitting lasers) and DFBs (distributed feed-back lasers).

3.3.1 VCSEL and DFB

A short comparison between the two single-mode laser types is given in Tab. 3.2. Compared to DFB lasers, VCSELs show lower threshold and operating currents. Even

	VCSEL	DFB
Threshold current	$\sim$ 1 mA	$\sim$25 mA
Operating current	$\sim$10 mA	$\sim$100 mA
Output power	$\sim$0.6 mW	$\sim$3 mW
On-wafer testability	yes	no
Current tuning coefficient	$\sim$0.6 nm/mA	$\sim$0.02 nm/mA

Tab. 3.2: Comparison between VCSELs and DFBs @ 2 μm [18, 19]

though the output power is lower, it is sufficient for the tunable diode laser absorp-

tion spectroscopy application (explanation see section 6.1.2). Because of the on wafer testability of VCSEL, it has a significant low cost potential.

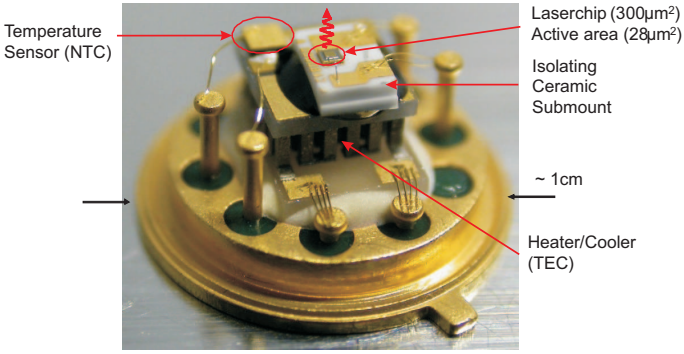

Fig. 3.9: A photograph of commercial InP-based vertical-cavity surface-emitting laser on a TO header including a thermo-electric cooler for laser temperature control (courtesy of VERTILAS GmbH).

A photo of a commercially available InP-based vertical-cavity surface-emitting laser is shown in Fig. 3.9. The laser chip temperature is controlled by the thermal-electric cooler (TEC) and measured by the temperature sensor (NTC). Since the NTC is mounted directly on the TEC, the measured temperature is the temperature of TEC, but not the temperature of laser chip, which is glued or soldered on the TEC via a ceramic submount. Therefore, the emission wavelength can not be controlled very exactly. An evaluation algorithm is needed for wavelength calibration of the emitted laser light, which is introduced in Chap. 6.

3.3.2 Wavelength range and material system

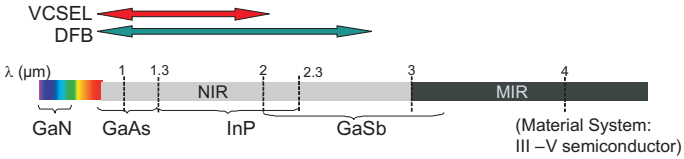

Fig. 3.10: The material systems for electrically pumped, room temperature, CW interband semiconductor lasers of different emission wavelength. The commercially available wavelengths ranges for VCSELs and DFBs of this kind are also shown. VCSELs up to 2.6 μm [8, 20, 21] and DFB lasers up to 3.06 μm [22] have been demonstrated.

In Fig. 3.10, different material systems for achieving different emission wavelengths by interband transitions in semiconductor lasers are shown. Because of the high bandgap energy, GaN is suitable for emission of visible or UV light and room-temperature, continuous-wave and electrically-pumped VCSELs were recently demonstrated [23]. The GaAs material system covers the red range and near-infrared range up to 1.3 μm.

InP covers the wavelength range from 1.3 μm to 2.3 μm, whereas GaSb is a suitable candidate from 2.0 μm onwards. Continuous wave, room-temperature DFB-QCL lasers are based on intraband transitions and these energy transitions have much lower energies. A wavelength range from 4.5 μm to 10.5 μm is commercially achieved with lasers operating at room temperature [24, 25]. However, these lasers are not as mature as conventional interband lasers and have high power consumption in the Watt range, therefore they are not considered in this work. Mid-infrared PbTe-based VCSEL devices [26] are optically pumped and not operating at room temperature, so they are also not suitable for compact sensor designs.

Commercially available interband DFB lasers reach up to 2.7 μm provided by datacom companies like NEL (InP-based up to 2 μm) and Nanoplus GmbH (InP- and GaSb-based, up to 2.7 μm), whereas the wavelength of commercially available InP-VCSEL is up to 2 μm provided by VERTILAS GmbH. Material system for long wavelength is interesting for gas sensing application, because then strong gas absorption bands can be accessed. The recently developed GaSb-based VCSELs [20] are investigated in this work in terms of gas sensing relevant aspects. Up to 2.6 μm wavelength, extended InGaAs detectors are available. For up to 1.1 μm wavelength, silicon detectors are preferred.

4 VCSEL characterization

Vertical-cavity surface-emitting lasers have gained increasing importance for numerous optoelectronic applications because of their intrinsic advantages, such as low threshold current and potential for low fabrication cost [27, 28]. While short wavelength single-mode VCSELs (< 1 μm) have been available for more than one decade [28, 29, 30], high-performance long-wavelength InP-based (1.3 μm - 2.3 μm) VCSELs were realized in the past ten years [31, 7, 32]. Recently, GaSb-based very long wavelength (2.3 μm - 2.6 μm) VCSEL have been developed [20, 21]. In this chapter, VCSELs are characterized in terms of suitability for TDLS. Main issues are:

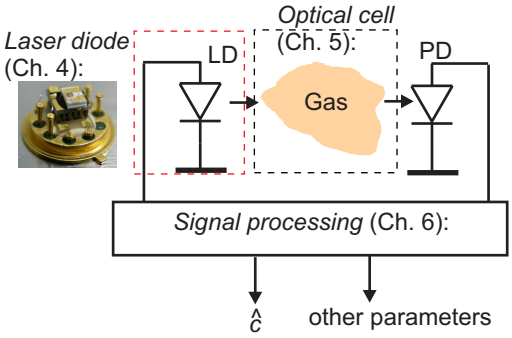

Fig. 4.1: Schematic overview of the sensor system. The three decisive components of the sensing system are laser diode (this chapter), optical cell and signal processing.

- What is the speed limitation of the wavelength tuning of VCSELs and how quick can gas detection be carried out? Since in a gas sensing system the laser tuning rate is the ultimate limiting factor of the gas detection speed, the two questions are equivalent. The FM response is a measure of the dynamic tuning behavior of the laser wavelength. It shows the dependency of the wavelength tuning range on the modulation frequency. Since wavelength tuning is basically a thermal effect, the FM response typically has a lowpass behavior. Prior to this work, FM response measurements for VCSELs did not exist in literature. The FM response of a laser diode including VCSELs has been theoretically described with a first order low pass model [33, 34, 35, 36]. The obtained typical values of the VCSEL thermal time constants τ_{th} are around 1 μs [36, 37], which corresponds to a 3 dB cutoff frequency of $f_c = 1/(2\pi\tau_{th}) \approx 160$ kHz. In a first order low pass model, the current-to-wavelength tuning coefficient above cutoff frequency is inversely proportional to the frequency, i.e. the tuning coefficient drops by a factor of 2 if the frequency is doubled. The experimentally demonstrated high speed tuning by Lackner [38] would then be impossible, because at 1 MHz only one-twelfth of the DC tuning coefficient is still available according to the first order low-pass model. This contradiction gave an inspiration to carry out measurements of FM

response of VCSELs and also develop a physically based model to explain it.

- Which properties of VCSELs are favorable for gas sensing? How is the sensor sensitivity influenced by the laser diode? For an ideal laser, i.e. constant laser intensity during tuning, there are no laser-caused features on the measured spectrum caused by the laser, neither with direct spectroscopy nor with wavelength modulation spectroscopy. For a real laser, the laser intensity changes nonlinearly if the laser current is tuned. This gives a nonlinear baseline if gas absorption is directly measured and typically an offset and slope on the second harmonic spectrum. The term 'laser background' therefore denotes the baseline of the measured spectrum due to a non-ideal laser current to intensity behavior. The laser background for WMS is not investigated in literature.

  The second important point is the absolute current tuning range of VCSELs.

4.1 Static tuning behavior

Like edge emitting lasers, VCSELs allow tuning of the wavelength via laser current. Up to the MHz range, the tuning of the wavelength is basically a thermal effect: the injection current causes an internal heating in the laser, which results in a refractive index variation in the laser material, so that the emitted wavelength changes [39]. An additional effect that changes the wavelength is the plasma effect, which describes the influence of the carrier density on the refractive index [40]. In case of a directly modulated VCSEL, the plasma effect is significantly lower than the thermal effect at low frequencies [41, 42]. The absolute tuning range of "good" VCSELs in the NIR is around

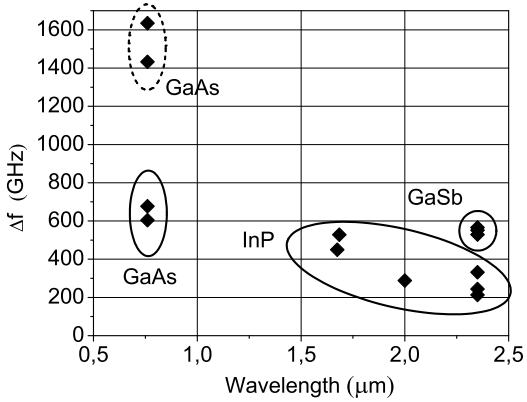

Fig. 4.2: Absolute current tuning range of different VCSELs (adapted from [43]). The usable current range was taken to be from threshold to rollover (InP- and GaSb-based VCSELs (solid), GaAs (dashed)) and threshold to 3 mA for GaAs VCSELs (single-mode operation regime, solid).

300-600 GHz (Fig. 4.2). This is given by 6-11 mA usable current range with tuning coefficients of 45-60 GHz/mA for InP- and GaSb-based VCSELs in the wavelength range 1.3-2.3 μm [42, 41]. GaAs-based VCSELs have 300 GHz/mA with only 2-3 mA

usable current range, where the single mode emission is achieved. The tuning range of a typical NIR DFB laser diode is around 100-200 GHz (100 mA @ 1-2 GHz/mA). The large current-to-wavelength tuning range of VCSEL enables the inherent wavelength scale calibration concept, which will be introduced in section 6.2.2. The current tuning coefficient is correlated with the thermal resistance, which is 1000-3000 K/W for single-mode VCSEL, and in the order of 100 K/W for DFBs [44]. In contrast to VCSELs the usable current range of DFB lasers is far below roll-over, because otherwise the output power is too high and catastrophic optical damage may occur. For DFB lasers the current tuning range can not easily get improved by increasing the thermal resistance because of the high threshold currents. Then a high temperature rise will occur inside the laser even before lasing sets in and the laser will not work at room temperature.

4.2 Dynamic tuning behavior

For small current variations around a bias point the differential current to wavelength shift behavior is linear. The laser behavior can be considered linear and time invariant with respect to its frequency/wavelength modulation (FM) behavior, which means that a small sinusoidal current variation always results in a sinusoidal wavelength variation (see Eq. (6.15)). The tuning coefficient given by the ratio of the amplitudes is frequency dependent, and it is obvious that it will have a kind of low-pass behavior because heat conduction is an inert process. In the following, the frequency response of the current-to-wavelength tuning rate is defined as 'FM response'. The FM response of a laser is of considerable interest for wavelength modulation spectroscopy (WMS) applications, because in this application the wavelength of the emitted light is modulated sinusoidally through the injection current. It is important to know how the current to wavelength tuning efficiency depends on the modulation frequency. Furthermore, this allows for a general characterization of the laser, because if the FM response is known, the small-signal wavelength response can be computed with a Fourier transform for arbitrary waveforms.

This section essentially summarizes the papers [45, 46, 47] published within the frame of this work.

4.2.1 Accurate measurement method for the FM response of tunable diode lasers based on wavelength modulation spectroscopy

There are several methods to measure the 'FM Response' of a laser diode [48, 49, 50]. To measure a wavelength variation, a conversion frequency/wavelength modulation (FM) to amplitude modulation (AM) is needed. Conventionally, an interferometer is used for that purpose [49, 51]. Another approach was presented by S. Schilt, who first used the change in the amplitude of the harmonic-spectrum of gas absorption to determine the FM response [48]. In this case, the FM to AM conversion is carried out by the gas absorption. However, the amplitude of the detector signal always depends on the bandwidth of the measuring equipment like the pre-amplifier, which is the reason for the upper frequency limit (100 kHz) in the measurement by S. Schilt.

In this work, also gas absorption is applied for FM response determination. But instead of the amplitude, the distance between two zero crossings of the measured second-harmonic spectrum is evaluated. The reduction of sinusoidal wavelength variation due to high speed tuning is indirectly measured via observing the narrowing of the measured second harmonic signal. A very simple experimental setup was developed,

which allowed for measurements up to 1 MHz. In doing so, a time distance instead of amplitude is detected, which is in principle insensitive to bandwidth and noise issues. Therefore no high bandwidth photodetector is required, i.e. an overall bandwidth of ≈ 2 MHz is sufficient. This is a significant advantage against interferometer measurements and S. Schilt's measurement.

The width of the second harmonic spectrum given by the distance between the two zero crossings or minima not only depends on the gas temperature and pressure, but also highly on the wavelength modulation amplitude λ_a. This effect is shown in Fig. 4.3(a).

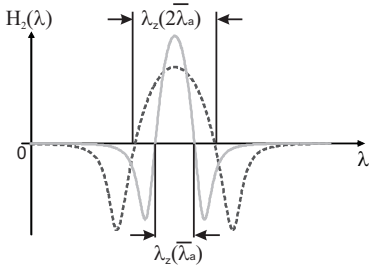

(a) The second-harmonic spectrum and its dependence on the wavelength modulation amplitude, with $\lambda_z(\lambda_a)$ representing the distance between the two zero crossings at modulation amplitude λ_a. By doubling λ_a, λ_z is also almost doubled.

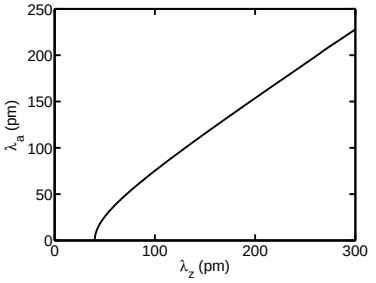

(b) Simulated relationship of the distance between the zero crossings λ_z of the second harmonic spectrum and the wavelength modulation amplitude λ_a. A constant laser intensity is assumed. A H_2O absorption line at 1853 nm with 20 cm path length and laboratory air conditions was used.

Fig. 4.3: Schematical and functional relationship of the modulation amplitude λ_a and distance between zero crossings λ_z.

Let $\lambda_z(\lambda_a(f)) =: \lambda_z(f)$ be the distance of the zero crossings of the second harmonic spectrum at modulation frequency f and $\lambda_a(f) = |H(f)|\, I_a \frac{\mathrm{d}\lambda}{\mathrm{d}I}$ the corresponding wavelength modulation amplitude (see Eq. (6.15)). I_a is the current modulation amplitude and $\lambda(I)$ the static current-to-wavelength tuning behavior of the laser. The FM response $H(f)$ is the normalized value of the tuning coefficient:

$$H(f) = \frac{\lambda_a(f)}{\lambda_a(0)} = F\left(\frac{\lambda_z(f)}{\lambda_z(0)}\right). \tag{4.1}$$

For simulation of the function F, three important models for laser AM can be distinguished, where $P(I)$ denotes the laser's P-I-characteristic measured at DC condition:

- ideal model:
$$P_L(t) = P(I) = \text{const.} \tag{4.2}$$
- static model:
$$P_L(t) = P(I_L(t)) = P\left(I + I_a \cos(2\pi f t)\right) \tag{4.3}$$
- dynamic model:
$$P_L(t) = P\left(I + I_a H(f) \cos(2\pi f t + \phi(f))\right) \tag{4.4}$$

Ideal model In the ideal case, the laser intensity is constant (see Eq. (4.2)). As outlined in section 3.2.2 a closed form expression for the harmonic spectrum of a Lorentzian line is available. Since this is usually fulfilled at atmospheric conditions (see section 3.1.3), the relationship between the distance of the zero crossings λ_z and the modulation amplitude λ_a can be computed (Fig. 4.3(b)). This is done by evaluating the zeros of Arndt's formula with an standard iterative algorithm. There is an almost linear correlation between λ_z and λ_a, which however does not cross the origin. It seems that the distance of the two zero crossings is limited by the Half-Width at Half-Maximum (HWHM) of the gas absorption line, which is in this case about 33 pm.

Static model If it is assumed that the output power of the laser immediately follows the laser current, then the static model Eq. (4.3) is used.

However, this model is incorrect at high frequencies, because the nonlinearity of the current to intensity behavior is due to the temperature variation in the active region. With increasing frequency the amplitude of the temperature variation decreases because heat conduction is a slow process. So the nonlinearity of the intensity variations should decrease as well. This gives rise to the other model that represents the opposite extreme case as compared to the static model.

Dynamic model For the dynamic model it is assumed that the current to intensity behavior is dynamic and has the same dynamics as in the current to wavelength behavior Eq. (4.4). If the nonlinearities of the P-I-characteristic are only due to the internal heating of the laser, it is reasonable to assume that the frequency behavior of the nonlinearities are the same as the current-to-temperature (or current-to-wavelength) behavior. This model can be simplified when the intensity scale of the P-I-characteristic is translated to the wavelength scale. Then the translated P-I-characteristic can simply be multiplied with the transmission function to simulate the effect of the laser AM on the second harmonic spectrum. However, this is an empirical assumption and the exact model is to be developed within the doctoral thesis of A. Hangauer.

The P-I-characteristic of the laser causes a background distortion of the harmonic spectra [52], whereas its quadratic term causes an offset [16] of the second harmonic spectrum that changes the distance of the zero crossings. It means that the curve representing the relationship between λ_z and H will be shifted. A comparison for different models for the InP-based 1853 nm VCSEL [32] is shown in Fig. 4.4.

Experimental setup for the measurement of the FM response of VCSELs

The measurement setup as shown in Fig. 4.5 is the basic setup for a WMS system to measure a second harmonic spectrum but with the difference that a frequency analyzer is used instead of a lock-in amplifier and that the laser diode is driven directly by the function generator (Agilent 33250A) with a shunt series resistor.

The limiting factor of the high speed measurement is the system bandwidth, all the equipments have to have a cutoff frequency above at least 1 MHz. Therefore, a commercial laser controller with limiting bandwidth is not used to control the laser current. Instead, the laser chip is connected to the voltage sources directly by an additional shunt resistance of 100 Ω to monitor the laser current. A sinusoidal current with the amplitude 373 μA and 43 μA was applied to InP VCSEL (1853 nm) and GaAs VCSEL (763 nm), respectively, as well as an appropriate bias current of 5.1 mA and 1.8 mA. The amplitude of the sinusoidal current is small enough compared to the bias current to assure that the current to wavelength behavior is still linear. The heat

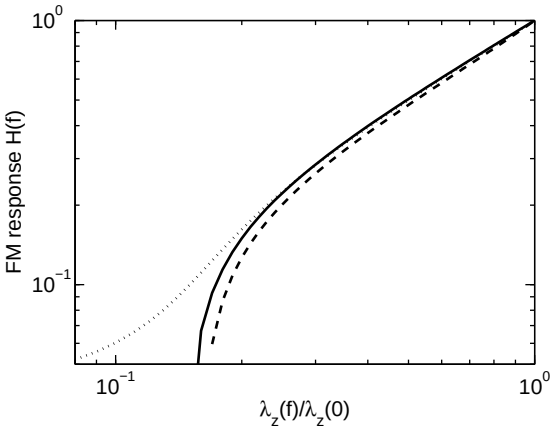

Fig. 4.4: The correction function F in double-logarithmic scale. The solid curve represents the simulation result of the Arndt formula (ideal model, Eq. (4.2)). The dotted and broken curves resemble the model of Eq. (4.3) and Eq. (4.4), respectively. An H_2O absorption line at 1853 nm measured with 20 cm path length under laboratory air conditions was used. The correction function is mostly linear and independent of th P-I model for large $H(f)$. The suitable range is about a factor of 5 decrease of $H(f)$.

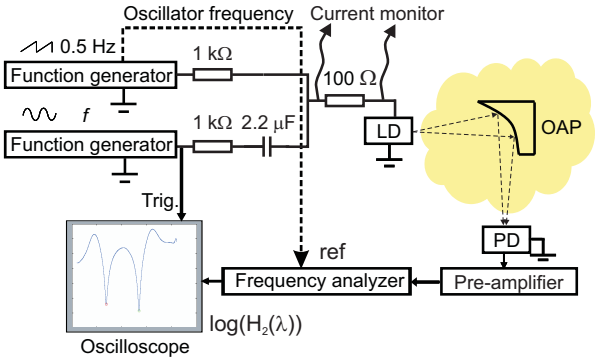

Fig. 4.5: Experimental setup for measuring the FM response with the WMS method. LD: Laser diode, PD: Photo diode, OAP: Off Axis Parabola. Difference to the basic laboratory setup for WMS (Fig. 3.7): frequency analyzer is used instead of Lock-in amplifier. Instead of using a laser controller, the laser is directly controlled with a function generator with a shunt series resistor inbetween to monitor the laser current.

sink temperature of the laser chip is kept at about 32 °C with a temperature controller (Profile LDC 200) with a precision of 0.01 °C.

The pre-amplifier (Hamamatsu C6438) utilized has a cutoff frequency of 2 MHz at a gain of 10^3 V/A. The frequency analyzer (HP 3585A) measures a single frequency at twice the modulation frequency f. The resolution bandwidth is set to 10 Hz to enable a low noise measurement, therefore the synchronization of the oscillator frequency becomes very important. It is a notably advantage that the frequency analyzer outputs the logarithm of the absolute value of the second harmonic spectrum $\log|H_2(\lambda)|$ because the two zero crossings are transformed into two very easily detectable sharp peaks as shown in Fig. 4.6.

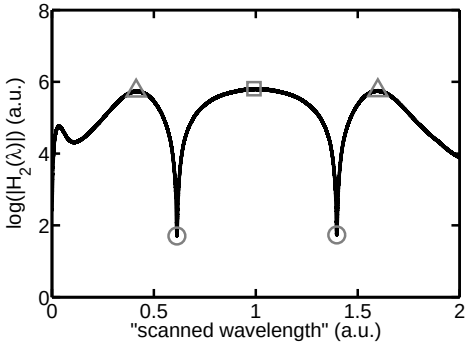

Fig. 4.6: Experimental second harmonic spectrum measured with a frequency analyzer: $\log|H_2(\lambda)|$. The characteristic points are the maximum (square), the two minima (triangles) and the zero crossings (circles). By observing the narrowing of the sharp peaks, the FM response is obtained by applying an (approximately linear) correction function to the distance of the zero-crossings.

It is also possible to determine the maximum and minima of the second harmonic spectrum, which correspond to the primary and secondary maximum of the signal of the frequency analyzer. The distance of the two minima as well as the ratio between the maximum and minimum could be also taken as a measure for the modulation amplitude λ_a. However, the minima are no sharp structures like zero crossings in logarithm scale and are therefore not so precisely detectable.

Measurement procedure To summarize, the measurement procedure works as follows:

- Select a gas absorption line in the tuning range of the laser which gives a strong enough absorbance, so that the offset on the second harmonic spectrum due to the laser P-I-characteristic is minimized.
- Measure the second harmonic spectrum at different modulation frequencies with a spectrum analyzer instead of a lock-in amplifier.
- Detect the distance of the two sharp peaks (zero crossings) off-line.
- Normalize the distances with the distance of the zero crossings at a near DC frequency.

- Use the correction function F to get the normalized FM response.

Verification of the method To guarantee the correctness of the new method, reference measurements with a step scan spectrometer (Bruker Vertex 70) were carried out. The laser was modulated with a sinusoidal current at frequency f and the same amplitude as in the WMS measurement. The temperature of the laser was also stabilized with a temperature controller. A step scan spectrometer uses a Short Time Fourier Transform (STFT) to get the momentary spectrum of the light at certain short time intervals with a minimum time resolution of 5 ns. The time intervals were shifted until at least one period of the modulation signal (i.e. $T_0 = 1/f$) was covered. The emission peak of the spectrum taken at each interval is detected and taken as the momentary wavelength of the laser diode. With sinusoidal injection current a sinusoidal variation of the emission peak is expected and practically observed. The wavelength modulation amplitude is then determined by evaluating the shift of the emission peak. In Fig. 4.7 the measurement data for the InP-based 1853 nm VCSEL from the WMS method and step scan spectrometer are shown. Both methods show very good agreement. Due to

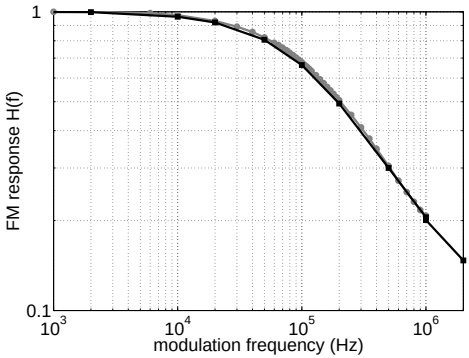

Fig. 4.7: The measurement data of FM response of a InP-based 1853 nm VCSEL using WMS method (gray curve) and spectrometer (black curve). The results from both methods show excellent agreement.

the automatic control of the WMS measurement equipment, it was possible to take more samples around the cutoff frequency (about 100 kHz) and to measure the FM response up to at least 1 MHz. Compared to the spectrometer measurement, the correction with ideal model gave a maximum error of 6 %, the dynamic model 8 % and the static model 5 %. Since all the models describe extreme cases, the correction should be good enough to approximate the real case. It is important to note that these error values not only depend on the PI model, but also strongly on the strength of the gas absorption. In Fig. 4.7 the static model is used for the correction.

4.2.2 Experimental characterization of the FM response of VCSELs

Using the characterization method developed in the last section, the performance of the following two different VCSEL structures shown in Fig. 4.8(a) and Fig. 4.8(b) could be studied:

- InP-based VCSEL at 1853 nm, which is packaged in a windowless TO-46 housing and placed on a thermoelectrically cooled laser mount. The long-wavelength ($\lambda \geq 1.3$ μm) InP-based VCSEL is described in detail in [32].
- GaAs-based VCSEL at 763 nm in a TO-5 housing with window and thermoelectric cooler. The fabrication and performance of this kind of VCSEL is described in [53].

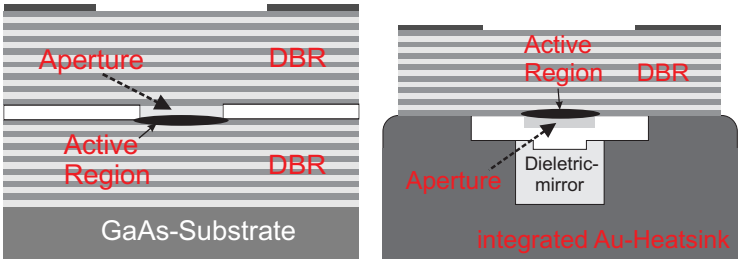

(a) GaAs-based VCSEL (763 nm) (b) InP-based BTJ-VCSEL (1853 nm)

Fig. 4.8: (a) Schematical cross-section of $\lambda = 763$ nm VCSEL. (b) Schematical cross-section of $\lambda = 1853$ nm BTJ-VCSEL. DBR: Distributed Bragg Reflector.

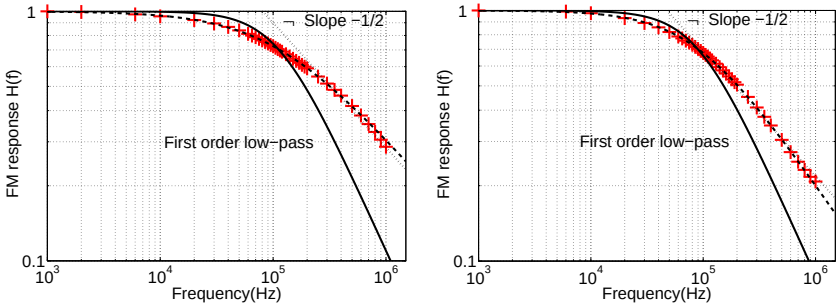

(a) GaAs-based VCSEL (763 nm) at $I = 1.8$ mA and $I_a = 43$ μA (b) InP-based BTJ-VCSEL (1853 nm) at $I = 5.1$ mA and $I_a = 373$ μA

Fig. 4.9: Measured FM response of the VCSELs (red '+'). The dotted and solid curves correspond to slope of -0.5 and the first order low-pass case, respectively. The dashed curve resembles the empirical model Eq. (4.5) with $n = 0.52$ (GaAs) and $n = 0.65$ (InP). The good agreement with the empirical square root model confirms the square root behavior of the measurement data.

The measured FM responses for both VCSELs are depicted in Fig. 4.9(a) and Fig. 4.9(b). It can clearly be seen that the frequency behavior of both VCSELs follows a square root law, since the slope reaches approximately $-1/2$ in the doubly logarithmic scale (see dotted line in Fig. 4.9(a) and Fig. 4.9(b)). The following empirical model for the normalized FM response $H(f)$ was found to describe the FM amplitude

response quite well:

$$H(f) = \frac{1}{\sqrt{1 + (f/f_c)^{2n}}} \tag{4.5}$$

Where f_c is the 3 dB FM cutoff frequency and $-n$ the slope in a doubly logarithmic scale for $f \to \infty$. The curve fit for the 763 nm VCSEL gives $n = 0.52$, which is in very good agreement with the observed square root law. Although the slope parameter for large frequencies for the 1853 nm VCSEL is $n = 0.65$, the measurement data show good agreement with the slope $-1/2$ in the measured frequency range as well.

The 3 dB cutoff frequencies f_c are $f_c \approx 88$ kHz (1853 nm) and $f_c \approx 110$ kHz (763 nm).

When the amplitude of the sinusoidal injection current was varied, the behavior of the normalized FM response did not change for both lasers.

Although both VCSELs show a low-pass behavior, it clearly does not correspond to a first order low-pass, but follows a square root law above cutoff frequency (about 100 kHz). This means that doubling the frequency of the injection current will cause the current to wavelength tuning rate to drop only by about 30 % ($1/\sqrt{2}$) instead of 50 % as expected by the first order low-pass. This is a clear advantage for wavelength modulation spectroscopy applications with VCSELs, because the wavelength of the laser can be tuned at rather high frequencies without significant loss of the tuning efficiency compared to DFB lasers. For the 1853 nm VCSEL, the current to wavelength tuning rate of 0.6 nm/mA at 1 kHz drops only to 0.12 nm/mA at 1 MHz.

Additionally, it is concluded that the step response of the VCSELs is not an exponential function as with a first order low-pass. As a result, the FM cutoff frequency of the VCSELs cannot be determined easily by a exponential curve fit with a measurement of the wavelength step response.

It is remarkable that in spite of their different device structure both VCSELs show nearly the same FM response. Obviously, the square root law behavior of the two different VCSELs is due to general thermal properties of the specific geometry of VCSELs. To find out the reason of the surprising square root law, a thermal model for VCSEL is developed in the next section.

4.2.3 Theoretical model of the dynamic thermal tuning behavior of VCSELs

A theory of the FM response for distributed feedback (DFB) lasers already exists that well matches the measured laser behavior [54]. For a theoretical analysis and explanation of the measured square root law of FM response of VCSELs, a simplified thermal VCSEL model based on the heat equation is developed and the FM response is computed analytically. The active region of the VCSEL is modeled as a Gaussian-distributed instantaneous plane heat source. The average temperature in the active region over time is assumed to be proportional to the wavelength of the laser. The FM impulse response (thermal impulse response) is therefore the variation of the average temperature in the mode volume over time, when a heat impulse is generated at time $t = 0$. The Fourier transform of this impulse response then gives the FM response of the laser.

Simplified thermal VCSEL model and derivation of the FM response

For theoretical calculations the following assumptions about the heat source, conduction medium and optical mode distribution have been made (see illustration in Fig. 4.10):

- Heat source: The active region generates the heat and is modeled as an infinitely thin plane heat source at $z = 0$. The strength of heat generation in the infinitely thin plane is radially Gaussian-distributed with the standard deviation R_0. The heat production is a δ-function and occurs at $t = 0$.
- Optical mode: The optical mode is radially Gaussian-distributed with the standard deviation R_1 and the average temperature of the active region affects the emitted wavelength. The z extension (h) of the optical field is neglected in this simplified thermal analysis, which fits well to usual VCSELs with small $h/(2R_1)$ ratio.
- Conduction medium: The medium is isotropic and extends infinitely in the x, y and positive z direction. The substrate acts as an ideal heat sink, i.e. it is kept at a constant temperature.

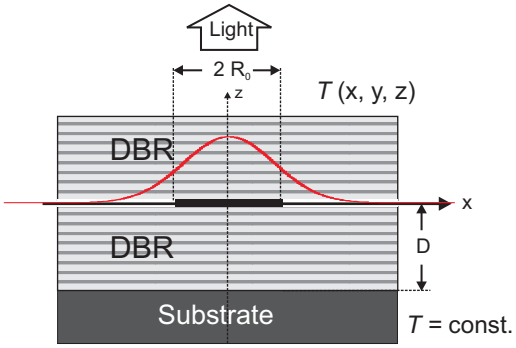

Fig. 4.10: Schematic cross-section in the $x-z$ plane of the idealized VCSEL structure. The active region (solid black) is modeled as an infinitely thin plane at $z = 0$ that generates heat with radially Gaussian distributed intensity (standard deviation: R_0). The substrate is located at $z \leq -D$ and kept at a constant temperature. DBR: Distributed Bragg reflector. The optical mode is also assumed to be radially Gaussian-distributed.

The equations for the transient heat distribution in the VCSEL are given by the heat equation for an isotropic solid (Eq. 1.6.7 in [55]) with appropriate boundary condition and intensity distribution of the heat source q (unit: W/m^3):

$$\frac{d^2T}{dx^2} + \frac{d^2T}{dy^2} + \frac{d^2T}{dz^2} + \frac{q(x,y,z)}{K}\delta(t) = \frac{1}{\kappa}\frac{dT}{dt}, \tag{4.6}$$

$$T(x,y,z,t) = 0 \qquad \text{for } z = -D. \tag{4.7}$$

The thermal diffusivity $\kappa = \frac{K}{c\,\rho}$ is a material constant, which is a measure of transient heat flow and is defined as the thermal conductivity K divided by the product of

specific heat capacity c times density ρ. The plane heat source is assumed to have a Gaussian-distributed intensity, i.e.

$$q(x,y,z) = \delta(z-z_0)\,\frac{1}{2\pi R_0^2}\exp\left(-\frac{x^2+y^2}{2R_0^2}\right), \tag{4.8}$$

whereby the source is located in the plane $z = z_0$ and the standard deviation of the distribution is assumed to be the current aperture radius R_0.

The transient temperature response $T_g(x,y,z,t)$ at an arbitrary point (x,y,z) at time t can be calculated by spatial convolution of the transient point heat source response and the source distribution $q(x,y,z)$ (Eq. 10.2.5 in [55]). The boundary condition Eq. (4.7) is satisfied by using the method of images (section 10.10 in [55]). With the disc heat source located at $z_0 = 0$, we associate the mirrored sink with the same strength but opposite sign at $z_0 = -2D$. The superposition of this two sources will give a zero temperature at $z = -D$.

The average temperature $\overline{T}_g(t)$ of the active region is determined by averaging $T_g(x,y,z,t)$ with respect to the optical mode distribution $M(x,y,z)$.

$$\overline{T}_g(t) = \iiint_{-\infty}^{\infty} T_g(x,y,z,t)M(x,y,z)\mathrm{d}x\mathrm{d}y\mathrm{d}z. \tag{4.9}$$

As noted in the assumptions above, the optical mode distribution is also chosen to be a Gaussian function

$$M(x,y,z) = \delta(z)\,\frac{1}{2\pi R_1^2}\exp\left(-\frac{x^2+y^2}{2R_1^2}\right). \tag{4.10}$$

The FM frequency response is the Fourier transform $\widehat{T}_g(f)$ of the thermal impulse response $\overline{T}_g(t)$. The results are

$$\overline{T}_g(t) = \frac{1}{4\pi^{3/2}\sqrt{\kappa t}\,(R_0^2+R_1^2+2\kappa t)}\left(1-\exp\left(-\frac{D^2}{\kappa t}\right)\right), \tag{4.11}$$

$$\widehat{T}_g(f) = \frac{\sqrt{f_0}}{4\sqrt{2}\kappa^{3/2}}\left(\exp\left(i\frac{f}{f_0}\right)\operatorname{erfc}\left(\sqrt{i\frac{f}{f_0}}\right) - \exp\left(i\frac{f}{f_0}+d^2\right)\operatorname{erfc}\left(\sqrt{i\frac{f}{f_0}}+d\right)\right), \tag{4.12}$$

and the normalized FM response $H(f)$ is defined by:

$$H(f) := \widehat{T}_g(f)/\widehat{T}_g(0). \tag{4.13}$$

Basically, $H(f)$ depends on two parameters. Firstly, the frequency scale parameter

$$f_0 := \kappa/\left(\pi(R_0^2+R_1^2)\right) \tag{4.14}$$

scales the FM response in frequency. The 3 dB cutoff frequency f_c is approximately proportional to f_0^2, i.e.

$$f_c \approx \frac{f_0^2}{64\,\widehat{T}_g(0)^2\,\kappa^3} = \frac{\kappa}{(1-\exp(d^2)\operatorname{erfc}(d))^2\,2\pi(R_0^2+R_1^2)}, \tag{4.15}$$

or rather

$$f_c\cdot\widehat{T}_g(0)^2 \approx \left((8\pi)^2\kappa(R_0^2+R_1^2)^2\right)^{-1}. \tag{4.16}$$

If κ, R_0, R_1 are held constant, the cutoff frequency f_c has an inverse quadratic relationship with the tuning coefficient at DC condition, which is proportional to $\widehat{T}_g(0)$ (Fig. 4.11(a)).

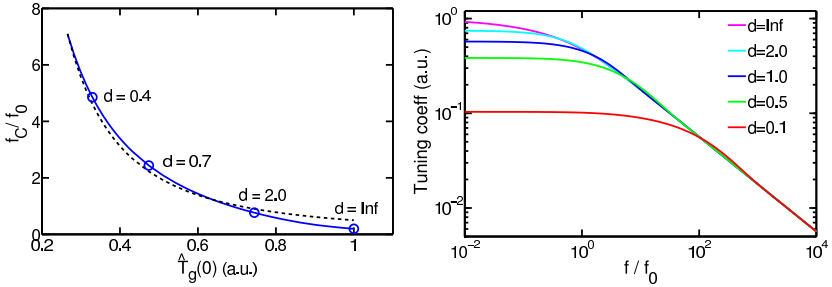

Fig. 4.11: (a) Exact (solid curve) and approximate (Eq. (4.15), broken curve) relationship of the normalized cutoff frequency f_c/f_0 and the tuning coefficient at DC condition with constant R_0, R_1 and κ, when d is adjusted. (b) The "tuning coefficient" $\widehat{T}_g(f)$ for different d with constant R_0, R_1 and κ (the curves are shown in the same order as listed in the legend).

The second parameter is the VCSEL form factor

$$d := D/\sqrt{(R_0^2 + R_1^2)/2}, \tag{4.17}$$

which is the quotient of the distance of the active region to the substrate D and the square mean of the current aperture radius R_0 and the optical mode radius R_1. A decreasing D (active region nearer to the heat sink) or d with constant R_0, R_1 and κ increases the cutoff frequency but lowers the tuning coefficient (Fig. 4.11(b)). It should be noted that the tuning behavior for high frequencies does not depend on D or d (constant R and κ parameters), because the curves have the same asymptote. In the simulation, the heat source and the optical mode are assumed to be both Gaussian-distributed with the same radius. This is not a limitation, because according to calculations the same result for $\overline{T}_g(t)$ is obtained if $R_0^2 + R_1^2$ is kept constant.

In case of no boundary condition, (i.e. $d \to \infty$) the normalized FM response can be expressed in terms of a confluent hypergeometric function of the second kind (13.6.39 in [56]), which is related to the generalized hypergeometric function:

$$H(f)|_{d\to\infty} = \exp\left(i\frac{f}{f_0}\right)\,\mathrm{erfc}\left(\sqrt{i\frac{f}{f_0}}\right) \tag{4.18}$$

$$= \pi^{-1/2}\,\mathrm{U}\left(\frac{1}{2},\frac{1}{2};\,i\frac{f}{f_0}\right) \tag{4.19}$$

$$= \pi^{-1/2}\frac{1}{\sqrt{i\,f/f_0}}\;{}_2F_0\left(\frac{1}{2},1;-\frac{1}{i\,f/f_0}\right). \tag{4.20}$$

Note that $\left|{}_2F_0\left(\frac{1}{2},1;-\frac{1}{z}\right)\right|$ approaches its final value 1 very quickly for $f > f_0$. This demonstrates that U has basically $1/\sqrt{if/f_0}$ behavior for $f \gg f_0$ and thus shows that

$H(f)$ follows a square root law. For decreasing d the slope of the FM response at high frequencies in doubly logarithmic scale remains to be 1/2 (see Fig. 4.11(b)), because the second summand in Eq. (4.12) reaches zero very quickly for increasing f.

Comparison with experimental data

In Fig. 4.12 measurement data of the FM response of two different types of VCSELs (Fig. 4.9(a) and Fig. 4.9(b)) are shown in conjunction with the theoretical model presented in this section with fitted parameters for f_0 and d. The values in parentheses behind d are the expected values determined by dividing the current aperture radius of the VCSEL and the approximate distance of the active region to the substrate. An expected value for f_0 (Eq. (4.14)) is not known, because the average thermal conductivity as well as the average thermal diffusivity of the compound semiconductor material are difficult to obtain.

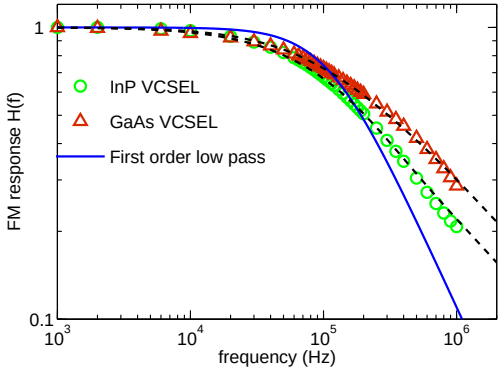

Fig. 4.12: The normalized FM response $H(f)$ of GaAs VCSEL (triangles) and InP VCSEL (circles) and the simplified thermal model (broken curve). The solid curve represents the first order low pass with the cutoff frequency 110 kHz, which is same for the GaAs VCSEL. It clearly can be seen, that the developed thermal model explains the square root behavior of the experimental data quite well.

- GaAs-based VCSEL (763 nm, ULM Photonics): $R_0 = R_1 = 1.5$ μm, $d = 2.7$ (expected: 2.6), $f_c = 110$ kHz ($f_0 = 190$ kHz)
- InP-based VCSEL (1853 nm, VERTILAS): $R_0 = R_1 = 2.5$ μm, $d = 0.82$ (expected: 0.8), $f_c = 85$ kHz ($f_0 = 42$ kHz)

4.2.4 High-speed wavelength tuning

For several applications, high-speed wavelength tuning is desired. For instance, a spatial gas concentration measurement in combustion environments e.g. in motor compartments requires fast sensing (down to the sub-ms range) [57]. Also for 2D imaging fast tunability is required. This is because the point of the image are measured sequentially and thus a high measurement rate for each spatial point is needed.

4.3 Gas sensing limitations by the laser diode

GaAs-and InP-based RT-CW-VCSELs covering a wavelength range from 700 nm to 2.3 μm are well known [53, 32, 7]. The absorption of most gases such as methane and water is by more than one order of magnitude stronger at wavelengths above 2 μm than at shorter wavelengths [10]. Especially for carbon monoxide (CO), only the utilization of wavelengths around 2.3 μm (second overtone band) enables sensing with the required ppm resolutions applying a few ten cm path length and one second averaging time for a typical sensor system using TDLS (see Fig. 3.1). For long wavelength VCSELs ($>$ 2 μm), the GaSb material system is the preferable candidate because of the small band gap energy and large optical gain in this spectral region, whereas the newly developed highly strained InP-based VCSELs at 2.3 μm have reached the upper wavelength limit of the InP material system [7]. For these reasons, GaSb-based VCSELs have a great potential to significantly extend the application areas of TDLS. Recently, single mode EP-CW-RT VCSELs based on GaSb emitting around 2.3 μm have been reported [20, 58]. In this section, VCSELs emitting at 1680 nm and 2300 nm are examined and their suitability for gas sensing is investigated. Special emphasis is placed on the 2.3 μm GaSb-based VCSEL, because these VCSELs just became available and the material system is not yet as mature as the GaAs or InP based material system.

As for the measurement cell, there is also a spectral baseline caused by the laser. This may be caused by kinks in the P-I-characteristic, which display as unwanted ripples on the second harmonic measurement signal. The laser background is the stronger the higher the nonlinearity of the laser P-I-characteristic is. If especially kinks in the P-I-characteristic are observed, a high level of ripples on the second harmonic measurement signal will be present.

4.3.1 InP-based laser at 1680 nm

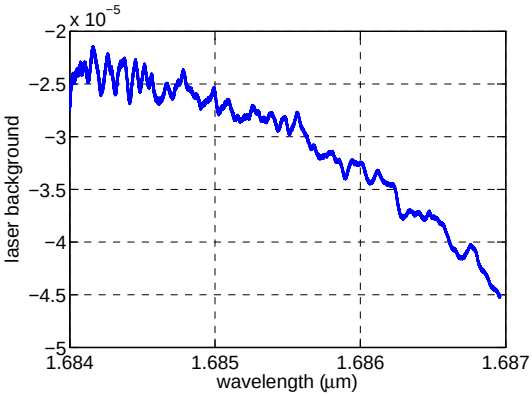

Fig. 4.13: The background on the second-harmonic spectrum caused by an InP-based VCSEL at 1680 nm ("laser background"). An amplitude fluctuation of as low as 2×10^{-6} superimposed on a parabolic background, originated from the bending of the P-I-characteristic of the laser is observed.

As can be seen in Fig. 4.13 InP- based VCSELs have a rather low laser background below 10^{-5}. Additionally, a negative offset and a negative slope are observed on the second harmonic measurement signal. This is attributed to the slight negative bending of the P-I-characteristic, while the second harmonic laser background is approximately given by its second derivative.

4.3.2 GaSb-based laser at 2330 nm

Utilizing GaSb-based 2.3 μm VCSEL, the measured second harmonic spectrum for CO (Fig. 4.14(a)) and mixture of CO and CH_4 (Fig. 4.14(b)) together with their curve fits are shown. The curve fittings using parameters from the HITRAN database [10] show very good agreement with the measurement data. The Lorentzian profile based second-harmonic formula from Arndt (Eq. (3.2.2)) is used to program the model function for the minimal mean square error curve fit (section 6.1). With curve fit, the tuning coefficient was determined to be 0.23 nm/K, which is 30 % higher than 0.17 nm/K for the 2.3 μm InP devices [59].

This section summarizes work published in [60, 61].

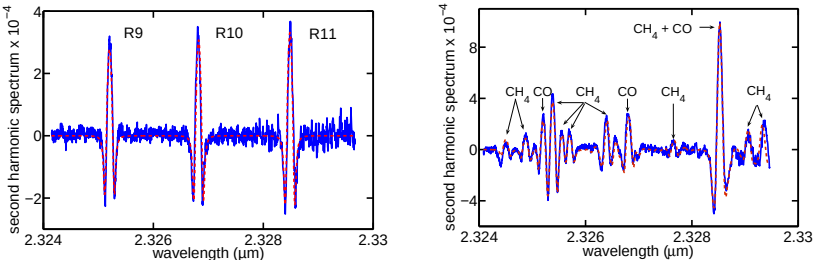

(a) CO gas (b) CO and CH_4 gas

Fig. 4.14: Measured second harmonic spectra (solid curves): (a) with 57 ppm CO (b) 50 ppm CO and 140 ppm CH_4 and the corresponding curve fits with tabulated line parameters (broken curves). The laser background was measured separately and subtracted.

Laser background

A complex background pattern has also been observed during the CO measurement (Fig. 4.15), which was measured separately by filling a single-reflective cell (section 5.4) with nitrogen and subtracted in the measurement to enable a good curve fit. A complex background pattern exists in a current scan spectrum as well. Because the cell background is far below 10^{-5}, the complex spectral pattern may only originate from the laser diode itself. To understand the origin of the laser background, the device behavior is investigated at varying current because the background pattern in the second harmonic spectra can be attributed to features in the P-I-characteristics.

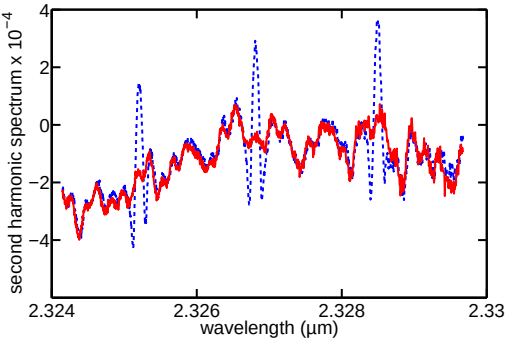

Fig. 4.15: Second harmonic spectrum (broken curve) and measured background (solid curve) with temperature scan. This complex spectral pattern is caused by the laser diode.

Origin of Laser background

The P-I-characteristics of the laser device is measured and also the approximate first derivative of the P-I-characteristics by measuring the first harmonic without gas absorption. It can be seen clearly that the first derivative shows steps (Fig. 4.16, middle), which corresponds to kinks in the P-I-characteristic (Fig. 4.16, top). The second harmonic without gas absorption (Fig. 4.16, bottom) approximately represents the second derivative of the P-I-characteristics. For typical single mode lasers the P-I-characteristics shows no kinks and the laser induced second harmonic background is typically a negative offset with a slight negative slope (see Fig. 4.13).

Two possible causes for the spectral background could be excluded. One assumption for a possible reason for the kinks in the P-I-characteristics is that the emission pattern of the transversal mode rotates with the laser current and thus causes a change in light intensity at the photodetector. To investigate the behavior of transversal modes, the far-field of the laser diode is recorded with an InSb based infrared camera. A LP 01 transversal mode emission has been observed (Fig. 4.17(a)). However, measurements of the far field for different injection currents showed no rotations. Another assumption are mode flips while tuning of the laser current. A successful curve fit to measured gas absorption spectra (Fig. 4.17(b)) showed that no wavelength/mode flips are associated with the kinks on the laser P-I-characteristics. With mode flips, it would not be possible to fit the spectra because the wavelength scale changes discontinuously. The dynamic range/amplitude of the background pattern is different for the temperature scan (5×10^{-4}) (Fig. 4.15) and the current scan (10^{-3}) (Fig. 4.17(b)), which indicates that the complex background pattern is not caused by any optical resonance.

The exact nature of the kinks in the P-I-characteristic causing the spectral background is still unclear. This effect was, however, not observed in the second generation lasers.

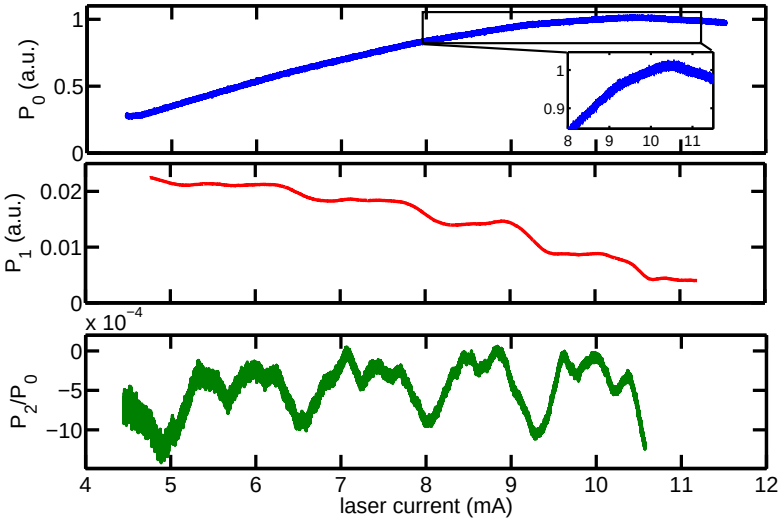

Fig. 4.16: The first harmonic $P_1(I)$ of the intensity modulation of the GaSb-VCSEL (middle) (i.e. approximate derivative of the P-I-characteristics) shows cascade behavior with increasing laser current, which indicates that the laser P-I-characteristics $P_0(I)$ (top) exhibits kinks. This causes the complex laser background pattern $P_2(I)/P_0(I)$ on the second harmonic spectrum (bottom). The current modulation amplitude I_a was around 100 μA.

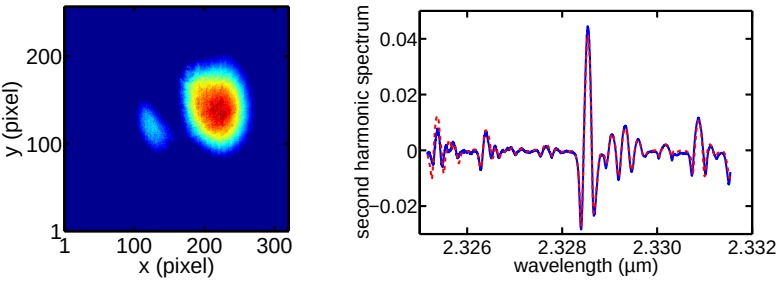

(a) (b)

Fig. 4.17: (a) Measurement of the far field of the GaSb VCSEL with injection current of 11 mA (b) Measurement of CH_4 second harmonic spectra with current tuning and the curve fit (broken curve) which proves continuous wavelength tuning. The kinks are thus not associated with mode-jumps and rotating the far-field is not observed.

4.4 Conclusion

Dynamic tuning of VCSELs In this chapter, the characterization of the FM response was shown for two different types of VCSELs up to frequencies of 1 MHz: GaAs-based VCSEL (763 nm) and InP-based VCSEL (1853 nm). Both of them show the same qualitative FM response behavior, which can be described by a square root law, and therefore cannot be modeled by a conventionally assumed first order low-pass. The square root law behavior is a significant advantage for laser spectroscopy applications with VCSELs, because the decrease of the current-to-wavelength tuning coefficient is less severe compared with the case of the first order low-pass. These characteristics have been very beneficial, for example for high-speed tuning at 5 MHz of a 1680 nm VCSEL used for methane sensing [38], which would be impossible if the thermal tuning has a first order low pass behavior with a cutoff frequency around 160 kHz. Compared to existing measurements of DFB lasers up to 100 kHz [48], measurements at frequencies up to 1 MHz are performed. These are enabled by using a novel and accurate characterization method based on wavelength modulation spectroscopy. There the distance of the zero crossings of the second harmonic spectrum with a constant modulation current is detected for each modulation frequency. A reference measurement with a step scan spectrometer was carried out, which validates the WMS measurement. The WMS method requires only standard equipment and a simple mechanical setup compared to an interferometer measurement. Also no high bandwidth photodiode is required. It was also possible here to derive closed analytical expressions for the FM impulse and frequency response that give a significantly better qualitative description of the actual device behavior than the common first order low pass model. The calculation is based on the assumptions of a two-dimensional Gaussian-distributed plane heat source and optical mode distribution. The analytical expression of the FM response shows a square root behavior for high frequencies and recreates the measurement result with good accuracy. VCSELs show a 2D heat generation in a 3D space, which results in this square root behavior and a high cutoff frequency compared to conventional edge emitting lasers.

GaSb-based VCSELs The newly developed CW EP GaSb-based VCSELs are suitable for simultaneous gas detection of CO and CH_4 at 2.3 μm. Compared to the InP based VCSEL, the GaSb based VCSEL has a 30 % higher temperature tuning coefficient, and a lower threshold current. The GaSb material system is a suitable candidate for wavelengths over 2.3 μm. For the first generation lasers, the complex background pattern in the second harmonic spectrum is caused by kinks in the PI characteristics. These are not associated with mode flips because the device remained in stable single mode operation during spectrum scan with current/temperature. Moreover, there is no rotation in the far field emission pattern during current tuning. The reason for the kinks in the P-I-characteristics is still unclear, but they were no longer present in selected second generation lasers. The presence of kinks clearly shows that the laser background can give the limiting factor of sensing sensitivity. For gas sensing with the necessary sensitivity, a laser background below 10^{-5} is needed. It is also shown that this performance is easily achieved, as an example measurement of a VCSEL from the mature InP material system indicates.

5 Optical gas cell

The optical cell is a container where the interaction between gas and light takes place. Thus discussion of the physics and properties of the optical gas cell are essential in order to understand how the cell detects trace (or bulk) gases. High sensitivity is the most desirable property, which is given by the smallest resolvable gas absorption coefficient α_{res}. This quantity depends on the interaction length l (inverse relationship) and the resolvable absorbance a_{res} (direct relationship). a_{res} is the smallest fraction of absorbed light intensity that can be resolved. This is determined either by the noise produced by the detector or laser, or the random spectral baseline given by the cell geometry itself (an example of 'cell background' is given in Fig. 5.7). In the literature, only the sensitivity of the total sensor system is mentioned, without characterization of 'cell background'. Thus the literature does not deal separately with the influence of the cell, detector and/or laser noise and signal processing on the overall sensor performance.

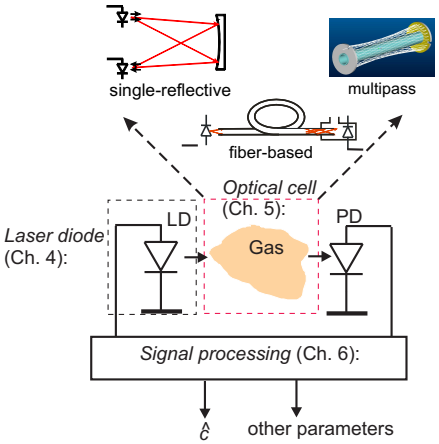

Fig. 5.1: Schematical overview of the sensor system. Both 'conventional' gas cell - single/multi-reflective cells and newly developed fiber-based gas cells are analyzed and characterized in this chapter.

High sensitivity conventionally refers to the minimum detectable mixing ratio of the gas (i.e. concentration). However, the minimum detectable number of molecules may also be significant, but this is not usually considered in the literature.

The gas exchange time also has to be considered to enable efficient gas detection. A large gas exchange time given by the small area of the gas inlet/outlet predominantly limits the detection speed. Therefore, the gas exchange time for a fiber-based sensor may be an issue not discussed so far, except for the case of gas diffusion into the fiber [62].

Following from the above factors, different types of optical cells are studied with the focus on the suitability for low-level (sensitive) and low probe volume (ml) gas sensing. Robustness in harsh conditions is also an important aspect which is investigated.

The following questions are to be answered:

- How to measure the 'cell background' and identify its origin (section 5.3)?
- How to develop robust sensing in harsh conditions, i.e. an optical cell which is robust against thermal cycling, condensation and contamination (section 5.4)?
- How to produce sensitive measurements with a simple setup and without the disadvantages (for example, sensitive alignment or large sample volume) of the multi-pass cells known from the literature (section 5.7)?
- What is the lowest resolvable number of molecules for different cells (Tab. 5.1)?
- What is the gas exchange time limit, especially for fiber based cells (section 5.6 and section 5.7)?

The gas absorption spectrum is linearly superimposed upon the cell background (section 5.1). According to the theory, design criterion are given (section 5.2). After a discussion of geometric sources of 'cell background' within the cell itself, different cell variants are investigated to determine their contribution to 'cell background'. The resolvable absorption coefficient and a newly defined 'cell cross section' is then calculated for each cell type and compared in Tab. 5.1. The investigation starts with 'conventional' cell designs (i.e. single-/multipass cells), and then moves on to a novel fiber-based cell, which showed the most interesting properties.

5.1 Theory of the optical cell

In this section, a theory for the 'cell background' is derived, which is useful for analysis for the optical cell and for deriving the design criterion of the optical cell. If it is assumed that the gas does not influence the light propagation, except for an overall attenuation, the total transmission $T(\lambda)$ is given by gas transmission $T_{\mathrm{gas}}(\lambda)$ multiplied with the cell transmission $T_{cell}(\lambda)$:

$$T(\lambda) = T_{gas}(\lambda)\ \underbrace{T_{0,cell}\left(1 - A_{bg,cell}(\lambda)\right)}_{T_{cell}(\lambda)} \tag{5.1}$$

$T_{cell}(\lambda)$ is the transmission of a cell under vacuum conditions. It has an attenuation factor $T_{0,cell}$ and wavelength dependent fluctuation $A_{bg,cell}(\lambda)$ (the 'cell background', example shown in Fig. 5.7).

Among the conditions investigated within this work, the absolute cell transmission $T_{0,cell}$ can be in the range of 0.001 to nearly 1. It depends on the type of the cell and its condition e.g. contaminated, condensation, mirror reflectivity, etc... . The cell background is ideally zero but typically $|A_{bg,cell}| \leq 0.001$. When $0.9 \leq T_{gas} \leq 1$, the following relationship is obtained:

$$T(\lambda) \approx T_{0,cell}\ \left(T_{gas}(\lambda) - A_{bg,cell}(\lambda)\right) \tag{5.2}$$

The interpretation of this is straightforward: the cell background/interferences are directly superimposed on the gas transmission, if the background is small and the gas

transmission is close to one, which is the case in the framework of the investigations. From Eq. (5.2) we obtain for the WMS harmonic spectra an equivalent relationship:

$$H_n(\lambda) \approx T_{0,cell} \left(H_{n,gas}(\lambda) + H_{n,bg,cell}(\lambda) \right). \tag{5.3}$$

$H_{n,gas}$ is the harmonic spectrum for the gas (Eq. (3.24)) and $H_{n,bg,cell}(\lambda)$ the harmonic spectrum of the cell background. Eq. (5.3) indicates that the cell background and gas spectrum simply add.

The resolution of detection in terms of concentration c_{res} (mixing ratio, unit: 1) is given by:

$$c_{res} = \frac{a_{res}}{\alpha_c \, l} \tag{5.4}$$

α_c is the peak gas absorption coefficient (unit: 1/m) in the scanned wavelength range and is an intrinsic property of the gas species. The absorbance resolution a_{res}, i.e. the smallest fraction of absorbed light power that can be resolved. When the absorption line to be detected is fixed, c_{res} is basically given by the ratio between a_{res} (unit: 1) and the interaction length l.

a_{res} consists of noise resolution $a_{res,noise}$, cell background resolution $a_{res,cell}$ and laser background resolution $a_{res,laser}$. Therefore, it is influenced by the following factors:

- noise: $a_{res,noise}$ is influenced by the noise power density S_{yy} on the measured spectra (see Eq. (6.34)) and therefore also by the absolute cell attenuation $T_{0,cell}$, because the signal to noise ratio depends on the light power arriving at the detector. The noise can be reduced by lowering the measurement rate. If the filtering effect by a linear curve fit is taken into account (observation matrix $\mathbf{\Psi}$, N spectral samples and measurement rate R, all introduced in the later section 6.1.3), the following expression is obtained:

$$a_{res,noise} = \sqrt{(\mathbf{\Psi}^T \mathbf{\Psi})^{-1}_{11} \, S_{yy} \, R \, N} \tag{5.5}$$

- cell background: strictly speaking, $a_{res,cell}$ is given by the result of the linear curve fit applied to the cell background. However, the filtering effect is neglected, because $\sigma(H_{n,bg,cell}(\lambda))$ is simple to measure (section 5.3.3) and is a good approximation for the absorbance resolution after the curve fit.

$$a_{res,cell} = \sigma \left(\left((\mathbf{\Psi}^T \mathbf{\Psi})^{-1} \mathbf{\Psi}^T \, H_{n,bg,cell}(\lambda) \right)_1 \right) \approx \sigma(H_{n,bg,cell}(\lambda)) \tag{5.6}$$

- laser background (spectral baseline due to nonlinearity of the laser P-I-characteristic): as for the cell background, the absorbance resolution from the laser background $a_{res,bg,laser}$ is exactly given by the result of the linear curve fit applied to the laser background P_n/P_0. This again is approximated as the standard deviation on the second harmonic laser background for the same reason.

$$a_{res,laser} = \sigma \left(\left((\mathbf{\Psi}^T \mathbf{\Psi})^{-1} \mathbf{\Psi}^T \, P_n/P_0 \right)_1 \right) \approx \sigma \left(P_n/P_0 \right) \tag{5.7}$$

  Here P_n denotes the n-th harmonic component of laser amplitude modulation (also given in Eq. (6.25)).

In contrast to noise, the laser background and cell background can not be eliminated by averaging over time. Both are deterministic structures, which, however, change

slowly during the measurements. To subtract them from the measured spectrum, additional measurements including venting with non-absorbing gas are required, which increases setup complexity and introduces dead times or is even impossible to realize for in-situ measurements.

5.2 Requirements on the design of the optical cell

According to Eq. (5.2), Eq. (5.3) and Eq. (5.4), the requirements for a high-sensitivity optical gas cell are:

- Long interaction length l between gas medium and light Eq. (5.4).
- Smooth spectral background of the gas cell, i.e. $A_{bg,cell}$ or $H_{n,bg,cell}$ as close as possible to zero, so that a_{res} is minimized (Eq. (5.6)). Specifically, the frequency components of the cell background spectrum should not be in the passband of the WMS filtering (for explanation see Fig. 5.4 and later section 5.3.2).
- Sufficient high cell transmission, i.e. $T_{0,cell}$ value should be high enough to guarantee laser RIN noise is dominating detector noise. Assuming an laser output power of 1 mW, a μW range power arriving on detector is sufficient for NIR range, giving a minimum $T_{0,cell} = 0.1$ %. In this case, laser RIN noise is dominant and no signal to noise ratio improvement by increasing laser power is possible. For detailed discussion see later section 6.1.2 or Fig. 6.6,.

Further requirements are:

- Small sample volume (ml range) required to fill the gas cell.
- Mechanical stability and robustness, easy-alignment and no alignment drift over time. For applications like in-situ combustion optimization, the cells must be robust against thermal cycles, condensation and contaminations.

5.3 Cell spectral background

In the following section, analysis and characterization methods of the cell background are developed:

5.3.1 Origin of the spectral background

Generally speaking, the spectral background of an optical cell originates always from interference of different optical modes. There are several modes propagating in the optical cell. Each mode has a different propagating path, resulting in different loss mechanisms or back-reflection coefficients, which is possibly wavelength dependent. For Fabry-Perot etalons, interference is created by reflections from both surfaces, but with an exponentially decreasing amplitude. For fibers, there is also probably mode dependent back-scattering at the end of the fibers or mode-dependent incoupling losses. The fiber ending is a waveguide discontinuity, which results in backscattering. In case of two optical paths or modes, the optical interference has a free spectral range (FSR) [63] of Δf:

$$\Delta f = \frac{c}{n\,OPD}, \tag{5.8}$$

where c is the vacuum velocity of light and n is the refractive index of light in the medium. OPD is called the optical path difference of light paths. By dividing OPD by light velocity, the time difference of two paths is obtained. For second harmonic detection, the interferences with a FSR corresponding to 4-6$\times\gamma_L$ (usually 10 GHz) are least attenuated (see explanation in next section 5.3.2). This is because the wavelength modulation amplitude is adjusted to be 2-3$\times\gamma_L$ because then the maximum signal is obtained. The FSR of 4-6$\times\gamma_L$ is then the dominant frequency component of the second harmonic signal. Therefore, interference with FSR of 4-6$\times\gamma_L$ is difficult to be eliminated with a filtering method without losing information of the wanted signal. At atmospheric conditions 4-6$\times\gamma_L$ is approximately 10 GHz and corresponds to 3 cm OPD in gas and 2 cm in glass (n=1.5).

The following origins of interferences could be identified within the frame of this work:

1. Reflections between parallel optical surfaces.
   A) between laser chip/window and photodiode chip/window (Fig. 5.2(a))
   B) inside optical components such as lenses or windows (Fig. 5.2(b))
   C) between laser/photodetector to lens/window (Fig. 5.2(c)).

   Recalling the worst OPD of 2-3 cm, it is concluded typical laser/detector geometries have to be designed very carefully and optical components with optical thickness or spacing of 1-1.5 cm should be eliminated.

2. Multiple paths of reflections on a diffuse reflector, causing wavelength dependent laser speckle pattern on the photodetector. It is diffuse-reflector specific and schematically shown in Fig. 5.3(a). There are two types of 'speckle pattern' [64, 65]: 'subjective' and 'objective' speckle pattern. A 'subjective' speckle is generated if a lens is used to image the diffuse surface to the photodiode. In this case, the interfering light beams have optical path length differences in $\leq$ mm range and result in fringes with much larger FSR compared to 'objective speckle' where no imaging optics are used. Interference created from the diffuse reflector is also called 'speckle noise'.

3. Optical interferences due to diverse propagating paths/modes in a waveguide. It is also called 'modal noise'. For a multimode fiber, the optical fringes have OPDs corresponding to the optical path length differences of all fiber modes (Fig. 5.3(b)). Therefore, the spectral background of a highly multimode fiber is a combination of a large amount of optical fringes with different FSR in a possibly large span.

One possibility of cell background elimination is signal processing, e.g. filtering and curve fit. This is carried out in the sensor system and is very efficient if the FSR of the interference to be filtered does not match the frequency components of the measured signal, i.e. for OPDs much larger or much lower than 2-3 cm. The second possibility is to reduce the side-mode generation, this includes eliminating coupling elements, lenses, windows or at least use anti-reflection coatings for the optical elements, using 'strictly' single-mode fiber i.e. only one possibility for light propagating in the fiber. The third possibility could be to generate many modes with comparable amplitude and statistical phase, which will partially cancel each other out and may result in a smooth cell transmission. The mode distribution may further be randomized by using mechanical vibration of optical elements.

(a) Reflection between laser diode and photodiode: OPD $= 2\,n\,l$, with $n = 1, 2....$ It corresponds to a multiple of twice the optical path length l, due to the back-and-forward reflections between the laser and photodiode. The FSR of this etalon type is usually much smaller than the gas absorption width, because $2\,n\,l \gg 3$ cm. It is therefore easily filtered by signal processing e.g. curve fit.

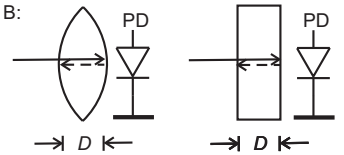

(b) Reflection inside optical elements e.g. lens/window, D: thickness of the optical elements. The OPD $= 2D$ can be in the order of a few cm, which is most disturbing the measurement. It can be overcome if very thin lenses/windows ($<$ mm) are used with appropriate AR coatings.

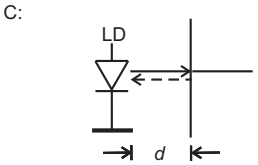

(c) Reflection between laser diode/photodiode and lens/window. The OPD $= 2\ d$ with d being the distance between laser chip/detector chip and window/lens, which is typically in the few 100 μm range (easy filtering) or in the cm range (most disturbing). It can be lowered by using tilted windows together with AR coatings.

Fig. 5.2: Various types of optical etalon formation by parallel surfaces in an optical cell. Depending on the distance of the surfaces the OPD of interference is given.

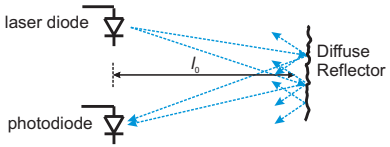

(a) Fringes due to speckle noise, for a diffuse reflector geometry. For 'subjective' speckle noise (using a lens to image the diffuse surface to the photodiode), the interfering light beams have OPDs in $\leq$ mm range

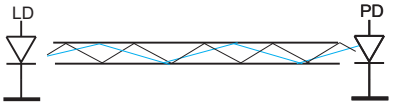

(b) Fringes due to a multitude of light propagating paths in a fiber ('modal noise'). The different fiber modes interfere and result in non-smooth fiber transmission. Due to the many different OPDs between the modes, also fringes with OPD $= 2, \ldots, 3$ cm may exist.

Fig. 5.3: Interference due to several light propagation paths.

5.3.2 Cell background on the second harmonic spectrum

'Cell background' is interference phenomenon on the cell transmission. However, in literature and also in this work, detection of the second harmonic spectrum is carried out. The question is how the cell background appears on the harmonic spectrum? Detection of second harmonic yields approximately the second derivative of the trans-

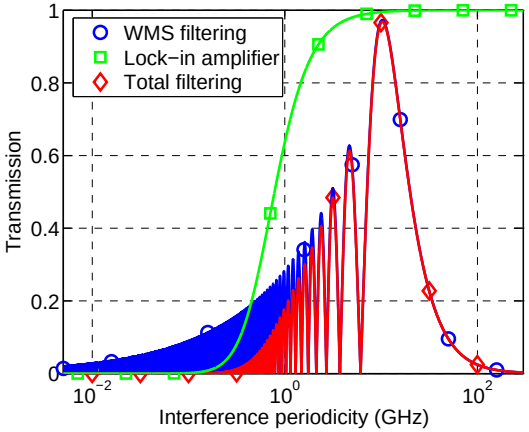

Fig. 5.4: The filtering achieved by wavelength modulation spectroscopy with typical wavelength modulation amplitude λ_a of 5 GHz (blue curve with circles) and by the filter inside the lock-in amplifier in a typical system (green curve with rectangles). The product of both (red curve with diamonds) gives the relationship between the measured second harmonic and the transmission spectrum in the frequency domain.

mission spectrum, or more exactly according to Hangauer, a band-pass filtering of the transmission spectrum [16]. The relationship between $H_2(\lambda)$ and $T(\lambda)$ is shown in Fig. 5.4: the Fourier transform of the detected second harmonic is the product of the Fourier transform of the detected transmission spectrum and a 2^{nd} order Bessel function [16]. If additionally low pass filtering in the lock-in amplifier (SRS, model SR830[66]) is taken into account, the following formula is obtained:

$$\mathcal{F}\{H_2(\lambda), k\} = \mathcal{F}\{T(\lambda), k\}\,(-2)J_2\,(2\pi\lambda_a\,k)\cdot\frac{1}{(1+i2\pi k\tau\beta)^n} \tag{5.9}$$

where λ, k denote wavelength and wavenumber, and λ_a denotes modulation amplitude in wavelength. λ and k are conjugate variables of the Fourier transform $\mathcal{F}$:

$$\mathcal{F}(f(\lambda), k) = \int_{-\infty}^{\infty} f(\lambda)\,\exp(-2\,i\pi\lambda\,k)d\lambda. \tag{5.10}$$

The filter in the lock-in amplifier is a n-th order low pass with its cutoff frequency depending on the lock-in time constant τ (unit: s) and the spectrum sweep rate β (unit: nm/s). The typical values are: $\tau = 1$ ms, $\beta = \lambda_a\,16$/s, $n = 4$ (24 dB/oct). The spectral features on the transmission spectrum are partially attenuated by detecting the second

harmonic spectrum, which, however, keeps the interferences with FSR corresponding to the dominant frequency component of the recorded harmonic spectrum. The interference on the second harmonic is thus relatively narrowband even if broadband interferences on the transmission spectrum exist.

As explained before, the wavelength modulation amplitude is chosen for maximum amplitude of the harmonic spectrum, which is λ_a =2-3γ_L depending on whether the amplitude or peak to peak amplitude should be maximized [17, 14, 67]. In the experiments the modulation amplitude λ_a was thus set to approximately 5 GHz at all wavelengths (HWHM typically 1-2 GHz).

5.3.3 Characterization method of the spectral background

The 'cell background' characterization is done in the following procedures with the setup shown in Fig. 5.5. The cell background is characterized with wavelength modu-

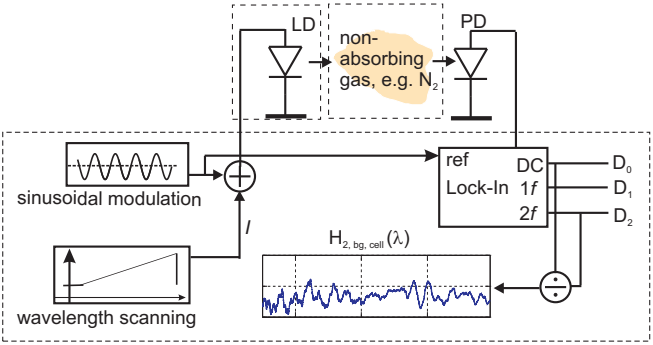

Fig. 5.5: The standard experimental setup for characterization of the cell background. The experimental setup for second harmonic generation is applied with a nitrogen filled cell, so $H_{2,bg,cell}(\lambda)$ is measured. Strictly speaking, the laser background and the cell background are simultaneously measured. However, the laser is selected so that the amplitude of its background is negligible compared to the cell background.

lation spectroscopy, with which the gas absorption is measured. The individual steps are outlined as follows:

- The cell is purged with a certain gas with absorption lines at the scanned wavelength.
- The WMS modulation amplitude λ_a is adjusted to 5 GHz by maximizing the second harmonic gas absorption line amplitude, and kept constant for the later measurements for cell background. The absorption features also allow for an initial determination of the wavelength scale.
- The cell is purged with nitrogen and the second harmonic spectrum of the cell is recorded and optionally sweep averaged to remove noise. The averaged value is then the sum of cell background and laser background. The utilized laser is selected by a previous characterization for a laser background of below 10^{-5}, so that the cell background dominates. However, the constant offset of the laser background is not removed.

5.4 Single-reflective cell: diffuse reflector

For in-situ gas measurement in harsh conditions, robust cells are needed. Harsh conditions means thermal cycles e.g. in a gas furnace, condensation and dirt. Due to thermal cycles, the cell alignment is not easy to maintain during life time, which will result in the loss of detector power and possibly an increase of the cell background due to additional unwanted reflections. Condensation/contamination of optical surfaces causes low cell transmission. In case of condensation, additional intensity noise may be given by moving waterdrops. Parts of this section has been published within the frame of this work in [68, 69].

Single-reflective optical cells are one of the simplest variants of the optical gas cells. The laser light is reflected by a diffuse reflector Fig. 5.6(a) or a spherical mirror Fig. 5.6(b) to the photodetector. The diffuse-reflector based cell is a new type of cell which is not common in literature. For compact cells, as examined here, $l = 2\,l_0$ and $l_0 = 5, \ldots, 10$ cm are used, with l_0 being the cell length. In contrast to the established spherical mirror cells, the diffuse reflector offers unique features in terms of robustness in harsh conditions. A diffuse reflector for the near infrared range can be made of anodized aluminum or sand-blasted aluminum.

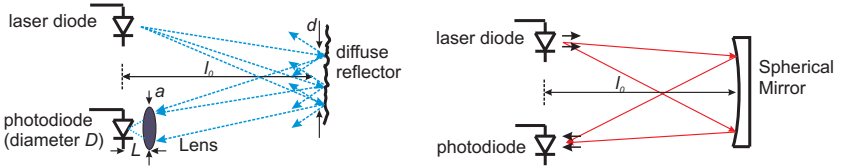

(a) Diffuse reflector based cell

(b) Spherical mirror based cell

Fig. 5.6: Schematic figures of (a) a diffuse-reflector based and (b) a spherical-mirror based single-reflective cell. For the diffuse-reflector based cell, the lens with aperture a in distance L of the detector (diameter D) serves as an optical light collector and enables detection of a higher light intensity because the effective area of the detector is significantly enlarged. According to the calculations using Eq. (5.11), the spectral background due to speckle noise is very low in the 10^{-6} range. For a spherical mirror based cell, laser diode and photodiode should be both in the focal plane of the mirror. Therefore, this cell type is very sensitive to alignment, but has an overall high transmission.

5.4.1 Thermal cycles

A significant advantage of a diffuse reflector lies in the simplicity of alignment: almost no alignment is required and optical setup changes due to thermal cycles can be tolerated. This is because even if the alignment changes during the thermal cycles, always the same amount of light is arriving at the photodetector and the cell background stays approximately the same. On the contrary, focusing the light on the photodetector by a spherical mirror is very alignment-sensitive, which is difficult to maintain with thermal cycles.

5.4.2 Cell spectral background

The measured second harmonic spectral background $H_{2,bg,cell}(\lambda)$ for the diffuse reflector based cell is shown in Fig. 5.7. The wavelength is tuned by laser temperature, which is given as x-axis. The intensity fluctuation on $H_{2,bg,cell}(\lambda)$ has a peak to peak amplitude of 10^{-5} with a dominant FSR of 10 GHz. By using the theory of section 5.3.1, the fringes are probably originated by the Fabry-Perot etalon between laser chip and the laser window ($\sim$ 1.5 cm distance, see Eq. (5.8)) (Fringe source: 1C, Fig. 5.2(c)). The etalon between laser diode and photodiode has a much smaller FSR and is already filtered with a curve fit.

The baseline fringes due to diffuse reflector i.e. speckle noise (Fringes source: 2, Fig. 5.3(a)) is thus below 10^{-5} and is also expected to stay stable during the time. This may not be the case for a spherical mirror based cell when a drift of adjustment occurs and the amount of back-reflected light from the detector surface interferes. The low speckle noise can be also explained theoretically. According to Hodgkinson [65], the speckle noise, i.e. the total fluctuation during the wavelength tuning for second harmonic detection is theoretically:

$$\sigma(H_{2,bg,speckle}) = \frac{1.4\pi\, h\, \lambda_a}{\sqrt{N}\, \lambda^2} \tag{5.11}$$

with h the standard deviation of the roughness of the surface, which basically gives

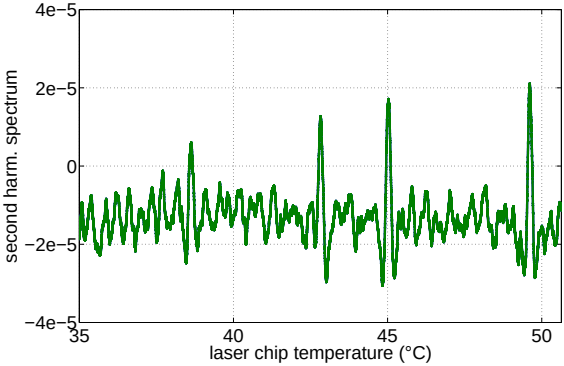

Fig. 5.7: The measured cell background $H_{2,bg,cell}$ of the diffuse-reflector based cell. The lasing wavelength is around 763 nm and was varied by changing the laser chip temperature (tuning coefficient 0.06 nm/K). The etalon fringes have a peak to peak value of 10^{-5} and corresponds to a resonator length of 1.5 cm caused by parallel surface between laser and window. The fringes are distorting the gas measurement and limiting the resolution, because their frequency component overlaps with the dominant frequency component of the wanted signal (indicated by the residual O_2 absorption lines at 38 °C, 43 °C, 45 °C and 50 °C. .

the length difference between several paths of the light propagation. N is the number of the speckle points on the detector surface and λ the detection wavelength. λ_a is the WMS modulation amplitude and typically set to 5 GHz in frequency scale at

atmospheric conditions. For sand-blasted aluminum h is in the μm range according to a measurement with a profilometer. N is given by the squared ratio of the detector diameter D and the average speckle diameter ϵ [65]:

$$N = \left(\frac{D}{\epsilon}\right)^2 = \left(\frac{Da}{1.2\,L\,\lambda_0}\right)^2 \qquad \text{'subjective speckle'} \qquad (5.12)$$

$$= \left(\frac{Dd}{1.2\,l_0\,\lambda_0}\right)^2 \qquad \text{'objective speckle'} \qquad (5.13)$$

For 'objective' speckle, a/L is the ratio of the aperture of the lens and its distance to the photodiode and for 'subjective' speckle d/l_0 is the ratio of the diameter of the lightened part of the diffuse reflector and its distance to the photodiode [65]. Applying typical values ($a = L = 1$ cm, $D = 3$ mm, $d = 3$ cm, $l_0 = 10$ cm, $\lambda_0 \approx 1$ μm), N is in the order of 10^6, which gives for both subjective and objective speckle a spectral background $\sigma(H_{2,bg,speckle})$ in the order of 10^{-6}. The theoretical detection limit of the diffuse-reflector cell based sensor is very good. The 'subjective' speckle is relevant here, because the diffuse reflector is imaged to the detector by the lens. Furthermore, the 'subjective' speckle noise has much larger FSR compared to gas absorption line width, which is easily filtered (section 5.3.1). The examined cell, however, is currently limited by interference of the laser window. The calculation shows that a significant improvement should be possible before the 'speckle noise' becomes dominant.

5.4.3 Contamination and condensation noise in furnaces

The hot and humid combustion gas causes condensation on colder surfaces like the laser window, lens and the reflector. It turned out that an additional diffusion by water droplets has less impact on diffuse reflector as for a focusing optic like a spherical mirror. According to the measurements, the power decreases by a factor of 5 due to condensation for diffuse reflector based cell, whereas the power decreases by at least a factor of 50 applying the spherical mirror. Additionally, condensation causes intensity noise because the waterdrops move on the optic surfaces: even at a constant laser intensity, the detector receives an intensity noise. The relative intensity noise spectrum is recorded and shown in Fig. 5.8. It has a lowpass first order behavior with a cutoff frequency of 5 Hz. Therefore it has low influence on the measurement because power normalization is done in 1 msec intervals for each measured wavelength point separately.

During a long-term test over more than one year in an operated gas furnace, the sensor using a diffuse-reflector based cell showed no significant drift (published in Ref. [70]). The absolute transmission $T_{0,cell}$ decreased by about 25 % in the first few months and then remained stable, which shows that no contamination exists in gas furnaces (Fig. 5.9, blue curve). The situation is different in oil furnaces where strong contamination exist. After few months the transmission reduced to 10 % due to contamination on the reflector as well as the detector and laser window (Fig. 5.9, red curve). This shows that additional means against contamination have to be applied to make the sensor suitable for maintenance-free operation over years. Contamination could be reduced by appropriate heating of optical surfaces. For spherical mirror the influence of contamination is much stronger, it may result in total vanishing of the photo current.

A brief comparison between diffuse reflector and spherical mirror is shown in Tab. 5.1 in section 5.8, together with other optical cells. Using single-reflective cell, absorbance resolution of $a_{res} = 10^{-5}$ is achieved. By assuming typical optical pathlength of 20 cm,

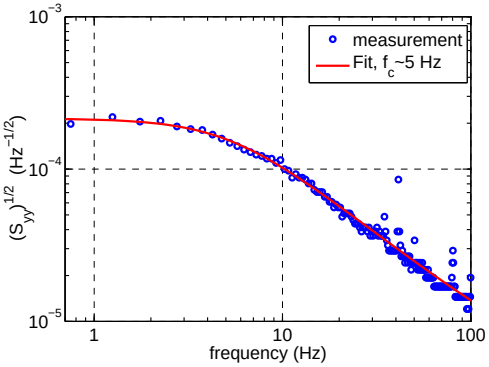

Fig. 5.8: The square root of the noise power density S_{yy} (unit: $1/\sqrt{Hz}$) of condensation caused intensity noise. The fit function for measured noise power density is $\sqrt{S_{yy}} = a/\sqrt{1+(f/f_c)^2} + b$, with a and b being scaling and offset constant and f_c is the cutoff frequency with a fitted value of 5 Hz. The intensity noise caused by condensation has therefore a lowpass behavior first order or is approximately $1/f^2$ noise.

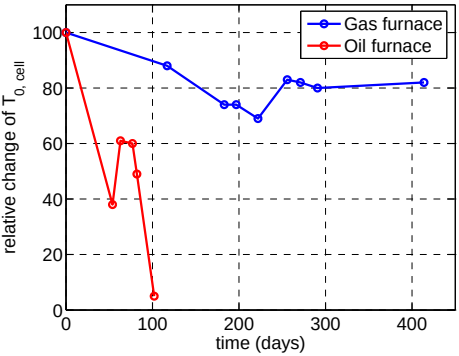

Fig. 5.9: The relative change of the cell transmission caused by contamination of the diffuse reflector cell in gas furnace (blue curve) and oil furnace (red curve). The cell transmission stabilized after few months in the gas furnace and after that remained stable showing the desired long-term stability in harsh environments. In the oil furnace contamination is far more severe. Although measurement at 10 % transmission is still possible, further contamination over longer periods is expected (measurement done by A. Spitznas, Siemens SBT, Rastatt).

absorption coefficient resolution of $\alpha_{res} = 5 \times 10^{-7}$ cm^{-1} is ultimately obtained. To achieve a higher sensitivity, longer optical pathlength is needed. For this a multipass cell is conventionally utilized.

5.5 Multipass cell: Herriott cell and White cell

The basic idea of the multipass cell is an extension of optical path length l by multiple reflections on the spherical mirrors on both sides of the cell. The optical path is given by:

$$l = l_0 \, (2\,N + m) \tag{5.14}$$

with l_0 being the cell length and N the number of the light spots on one side of the mirror (for white cell, the object mirror). Each light spot is related to two light paths (bidirectional reflections) and additionally the light path given by the in- and outcoupling. We have $m = 1$ for the Herriott cell [71] (when entrance and exit are on opposite sides of the cell) and $m = 2$ for the White cell [72]. The spot number N is limited by the ratio between the mirror area (reflecting area) and the size of the spot. By overlapping of two light spots, optical interferences will occur. To achieve long optical path length, large N and/or l_0 are required, which results in an increased sample volume to fill the cell. Here a specifically designed Herriott cell, optimized for low volume, by the Fraunhofer Institute for Physical Measurement Techniques (IPM) is investigated ($l = 4.9$ m, $l_0 = 10$ cm, $N = 24$, $V = 40$ ml).

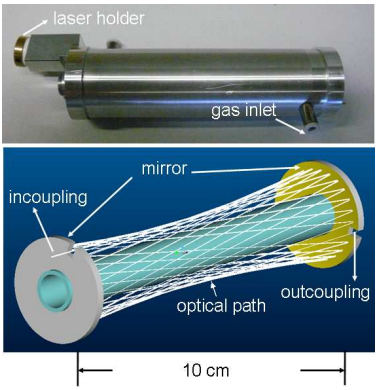

(a) Structure figure and photograph of the Herriott cell designed by Fraunhofer IPM [73]. It is a traditional design employing 5 cm radius spherical mirrors and a base length of 10 cm. 24 reflections give a pathlength of 4.9 m (l_0= 10 cm, $N = 24$, $m = 1$). The incoupled light is required to be a focused beam with focal point exactly between the mirrors.

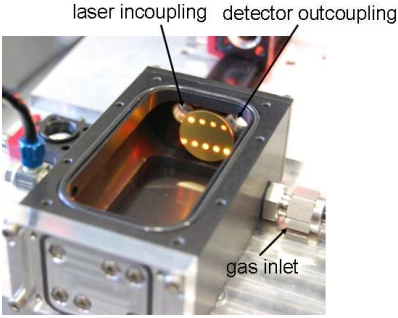

(b) Photograph of the White cell designed by Fraunhofer IPM [73]. It has an optical path length of 1.56 m and employs three spherical mirrors. $N = 9$ reflections give a pathlength of 1.56 m ($l_0 = 7.8$ cm, $N = 9$, $m = 2$). Compared to the Herriott cell the incoupled light is not required to be focused which allows for direct coupling of the laser without additional lenses.

Fig. 5.10: The design and photograph of the Herriott cell and White cell

As all conventional Herriott cells, it utilizes a spherical mirror and the light spots lie on a circle at the perimeter of the mirror (Fig. 5.10(a)). An inner pipe is used

to reduce the needed sample volume to fill the cell. Astigmatic Herriott cells using elliptical mirrors offer more optical pathlength because the light pattern can cover the whole mirror in a rectangular pattern. However, it is more difficult to manufacture. A 76 m optical path length in 500 ml volume cell is achieved [4]. For Herriott cell, a laser collimation optics is necessary to focus the light into the center of the cell with a focal length of $l_0/2$.

The characterized spectral background is shown in Fig. 5.11. An interference with amplitude of 10^{-4} and $\Delta f = 10$ GHz is visible. This corresponds to 3 cm pathlength difference (Eq. (5.8)). Thus the distance between laser and lens is identified as the cause. The AR coating on the lens is limiting but not completely preventing interferences being created. The possible solution for this problem is to use a lens with shorter focus length and move it very close to the laser ($\sim$100 μm). Other possibility is to use a mirror-based objective to focus the laser light to the cell, as done in a commercial high precision laser based instrument [4]

In contrast to the Herriott cell, the White cell is also suitable for light source with large divergence. This extended feature gives an advantage of the White cell: no collimation optic like lens or mirrors are needed, which are the limiting factor for the Herriott cell. The spectral background of the investigated White cell is thus much better and below 10^{-5} (Fig. 5.11(b)), but with a lower optical pathlength than the Herriott cell ($l_0 = 0.78$ cm, $l = 1.56$ m, $N = 9$). Also, 3 instead of 2 mirrors are utilized, which possibly increases the cost.

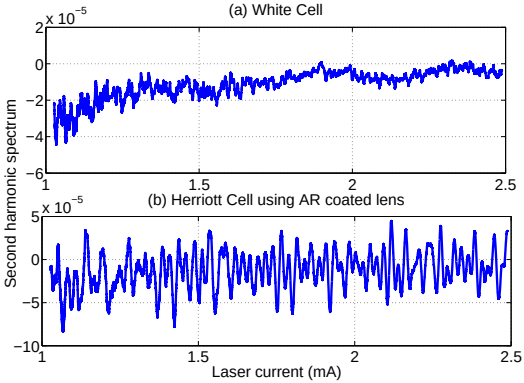

Fig. 5.11: The spectral background $H_{2,bg,cell}$ of White cell (a) and Herriott cell (b). The laser current corresponds to wavelength with a coefficient of 0.6 nm/mA. The wavelength is around 763 nm. The origin of the high background of the Herriott cell is found to be a reflection between the parallel surface between laser and lens (distance: 1.5 cm, interference type 1C in Fig. 5.2(c)). The lens is needed for collimation, which is required for the Herriott cell to operate correctly. The White cell has a background with peak to peak less than 10^{-5}.

In general, for multipass cell, the cell background, cell output power and optical path length are very dependent on careful alignment. Long term stability and robustness in harsh conditions is very hard to achieve because of the possible misalignment and high sensitivity to contamination on the mirrors. The cell transmission $T_{0,cell}$ is R^{2N}

with R being the reflectivity of one mirror. It is clear, that the transmission is strongly decreasing even if contamination only slightly reduces the mirror reflectivity. Therefore, another possibility of optical cell - fibers is investigated here. It provides long optical path length, and has the potential for sensitive and robust gas sensing. Compared to multipass cell, the fiber-based sensor should provide superior properties except for the contamination issue where the fiber is also expected to be sensitive to.

5.6 Photonic crystal fiber based cells

Telecommunication single-mode fiber can be used for gas sensing via evanescent field when the fiber cladding is removed. However, the power fraction of light in air (evanescent field) is very tiny and sensitive to the fiber conditions e.g. bending and is therefore not well defined. It is expected that a single-mode fiber has theoretically no spectral background, because no interference between different fiber modes can occur. Photonic crystal fibers (PCFs) are fibers with a periodic array of microscopic air holes that run along the entire fiber length [74]. The PCFs can be designed single-mode and the laser light is then confined in the air holes, so that certain interaction between gas and light mode in the air holes exist.

There are three types of photonic crystal fibers investigated in this section: single-mode suspended-core PCF [75], single-mode hollow-core PCF (HC-PCF) [74] and the multi-mode Kagome fiber. Silica suspended-core PCF ('Mercedes fiber') (Fig. 5.12) is preferred for this application because of their simple design compared to traditional hollow core PCFs. Furthermore, it is easier to implement lateral gas inlets on it without destroying the microscopic structure of the fiber.

Parts of this section have been published in [76].

5.6.1 Fiber properties

The SEM figure of the suspended-core fiber is shown in Fig. 5.12, the tiny solid silica core is supported by three silica sheets. The light mode not only propagates in the silica core, but also extends to the air holes, with evanescent field. The fiber is fabricated by the conventional stack and draw process [75]. Three thin-walled capillaries drawn from silica tubes were stacked to put into a preform, which is then subsequently drawn directly into the final fiber.

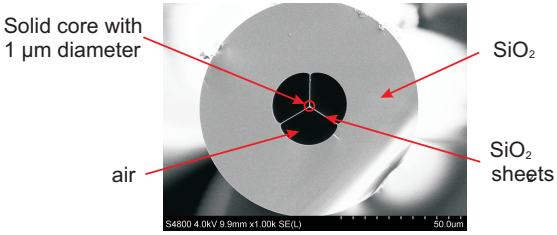

Fig. 5.12: SEM figure of 'Mercedes' PCF cross-section (fabricated and image taken by Max-Planck Institute in Erlangen). The silica core with a diameter of approx. 1 μm is supported by three silica sheets. The light mode not only propagates in the silica core, but also in the air holes, with evanescent field, which allows for gas-sensing.

Existing gas measurements with 'Mercedes' was only done for demonstration purpose e.g. 100 % acetylene is filled in the fiber [77]. No characterization of the sensor sensitivitity is done in literature so far. The effective interaction length l is the product of the physical fiber length l_0 and power fraction of light in the air holes Φ: $l = l_0\,\Phi$. Both Φ and the fiber spectral background are determined in the following.

5.6.2 Optical setup

Because of the small divergence of VCSELs (FWHM: 10-20 degrees), they are very attractive candidates for direct coupling with fiber. Optical coupling elements are also eliminated, allowing for robust and miniaturized gas sensing and simultaneously eliminating possible sources of additional cell background. Light emitted by the VCSELs

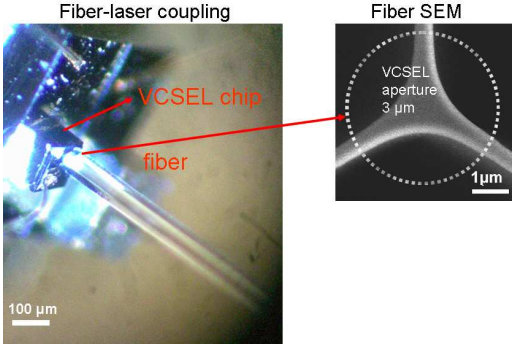

Fig. 5.13: The image of incoupling between laser chip and fiber. The SEM of the fiber cross section is also shown, with a circle indicating the aperture size of VCSEL. The core to aperture area ratio basically determines the incoupling efficiency, which is around 10 %.

was launched directly into the core of the PCF, which is placed at < 10 μm distance from the VCSEL. Typical launch efficiencies were 13 % (763 nm) and 15 % (1674 nm), which are in good agreement with surface area ratio between VCSEL and fibre core (Fig. 5.13). The laser has no window and is placed in front of the fiber with a distance of less than 10 μm. The detector is tilted and placed in a distance < 1 mm, both to avoid interference type 1C (see Fig. 5.2(c)).

5.6.3 Cell interaction length

The measured mode intensity profile of the fiber (Fig. 5.14) shows an increase of the extension of the mode with increasing wavelength. But it is difficult to determine the power fraction of the light in the air hole because the positions of the legs are not accurately known from the measured intensity profile. However, if the gas concentration and fiber length (2 m) are exactly known, the power fraction of light in the air can be obtained by comparing the measured and theoretical (HITRAN) line strength (Fig. 5.15). Different gas at different wavelengths are measured and Φ is determined to be 7 % (763 nm, 100 % oxygen), 17 % (1674 nm, 10 % methane), 27 % (2004 nm, 10 % carbon dioxide), which is increasing with wavelength as expected. The compari-

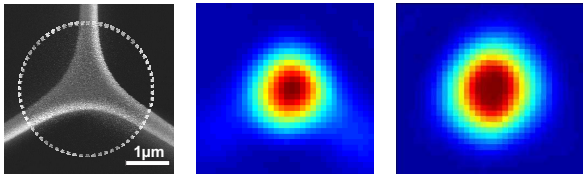

Fig. 5.14: (a) SEM of the air-suspended solid-core PCF with core diameter of 1 μm. (b) Measured mode intensity profile at the output of the fiber for 1674 nm and (c) for 2004 nm, recorded with a CCD camera. The scale of (b) and (c) is roughly equal to the scale of SEM plot. It can be seen that the power fraction of light in the air increases with wavelength. However, the images do not allow for precise determination of the field overlap. This is thus determined with a different method shown in Fig. 5.15.

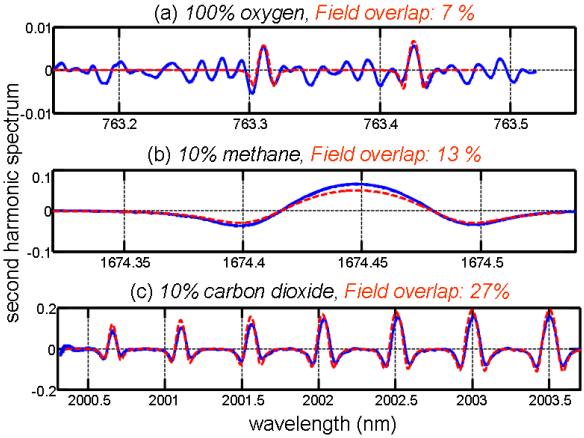

Fig. 5.15: Second harmonic spectra for different gases at different wavelength: (a) 100 % O_2 at 763 nm; (b) 10 % CH_4 at 1674 nm; (c) 10 % CO_2 at 2004 nm. Solid curves represent measurement data and dash curves the corresponding curve fit with HITRAN data. The comparison between measurement data and theoretial HITRAN data gives the power fraction of light in air holes Φ (summarized in Fig. 5.16).

son with simulation given in Fig. 5.16 is taken from [75]. This indicates that the light with shorter wavelength is more confined in the solid core. The simulation was done for fibers with slightly different core diameter (deviation 1-10 %), which could be the reason for the deviation between measurement and simulation.

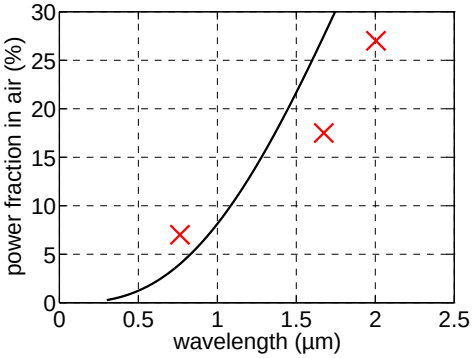

Fig. 5.16: The measured light power fraction in air Φ (from Fig. 5.15) as a function of wavelength (cross), which is compared with simulation [75]. It is clearly visible, that Φ can reach reasonable values well above 10 %, which is much larger than evanescent field of a standard single mode fiber.

5.6.4 Cell spectral background

The spectral background was found to have a peak-to-peak amplitude of less than 2×10^{-3} (Fig. 5.17) at three wavelengths, 763 nm, 1674 nm, 2004 nm. Since there are no coupling elements, it is obvious that the fiber itself is guiding multiple modes. The possibility of reflections from the starting surface of the fiber striking back to the laser is also excluded, because the interference periodicity does not change with distance between fiber and laser, the same is examined for the photodiode and the end of the fiber. The next question is where the multi-mode propagation comes from, i.e. is it transversal multimode or longitudinal multimode. In case of the second, is there an unwanted cladding mode? Transversal mode i.e. polarization mode and cladding mode could be easily filtered by using a polarization filter or immersing the fiber into index matching liquid. Experiment showed that the spectral background:

- has no polarization dependency: polarization filter was put next to the laser to select certain polarization mode with no considerable effort.
- is not caused by outer cladding mode interfering to core mode: the fiber was immersed into index-matching liquid with the purpose that the jacket mode is coupled out while the core mode is kept to propagate in the fiber. However, the spectral background level did not change.
- is dependent on the coupling condition: if the laser chip is coupled non-centrally to the fiber, the spectral background increases.

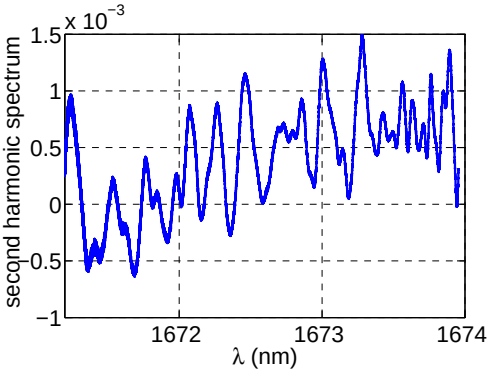

Fig. 5.17: The spectral background $H_{2,bg,cell}$ of the suspended-core photonic crystal fibers, with an amplitude in the order of 10^{-3}. The background level is approximately the same for wavelengths between 763 nm and 2004 nm. Its origin was determined to be mode beating between the fundamental core mode and weak core modes. This case corresponds to interference type 3, Fig. 5.3(b).

- has dependency on fiber length: if the fiber length increases, the dominant FSR decreases as well.

It is therefore concluded that two or more transversal modes are guided in the tiny core and interfere with each other results in the high spectral background. For comparison: the standard telecommunication single mode fiber has also modal noise on the transmission function in the order of approx. 10^{-4} due to interfering with other polarization mode [78]. The modal noise will increase if the fiber is stressed or tightly wound. For telecommunication fibers, methods for compensating the unwanted distortions, including the fiber background, exist, to achieve a resolution of absorbance of 5×10^{-6}, however, a reference channel is needed [79, 80].

5.6.5 Maximum interaction length and gas exchanging time

As introduced before, the interaction length provided by the fiber is a very essential factor to tell the detection limitation. The maximum interaction length is limited by three aspects: fabrication, fiber attenuation and gas exchanging time. According to the coupling efficiency and minimum required cell transmission $T_{0,cell}$ (see section 5.1), the maximal attenuation by the fiber is around 20 dB (assuming the laser output power to be 1 mW and sufficient photodetector power to be 1 μW, incoupling efficiency approx. 10 %). The fiber length can therefore be up to 10 m or 100 m depending on the wavelength (763 nm: 0.2 dB/m, 1670 nm: 2 dB/m). The fiber can be fabricated with several kilometers [81], like the standard glass fiber, so the maximal fiber length is not limited by manufacturing. Because of the very small radius of the capillary, the gas exchange time gives a limitation of the maximum interaction length. The flow rate for ideal gas in the isothermal case in a capillary is covered by the law of Hagen-Poiseuille

and the gas exchanging time τ is approximately given by:

$$\tau = 16\,\eta \left(\frac{l_0}{r}\right)^2 \frac{p_i}{p_i^2 - p_o^2} \tag{5.15}$$

Where η is viscosity of the gas medium, typically: 17.8 μPa· s for most gases in air. p_i the input pressure and p_o the output pressure, l_0 is the fiber length and r is the radius of the capillary. Applying 1 bar pressure difference (input: 2 bar, output: 1 bar), the gas exchanging time for a 2 m PCF fiber with 12.5 μm diameter is ∼1 min, but this increases quadratically with the fiber length with constant pressure difference between both ends. The exchanging time can be lowered quadratically by extending the hole diameter or be lowered by implementing lateral gas inlets on the fiber. The gas exchange time decreases then proportionally to the hole number on the fiber. Therefore, to achieve minute gas exchanging time, at least 2 holes are to be implemented for 10 m fiber.

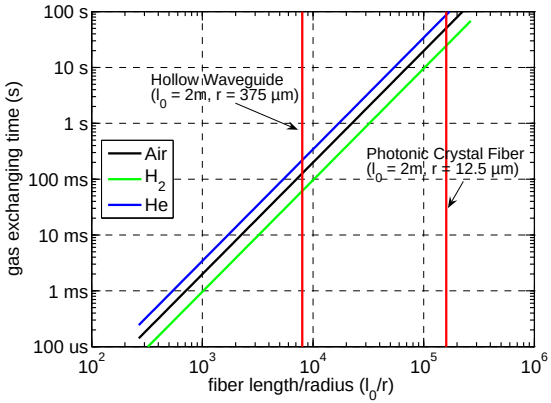

Fig. 5.18: The gas exchanging time in PCF ($l_0 = 2$ m, $r = 12.5$ μm) in comparison to hollow fiber ($l_0 = 2$ m, $r = 375$ μm), determined with the law of Hagen-Poiseuille (Eq. (5.15)). The exchange time has a quadratical dependency on fiber length and can reach very long times for the PCF due to the small holes. The time does not depend much on the substance, as all gases have a similar viscosity. The gas exchanging time may, however, be lowered if appropriate holes are implemented along the fiber.

5.6.6 Results on other PCFs

Other types of PCF such as the bandgap hollow-core PCF (HC-PCF) (Fig. 5.19) and Kagome fiber (Fig. 5.20(a)) are also investigated to provide a comparison to the 'Mercedes' fiber. HC-PCF is the traditional single-mode photonic crystal fiber and it is commercially available. Kagome fiber is a multi-mode fiber with its structure similar to the HC-PCF, except for the triangle hollow structures between hexagonal structures, where other light modes are also able to propagate in. Both of them provide a nearly 100 % overlap between gas and light, which is therefore interesting for gas sensing

applications.

Recorded mode intensity profile at the fiber end is shown in Fig. 5.20(b). However, random modulations in the order of 10^{-2} occur in the transmission of both fibers (Fig. 5.21 on next page). The HC-PCF is thus also not strictly single mode. At least two modes interfering resulting in the spectral features with a periodicity determined to be anti-proportional to the fiber length. The envelope of the interference is due to the filtering effect of WMS (see Fig. 5.4) and the slightly varying wavelength modulation amplitude λ_a during scanning caused by the nonlinear tuning behavior of the laser.

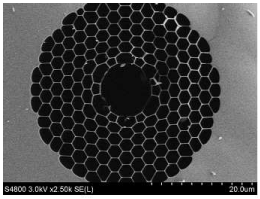

Fig. 5.19: SEM figure of bandgap hollow-core photonic-crystal fiber (HC-PCF)[82]. It consists of many small and hollow hexagonal structures surrounding by silica. There is a big air hole in the middle of HC-PCF (diamater ≈ 8 μm), where most of the light is propagating. The holes are however smaller than for the 'Mercedes' fiber, giving a longer gas exchange time and it is also technically more difficult to drill lateral holes on the fiber.

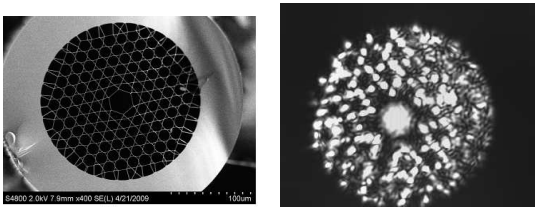

Fig. 5.20: (a) SEM figure [83] and (b) measured mode intensity profile of the multimode Kagome fiber (core diameter ≈ 20 μm). It is evident that the fiber supports many modes by observing the guided light in the modes at the triangular silica junctions between the hexagons.

5.7 Hollow capillary fiber based cell

In previous section it was shown, that 'single-mode' photonic crystal fibers are presently not strictly 'single mode' for gas sensing application. The beating of the fundamental mode and other weak core modes results in a fiber background in the order of 10^{-3} for the 'Mercedes' fiber and is even higher for the HC-PCF and the Kagome fiber. It is questionable if the background can be lowered to 10^{-5}, because even standard single mode fibers for communication applications exhibit a spectral background in the order of 10^{-4}, due to beating of the two polarization modes [78]. Therefore, the utilization of a highly multimode fiber is considered, with the idea that the interference

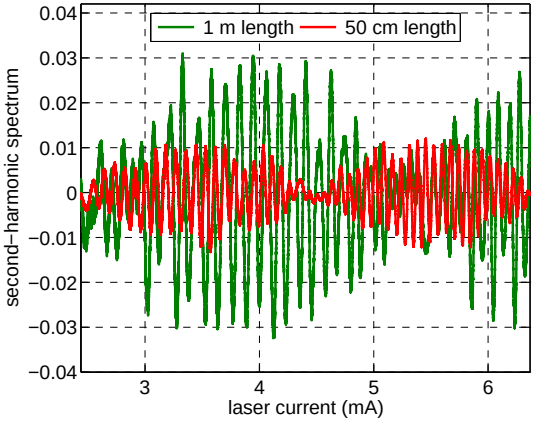

Fig. 5.21: The fiber background $H_{2,bg,cell}$ of 50 cm and 1 m HC-PCF. The laser wavelength is around 1680 nm and the tuning coefficient 0.4 mm/mA. The amplitude of the fiber background is the % range. The spectral features have a periodicity determined to be inversly-proportional to the fiber length. The envelope is caused by the WMS filtering, because the laser wavelength modulation amplitude slightly changes during wavelength scanning.

of thousands of modes may cancel out statistically and result in a rather smooth transmission function.

The most significant content of this section was published within the frame of this work in [84].

The hollow capillary fiber/ hollow glass waveguide (HGW) [85] was originally developed for transmitting CO_2 laser power in the 10.6 μm range [86] and YAG laser power at 2.94 μm [87]. It has an inner diameter of a few 100 μm to 1 mm. Recently, few gas/liquid sensing experiments with hollow glass waveguides have been reported in the literature: with quantum cascade lasers (QCL) for mid-infrared (MIR) sensing using coupling-elements like objective or off axis parabolic mirror [88, 89]; experiments show the concentration resolution achievable for Ethylene at 10.4 μm [88, 90, 91], but not at all clarify the nature of the limiting factors. Relevant aspects are missing in literature: no characterization of the fiber spectral background and its origin was done and no NIR laser based measurement was carried out so far.

5.7.1 Fiber properties

The hollow capillary fiber is an air or gas filled hollow waveguide, where the light is guided in the core by reflections on the AgI/Ag coating on the inner surface of the fiber. These fibers with inner diameters from 200 μm to 1000 μm as well as lengths up to 13 m are commercially available [85]. Here a fiber with 750 μm inner diameter (Polymicro, HWEA7501200) is used. Its structure is shown in Fig. 5.22(a) [86, 93]. The AgI coating has an optimized thickness of 0.3 μm for a minimal loss at a wavelength

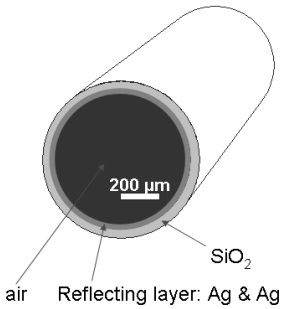

(a) The HGW with an inner diameter of 750 μm has a silica cladding and a thin metallic layer of Ag with a single dielectric film of AgI, both deposited inside the cladding to achieve a high reflectivity. The HGW is a highly multimode step-index fiber.

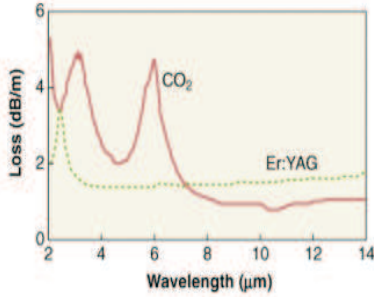

(b) The attenuation of light in hollow capillary fiber designed for transmitting of Er:YAG laser light (2.94 μm) and CO_2 laser light (10.4 μm) (taken from [92]).

Fig. 5.22: Schematic figure and attenuation of the HGW.

of 2.94 μm, which is closest to the desired wavelength range in our investigations [85]. The fiber shows an attenuation of 2 to 4 dB/m at 2 to 3 μm wavelength (Fig. 5.22(b)). This hollow glass structure has a very smooth inner surface compared to other hollow structures [85]. Its volume per optical interaction length is 400 μLiter/m, which is very small compared to conventional sample cells, e.g. a Herriott cell with a volume of 0.27 Liter for an optical path length of 36 m [94], but larger against the PCF volume for the same optical pathlength. The properties are summarized in Tab. 5.1 in section 5.8.

5.7.2 Maximum interaction length

The maximum interaction length given by a fiber can be limited by fabrication technology, fiber attenuation or gas exchanging time. Up to 13 m meter HGW is commercially available. Additionally, up to 24 dB attenuation is allowed for the HGW fiber, which is approx. 8 m in the near infrared range (assuming attenuation 3 dB/m, Fig. 5.22(b), assumed laser output power: 1 mW, and an in-coupling efficiency of 25 %. The incoupling efficiency is determined by the FWHM of the VCSEL and fiber (laser FWHM: 10 to 20 degrees, fiber FWHM ~10 degrees), The gas exchanging time is no limiting factor for the HGW: for 10 m fiber the gas exchanging time is in second range applying 1 bar pressure difference between fiber input and output (see Fig. 5.18). Therefore, the maximal fiber length is limited by the allowed attenuation. The situation is expected to improve significantly, if the fiber is optimized for the NIR or gas sensing is carried out at the wavelength the fiber is optimized for. Then fibers with the maximum manufacturing length can be used.

5.7.3 Cell spectral background

Because many physical effects such as backscattering at the end of the fiber, absorption in the coating or scattering inside the fiber are mode-dependent, the superposition of many fiber modes at the end of the fiber result in random modulation of the fiber transmission function (modal noise).

The cell background of HGW shows a tiny structure in the order of 10^{-4} (Fig. 5.23). The standard deviation $\sigma(H_{2,bg,cell})$ is $6{\times}10^{-5}$. This structure consists of many

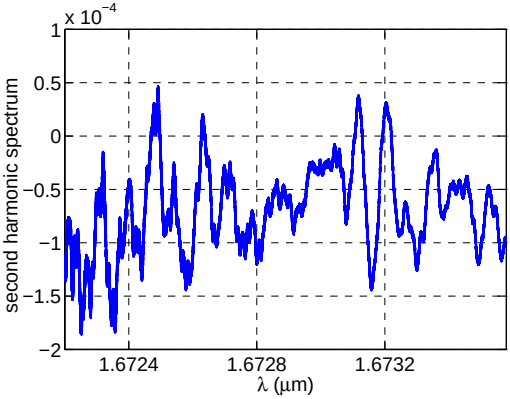

Fig. 5.23: The spectral background $H_{2,bg,cell}$ of a 3 m long bent HGW fiber (peak to peak $2{\times}10^{-4}$, standard deviation $\sigma(H_{2,bg,cell})$ is $6{\times}10^{-5}$). Spectral background is caused by interfering of different modes. The most dominant periodicity is 10 GHz, corresponding to the frequency least attenuated by second harmonic detection and also most disturbing the measurement (this case corresponds to interference type 3, Fig. 5.3(b)).

frequency components with a most dominant periodicity of approximately 10 GHz (0.1 nm @ 1.68 μm). This is also observed at $\lambda = 2.36$ μm. Structure with 10 GHz periodicity can be produced by an 1.5 cm long etalon. However, there are no parallel surfaces with a distance in this range that could form an etalon in our optical measurement system. The possibility of reflections from the start surface of the fiber striking back to the laser is also excluded, because the interference periodicity does not change with distance between fiber and laser. This excludes other sources of the spectral background except for the fiber itself causing the background: the fiber 'modal noise' on the transmission are broadband, while the WMS performs a selection of the 10 GHz interference due to its bandpass filtering characteristic (Fig. 5.4).

5.7.4 Analysis of spectral background and its improvement

Farfield observations and analysis

Since the spectral features are most likely resulting from the multimode character of the fiber, it is essential to know how many fiber modes are excited and also the corresponding amplitude and phase distribution at the fiber end. For this, the far-field under different conditions was investigated:

- straight fiber (20 cm) with centrally coupled VCSEL (Fig. 5.24(a)).
- straight fiber (20 cm) with non-centrally coupled VCSEL with 100 μm lateral displacement (Fig. 5.24(b)).

- bent fiber (3 m) with bend radius of approx. 15 cm (Fig. 5.24(c)).

The distance between fiber end to camera CCD chip is approx. 3 cm.

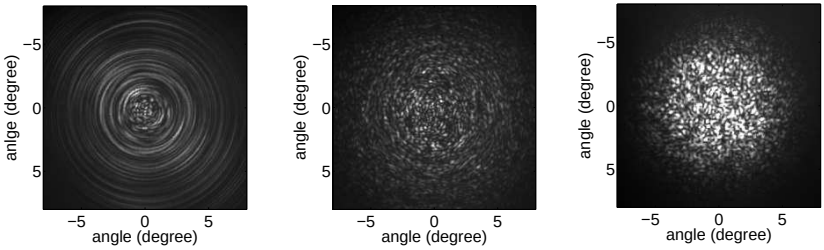

(a) 20 cm straight fiber, centrally coupled

(b) 20 cm straight fiber, 100 μm laterally displaced coupling

(c) 3 m bent fiber

Fig. 5.24: The farfield of hollow fibers directly coupled with VCSELs. For central coupling only the modes with Bessel function order 0 are excited. For the non-centrally coupled straight fiber and the bent fiber (any coupling) a speckle pattern is observed, indicating the propagation of all kinds of cylindrical waveguide modes.

Number of excited modes

In the case of the straight fiber with center coupled VCSEL, the farfield shows a ring structure, which indicates that only circularly symmetric modes are exited, i.e. only modes with Bessel function of order 0. For the straight fiber with laterally displaced coupling and for a bent fiber, a speckle pattern is obtained. It is a spatial intensity pattern, i.e. a spatially varying superposition of many modes - including higher order azimuthal modes [65, 95]. According to W. Freude [95], the maximum number of excited modes in a multi-mode fiber is theoretically determined by:

$$M = \left(\frac{2\pi}{\lambda} \tan(\theta) \cdot r \right)^2 \tag{5.16}$$

with r and λ denoting the radius of the hollow waveguide and the wavelength of the emitted light, respectively. According to Fig. 5.24(c) we determined the acceptance angle of the fiber θ to be approximately 6° (HWHM), which gives a maximum of 10000 modes propagating in the bent fiber and coupled out of it. Modes corresponding to angles much higher than the acceptance angle have very high losses and thus light in these modes does not propagate over the length of the fiber.

Statistic of modes distribution The spatial intensity distribution of speckle pattern caused by diffuse reflection is theoretically an exponential distribution [96]:

$$P(I) = \frac{1}{\langle I \rangle} \exp\left(-\frac{I}{\langle I \rangle} \right), \tag{5.17}$$

with $\langle I \rangle$ being the spatial mean value of the intensity and P the probability density function. After diffuse reflections, different light modes are uncorrelated to each other and the E-field strength of each light mode is orthogonal to each other, which results

in the Gaussian-distribution of the overall E-field. Intensity is the sum of squared real and imaginary part of the E-field and therefore, its distribution is an exponential distribution. The spatial intensity distribution of the recorded far-field of a 3 m bent fiber is plotted in Fig. 5.25 (red solid curve), which clearly shows an exponential behavior (blue dashed curve in Fig. 5.25). This gives an indication that the different fiber modes in the bent hollow waveguide are uncorrelated to each other and add with statistical phase and amplitude. This knowledge was employed for the simulation of the fiber farfield. The spatial intensity distribution of the far-field of a straight fiber with noncentral incoupling (Fig. 5.24(b)) was also found to be exponential.

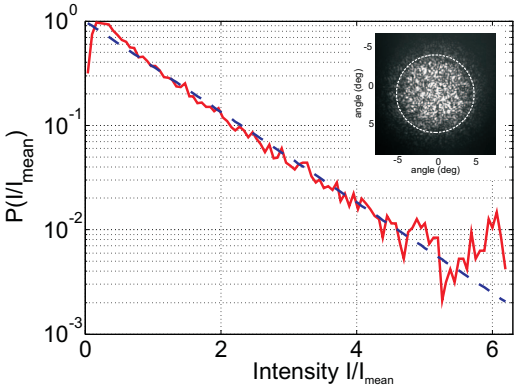

Fig. 5.25: The plot shows the probability density function P of the normalized intensity I/I_{mean} of the observed farfield of 3 m bent fiber (red solid curve) and the theoretical exponential intensity distribution of a speckle pattern (blue dashed line). The examined area is marked with a circle. The exponential distribution indicates independent fiber modes with similar amplitude and uniformly distributed phase shift. This causes a smoother fiber transmission than the beating of one strong and several weak modes as the case for PCF (Fig. 5.17).

Farfield during wavelength scanning If the integrated speckle intensity stays the same during the wavelength scan, the fiber transmission function should be smooth, i.e. $\sigma(H_{2,bg,cell}) = 0$. During the wavelength tuning, the fiber mode compositions change and therefore also their constructive or destructive superposition at a certain spot of the photodetector, i.e. the speckle pattern changes. The recorded speckle pattern changed slightly when the laser wavelength was tuned for several nm. The change at the perimeter is clearly observable, whereas in the center it is hardly noticeable. The possible reason is the following: speckle points at the perimeter are caused by interfering of light modes with very different propagation constants, leading to etalon fringes with small frequency spectral range (FSR). In the middle, the FSR of etalon fringes are relatively large - much larger than the wavelength range being tuned.

According to the law of energy conservation, the spectral features can appear if the photodetector does not collect all the light coming from the fiber end and/or mode-dependent losses exist. So the next step is to investigate the contribution of different in/outcoupling to the fiber spectral background, i.e. the dependence on the radial

incoupling position and dependence on partial integration of the fiber far-field.

Spectral background and incoupling

In the experiments shown in this section, we used a slightly tilted Ge photodiode (diameter: 3 mm) and a 1.68 μm VCSEL tuned to a wavelength range, where absorption due to ambient gases in the fiber with 3 m optical path length is less than 2×10^{-6}. Therefore, for the spectral background characterization there is no need to fill the fiber with nitrogen. The dependency of spectral features to the incoupling using the experimental setup shown in Fig. 5.26 was investigated, with the photodetector directly coupled to the end of the 20 cm straight fiber. The lateral displacement of the VCSEL from the fiber center Δr is varied.$\Delta r = 0$ gives a ring structure as far-field and the resulting spectral feature has similar period but slightly higher standard deviation as in the case for sideways coupling ($\Delta r \neq 0$), in which a speckle pattern is observed (Fig. 5.27). The far-field of a bent fiber is always a speckle pattern independent of incoupling. Therefore, regarding to the fiber spectral background, precise incoupling is not an issue for gas sensing with hollow capillary fibers.

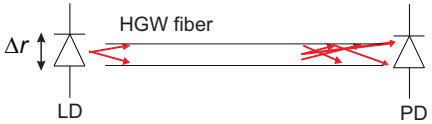

Fig. 5.26: Incoupling experiment with 20 cm straight fiber, where the lateral displacement between VCSEL and fiber center Δr is varied between 0 μm and 150 μm in 50 μm step.

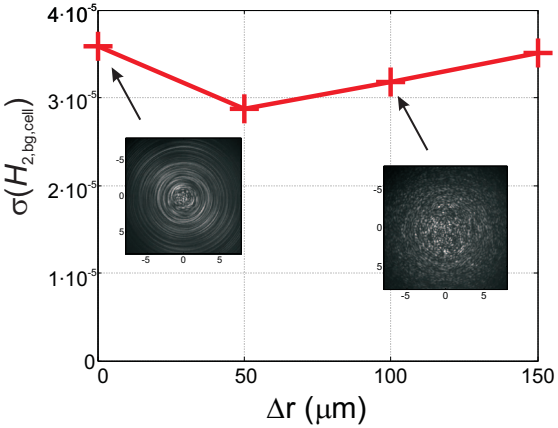

Fig. 5.27: $\sigma(H_{2,bg,cell})$ versus Δr (lateral laser displacement, see. Fig. 5.26). The insets show the fiber far-fields for $\Delta r = 0$ μm and 100 μm. This proves that the spectral background is essentially independent on the in-coupling.

Spectral background and outcoupling

To determine the influence of partial collection of the light coming from the fiber end on the fiber background, the distance between the fiber end and the photodiode Δz is varied between 1 mm and 12 cm (Fig. 5.28). The standard deviation of the

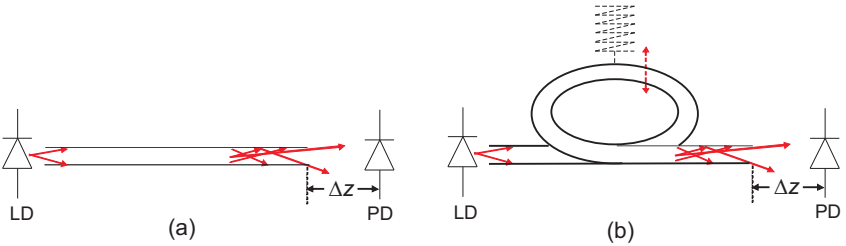

Fig. 5.28: Out-coupling experiment with (a) straight and (b) bent hollow fiber with and without vibration: the area of the integrated farfield by photodiode is varied by changing Δz. The resulting spectral background is shown in Fig. 5.29 and Fig. 5.30

spectral features against Δz is shown in Fig. 5.29. $\sigma(H_{2,bg,cell})$ increases linearly

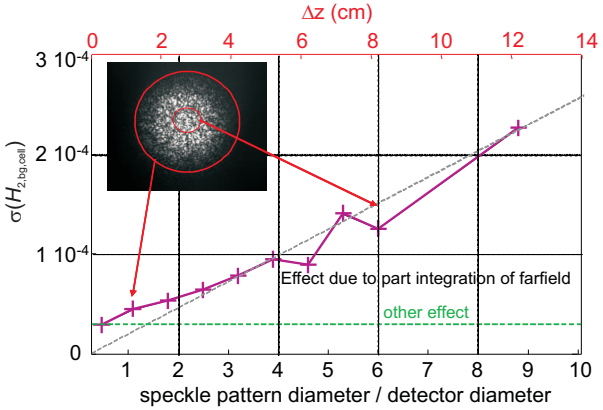

Fig. 5.29: The cell background $\sigma(H_{2,bg,cell})$ against the diameter ratio between detector and the integrated speckle pattern, which is varied by changing Δz (see Fig. 5.28(a)) At $\Delta z = 1$ cm the speckle pattern diameter is approximately equal to detector diameter and the background level goes to a threshold, indicating the anti-proportional dependency of $\sigma(H_{2,bg,cell})$ on the square root of the speckle number N. It is concluded that the residual spectral background is caused by mode-dependent losses.

with Δz, indicating its anti-proportional dependency on the diameter of the integrated farfield area, and thus the square root of N (the number of the integrated speckles), i.e. $\sigma(H_{2,bg,cell}) \propto 1/\sqrt{N}$. Below a certain distance, however, the decrease of the

fiber background level comes to a threshold, because N stays constant. Since the light emitted from the fiber end is all collected by the photodiode, this residual spectral background has to be caused by mode-dependent losses. These are constituted of the following:

- backscattering at the end of the fiber;
- incoupling losses: backscattering at the input of the fiber;
- responsivity of the photodiode. The responsivity of the photodiode is depending on the incident angle of the photons, which is mode-dependent.

The above effects are independent on fiber length and bent situation, whereas the following ones depend on these parameters:

- scattering in the fiber because of the inhomogeneity of the fiber or particles in the fiber;
- absorption in the coating (Ag/AgI), which increases when the fiber is bent.

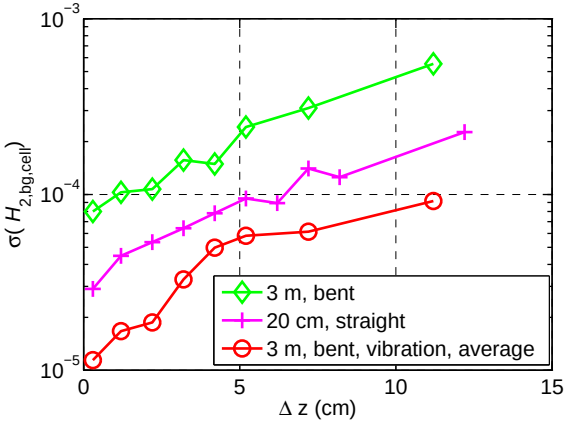

Fig. 5.30: The influence of integrated farfield on the fiber background for straight and bent fibers with and without vibration. The experimental setup is shown in Fig. 5.28(b).

To determine influences caused by the bending-specific loss mechanism, the previous experiment is repeated for the bent fiber (experimental setup Fig. 5.28(b)). Additionally, vibration is applied to reduce the influence of all possible mode-dependent effects on the fiber transmission. The results are shown in Fig. 5.30. The base value for 3 m bent fiber (curve marked with diamond) gives the upper limit of the mode-dependent effects. This value is lower for 20 cm straight fiber, because bending losses do not exist and lower scattering effects are inside the shorter fiber (curve marked with cross). Furthermore, there seems to be a constant improvement factor achievable by fiber vibration compared to non-vibrating system (roughly constant distance between

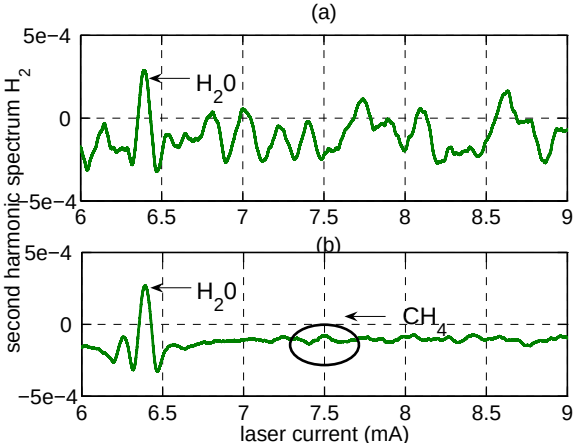

Fig. 5.31: (a) Second harmonic spectrum of the air-filled fiber at 2365 nm without vibration. The laser current tuning coefficient is approx. 1 nm/mA. (b) Second harmonic spectrum at 2365 nm with additional mechanical vibration. The methane absorption in the ambient air is clearly resolvable due to the nearly 10 fold decrease of fiber background by vibration.

the curve marked with circles and diamonds in logarithmic scale). By vibrating the fiber, the distribution of fiber modes is different in terms of amplitude and phase, so other speckle patterns are produced. By averaging different speckle patterns, the number of speckle points integrated by the photodiode is larger, which results in a smooth fiber transmission. It can be seen that by vibration the incoupling of light changes, which results in a spectral background same in amplitude but with a different shape. The averaging of these gives a smooth fiber transmission, similar to 'dithering' method in signal processing. As a result, a spectral background as low as 1×10^{-5} is achieved by vibrating the fiber and placing the photodiode very close to the fiber end. 1.5 ppm background level of methane absorption in the ambient air could be detected at 2.365 μm with 3 m hollow capillary fiber (Fig. 5.31).

Optimization of the vibration

In Fig. 5.32, several possibilities for applying vibration to the fiber are shown. Vibrating the laser diode requires more technical effort and laser diode could be destroyed by careless operation, so this possibility is excluded. Vibrating the photodiode laterally (3) or transversally (4) to fiber end does not produce significantly 'different' speckle patterns. The speckle pattern changes dramatically when the total fiber is vibrated (1) or vibrating the fiber at the incoupling position (2). For the latter case, independent speckle points are effectively generated and integrated by the photodiode with less influence on the remaining sensor parts compared to total vibration of the fiber.

It turned out practically, that the smoothing effect of vibration does not depend on the vibration frequency, as long as it is higher than the cutoff frequency of system filters, e.g., an analog low-pass filter and higher than the measurement rate. It will be

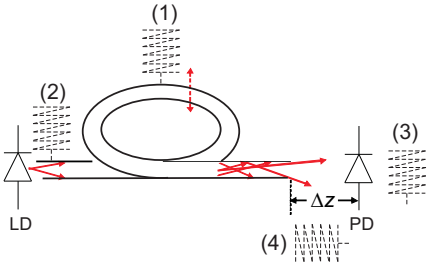

Fig. 5.32: The different possibilities applying vibration: 1) vibrating the whole fiber 2) vibrating the fiber at the in-coupling 3) vibrating the photodiode laterally 4) varying the distance between photodiode and fiber. The best performance was given by (1) or (2), as experimentally determined. Furthermore, (2) is technically easiest to realize.

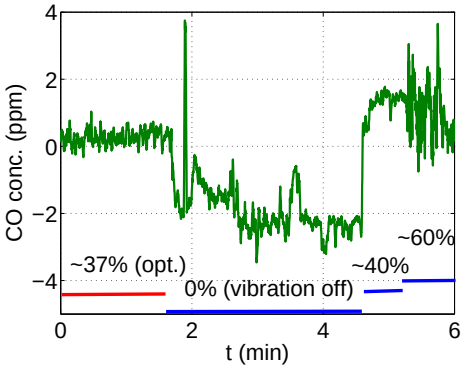

Fig. 5.33: Sensor baseline (output values without carbon monoxide) under different vibration conditions. With optimized vibration amplitude (37 %, in the order of 100 μm vibration) the sensor baseline has low noise and almost no offset due to low fiber spectral background. Other conditions give a strong and time dependent offset (0 % and 40 %), where the smoothing effect of vibration is too low, or high noise (60 %), where incoupled power varies strongly introducing new intensity fluctuations. The percentage values give the relative vibration strength.

shown in an example of carbon monoxide sensor (section 7.4), that 200 Hz is sufficient for 10 Hz concentration measurement rate and can probably be chosen even lower. The fiber background and sensor baseline is very sensitive to the vibration amplitude with its influence shown in Fig. 5.33. If the vibration amplitude is too high (e.g. in the range of the inner fiber diameter), the coupled light intensity is fluctuating as well, due to strongly variable coupling efficiency, and distorts the measurement. If the vibration amplitude is too low, the spectral background is not improved resulting in a unstable and inaccurate sensor baseline. The optimal value corresponds to several 100 μm.

Diffuse laser beam

Alternative methods instead of vibration to reduce the fiber spectral background is discussed here: one idea of this is to diffuse the laser beam so that the incoupling coefficients for different fiber modes are more or less equal. To realize it, a diffuse window sheet is put between the laser diode and fiber end. It turned out that the necessary fiber vibration amplitude is lower than without the diffuse window, but the fiber spectral background is not lowered further. It could be an indication that the fiber background is caused by effects inside the fiber or at the fiber output.

5.8 Comparison and conclusion

In this chapter, it was shown that the gas cell influences sensor sensitivity by the interaction length and cell background. The cells are compared below.

Single/multi-reflection cells For harsh conditions, for example in a gas or oil furnace, an optical cell is needed which is robust against thermal cycling and condensation. It turned out that a diffuse reflector-based cell has superior properties, namely easy alignment and robust behavior against thermal cycles and condensation in the combustion environment. Furthermore, such a reflector is less susceptible to the development of interference fringes, with the only trade off that the detector power is lower compared to a spherical mirror based cell. The intensity noise caused by the movement of waterdrops on the condensing surfaces is found to have a lowpass first order characteristic with the cutoff frequency of 5 Hz. Hence the utilized spectroscopic method is not susceptible to condensation noise. The limiting factor for the spectral background (peak to peak: 10^{-5}) is not the speckle noise given by diffuse reflections, but the surface reflection between laser and its window. On the other hand, single-reflective cells, despite their advantages, only offer a small optical path length, which is sometimes insufficient for sensitive gas sensing applications. Compact multipass cells (for example the White cell and the Herriott cell which have extent $<$ 10 cm $\times$ 10 cm) are investigated, which provide $\sim$ 10 times longer optical pathlength than the single reflective cell without enlarging the cell volume. It was determined that the White cell has a spectral background comparable to a single-reflective cell, so the advantage of longer optical pathlength can be fully exploited. The Herriott cell background is 10 times larger, attributable to the necessary laser light collimating lens placed before the light enters the cell. Generally, the multipass cell requires precise alignment which is likely to change in harsh environments, and which has extremely high sensitivity to dirt and condensation. Furthermore, the sample volume of multipass cells is still high (sub-liter range), which is unsuitable for applications like breath analysis.

	fiber		multipass cell		single-reflective cell	
	hollow fiber (vibration)[1]	PCF [2,3]	Herriott cell [3]	White cell	diffuse reflector[3]	spherical-mirror
Magnitude of $a_{res,cell}$ ('cell background')	10^{-5}	10^{-3}	10^{-4}	10^{-5}	10^{-5}	10^{-5}
optical pathlength l/ limitation [4]	up to 10 m/ attenuation	up to 0.4 m/ gas exchange	5 m/ compactness	1.56 m/ compactness	0.2 m/ compactness	0.2 m/ compactness
cell volume V	4 mL	3 μL	40 mL	100 mL	100 mL	100 mL
cell attenuation $1/T_{0,cell}$	24-30 dB	0.4-4 dB	3 dB	3 dB	17 dB	$\sim$ 0 dB
power decrease due to condensation	N/A[5]	N/A	N/A [5]	N/A [5]	Factor 5	Factor 50
alignment/ thermal stability	easy/ robust	difficult/ medium	difficult/ sensitive	difficult/ sensitive	easy/ very robust	medium/ medium
gas exchanging time ($\Delta p \leq 1$ bar)	$\sim$1 s	1 min	$<$1 s	$<$1 s	0 s (in-situ)	0 s (in-situ)
$\alpha_{res,cell}$ [6]	$1 \cdot 10^{-8}$ cm^{-1}	$2 \cdot 10^{-5}$ cm^{-1}	$2 \cdot 10^{-7}$ cm^{-1}	$6 \cdot 10^{-8}$ cm^{-1}	$5 \cdot 10^{-7}$ cm^{-1}	$5 \cdot 10^{-7}$ cm^{-1}
$\alpha_{res,cell} \times V = N_{res} \times \sigma_{gas}$ [7]	$4 \cdot 10^{-8}$ cm^2	$6 \cdot 10^{-8}$ cm^2	$8 \cdot 10^{-6}$ cm^2	$6 \cdot 10^{-6}$ cm^2	$5 \cdot 10^{-5}$ cm^2	$5 \cdot 10^{-5}$ cm^2

[1] all numbers including bending loss, attenuation for NIR range (situation improves in the MIR where the fiber is optimized for), incoupling loss between 0 dB and 6 dB, depending on FWHM of the light source.
[2] power fraction $\Phi = 20$ % for NIR sensing and incoupling efficiency 10 %.
[3] the limitation of $a_{res,cell}$ is specified in each section with hints for possible improvements.
[4] maximum gas exchanging time 1 min (with $\Delta p \leq 1$ bar), maximum dimensions 10 cm $\times$ 10 cm and maximum loss of light 30 dB.
[5] very high due to high number of distorted reflections. Cell is unsuited for very humid gas.
[6] smallest resolvable gas absorption coefficient by the cell. $\alpha_{res,cell} = a_{res,cell}/l$.
[7] 'cross section' of the cell. This is the minimum resolvable number of molecules N_{res} times the absorption cross section of the gas molecule σ_{gas}. For CO at 2.3 μm it is $\sigma_{gas} = 1.1 \times 10^{-20}$ cm^2 and thus $N_{res} = 4 \times 10^{12}$ for the hollow capillary fiber. For single/multipass cells, the minimum resolvable number of molecules is several orders of magnitudes higher.

Tab. 5.1: Comparison between investigated compact optical cells, i.e. cells with maximal dimensions of 10 cm $\times$ 10 cm. It is evident that the hollow fiber cell has superior properties. For very robust sensing the diffuse reflector based cell can be utilized.

Fiber-based cells TDLS-based gas sensors using gas permeable fibers as both gas 'pipe' and optical waveguide turned out to be very attractive, because fibers greatly extend the optical path length compared to conventional single-reflective gas cells. Compared to multi-pass cells, the sample volume is reduced by several orders of magnitude and the alignment is greatly simplified. A single-mode fiber such as the photonic crystal fiber would traditionally have been preferred for gas sensing since no spectral modal noise theoretically exists. However, the fiber background turns out to have a fluctuation in the order of 10^{-3}, which was found to be caused by a beating of the fundamental mode with additional weak core modes. The hollow capillary fiber is on the contrary highly multi-mode, but surprisingly exhibits a 10 times lower spectral background compared to the single-mode PCF. This is because the fringes with different FSR but similar amplitude cancel out with each other. The farfield of the HGW is a speckle pattern and it was found out that the spectral background is inversely-proportional to the number of speckle points integrated by the photodiode. Therefore, a setup with a large photodiode and with its distance to fiber end as short as possible, is insusceptible to a high spectral background. The effective integrated number of speckle points is even larger when mechanical vibration is applied to the fiber, resulting in a lower spectral background of 10^{-5}, which is comparable to a single-reflection cell. The gas exchanging time for HGW can be in 100 ms range due to the relatively large diameter of the fiber. A theoretical formula for the gas exchanging time (Eq. (5.15)) is also provided.

Cell comparison In Tab. 5.1 different optical cells are compared for aspects of physical properties. Even though small cell volume is desired, the cell volume is not the ultimate factor that is of interest to the physics of the situation. 'Cross section', or rather the resolvable absorption coefficient $\alpha_{res,cell}$ times cell volume V is more interesting. This divided by the absorption cross section of a gas molecule gives the minimum number of molecules that can be detected. In the literature, neither 'cross section' of an optical cell nor the minimum number of molecules that can be detected are investigated. Therefore, two quality factors are defined and compared: first, the resolvable absorption coefficient (unit: cm^{-1}), marking the sensitivity achievable with the optical cell, and second the 'cross section' of the cell (unit: cm^2), giving the minimum detectable number of gas molecules inside the cell when divided by the absorption cross-section of the gas molecule. In both aspects, HGW shows superior properties up to now. Compared to conventional single/multi reflection cells, the resolvable absorption coefficient by HGW is many orders of magnitude smaller, while the minimum resolvable number of molecules is also several orders of magnitude smaller than for other cells. For CO detection at 2.3 μm the minimum number of molecules detectable with a HGW based cell is in the order of 10^{12}, which corresponds to 40 pico-liter ($34\mu m \times 34\mu m \times 34\mu m$) gas volume. Therefore, we determine that a highly multi-mode waveguide HGW in combination with vibration is the best solution for sensitive gas sensing. Nevertheless, the suspended-core PCF may have some potential for improvement - the high spectral background may be lowered by improving the fiber design.

6 Signal processing: extraction of gas parameters

Signal processing is to extract the desired information e.g. gas concentration or gas pressure from the measured spectrum. Several requirements for sensors underline the need for an advanced signal processing: sensitive, fast (response time typically below 1 s), calibration-free and fail-save operation. Fail-save operation means the system and laser parameters are monitored continuously during operation, which is conventionally guaranteed by using a separate reference cell or reference etalon. Since a miniaturized and low-cost sensor is to be developed within the scope of this work, no separate reference etalon can be afforded. Instead, efficient signal processing methods have to enable a low-complex and fail-save sensor concept. For this, VCSEL-based gas sensing offers two advantageous aspects: less effect of the laser amplitude modulation on the second-harmonic spectrum and a large current tuning range. The first aspect simplifies the signal model for the measured WMS signal, while the second aspect offers a solution for inherent monitoring of laser parameters. A schematic overview of the sensor system

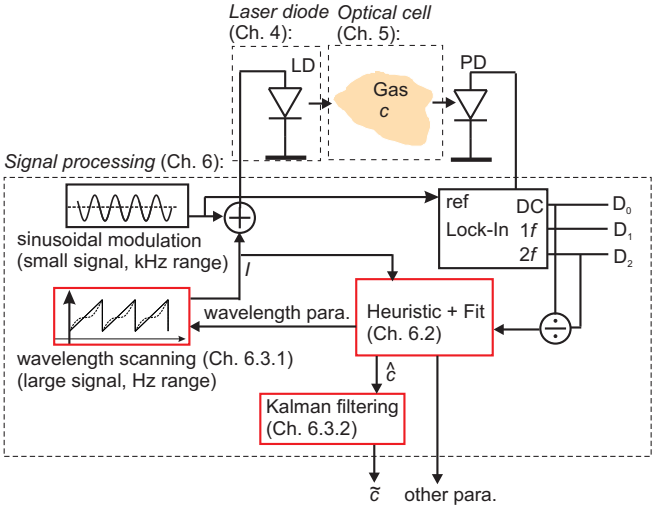

Fig. 6.1: Schematic overview of the sensor system. This chapter is describing the signal processing with the focus on the three components marked in red.

is given in Fig. 6.1. This chapter deals mainly with the following questions:

How to extract the gas parameters from the measured spectrum and what is the signal model for it (section 6.2)? For a moderate cost sensor, evaluation algorithm with low-complexity are required because of the small computing capacity given by the existing micro-controllers (e.g. processor Hitachi H8, clock frequency: 24 MHz, no floating point support). However, there is usually a trade-off between the simpleness

and reliability of the sensor. The simplest variant of signal processing is detection of the peak absorbance [97]. However, this method is only accurate if the spectral baseline is known a priori or measured permanently with a separate reference cell, which adds complexity to the sensor design. The second variant of signal processing is to use a measured reference curve for fitting of the measured spectrum using linear curve fit. The reference spectra can be measured once, in which case no separate reference cell is necessary [98], or on-line with a separate reference cell containing a precisely known gas concentration [99, 100]. In the first case, reference spectra at all occurring gas pressures and temperatures have to be stored. In the latter case, the gas pressure and temperature of the measured gas and the gas in the reference cell have to be regulated to be exactly the same, which also adds enormous sensor complexity [5]. Curve fit with an analytical model function is much more flexible and possibly more exact compared to using a measured reference curve, which also contains noise. An analytical model for recorded WMS harmonic signals was recently developed by Kluczynski [15], which includes the effect of laser residual amplitude modulation (RAM) in the measured spectra. This effect is especially strong for DFB lasers. The signal model for a second harmonic spectrum measured with a VCSEL is much simpler than in the case of a DFB laser, because a VCSEL has a lower amplitude modulation at the same frequency modulation.

How to monitor the laser parameters e.g. wavelength with as low as possible sensor complexity, so that calibration-free operation is obtained (section 6.2.2)? Laser wavelength is an important parameter because the absorption strongly depends on wavelength. For trace gas detection, the necessary laser current to match the laser emission wavelength to the gas absorption line is unknown. For non-trace gas detection, the laser wavelength can be identified from the absorption features in the measured spectrum. For the wavelength stabilization, a common method is to apply line-locking by

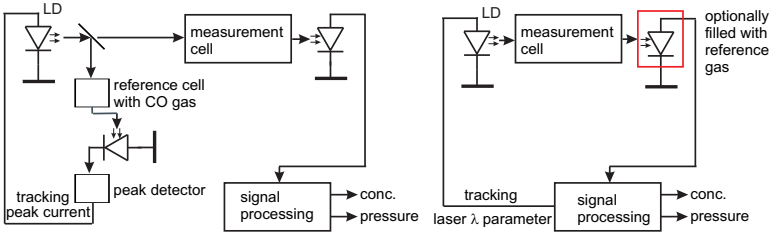

(a) line locking, target gas = reference gas: a separate reference path is used for the determination of the laser current to scan the gas absorption lines of interest.

(b) line identification, target gas ≠ reference gas: laser parameters are extracted from the measured spectrum.

Fig. 6.2: Schematic plot of line locking and the line identification concept introduced in this dissertation.

using a separate reference path and peak detection (Fig. 6.2(a)). The laser current to match the peak of absorption line is determined by this [100, 5]. But with this method the absolute wavelength variation and the laser tuning coefficient remain unknown. In cases when this is problematic, reference etalons are used [12, 101, 102]. However, etalons alone do not allow for determination of the absolute wavelength (parameter

λ_0), only the wavelength shift during a spectral scan can be determined. Furthermore, the reference etalon method and - for trace gas applications - the line locking method require the use of a separate reference cell, beam splitters and a second photodetector. When a cuvette with the target gas or an etalon is placed in the main absorption path, reliable and calibration-free gas detection is no longer possible.

The disadvantages of line-locking and reference etalon can be overcome, when a cuvette with a second absorbing gas is placed in the main absorption path and several absorption lines of the second gas serve as wavelength markers (Fig. 6.2(b)). This allows for determination of the absolute wavelength scale, including wavelength offset λ_0, linear and nonlinear tuning coefficients of the laser k and k_2. Since the reference gas is not the target gas, limited outdiffusion during the lifetime of the reference gas does not affect the sensor baseline of the target gas. Due to their wide current tunablity, vertical-cavity surface-emitting lasers are predestined for this application. The photodetector housing can be used as a reference gas cell (section 7.3.3). The comparison between this technique and conventional technique is given in Tab. 6.1.

Wavelength stabilization principle	Need separate optics?	Absolute wavelength offset?	Absolute wavelength variation
Line locking	yes (reference cell)	yes, known from absorption line	No, spectral width unknown
Reference etalon	yes (etalon)	no	yes, known from etalon thickness
This work: inline reference cell	no (reference cell integrated in main cell)	yes, known from absorption line	yes, because several lines used

Tab. 6.1: Summary of possible methods for wavelength stabilization or determination.

What is the theoretically lowest possible sensor noise (section 6.3)? The sensor noise is given by the sensor system including laser diode, photodiode and the resulted signal fluctuation that passes through the signal processing. This noise is inherent to system components and caused by basic physical principles like the discrete electron charge or thermal agitation. The generated noise is filtered by the curve-fit or other filters. The effect of the curve-fit depends on the shape of the data, i.e. also the procedure how data is recorded. In this chapter, the following two aspects are to be examined in terms of optimal measurement procedure and signal processing:

- Sample 'which' wavelength point 'how often'. Target is the optimal data recording way so that the linear least square curve fitting gives the lowest noise in terms of signal to noise ratio. At a given sensor bandwidth linear least squares curve fitting is the best linear method to filter the measurement noise. It gives the smallest variance on the fitted concentration values among all linear digital filtering methods, e.g. lowpass/highpass or Wiener filtering [103, 104]. However, the performance of curve fitting depends on the signal model for the measured data, which in turn depends on the spectra data that are recorded. Hence, the sensor performance can be improved, if the spectrum is recorded/'observed' in an optimal way. A special case of nonlinear scanning is applied in [105]. The wavelength scanning jumps over the spectral range where no absorption line is present and therefore optimizes scanning of two separate absorption lines. In this

chapter this approach is generalized and the optimum scanning method and corresponding signal to noise ratio (SNR) improvement is determined (section 6.3).

- What is the gain of applying time-variant/adaptive filter e.g. Kalman filtering for laser spectroscopic application and how to adjust the filter bandwidth over time properly? Conventionally, a time-invariant filter is used for filtering of residual noise on the concentration values e.g. lowpass/highpass or Wiener filtering [103, 104]. However, these filters result in a high time constant if a concentration fluctuation occurs. Time-variant filters like Kalman filtering theoretically overcome this disadvantage. For this the noise variances of all signals have to be exactly known over time, which constitutes the practical difficulty of this method. For laser spectroscopy application, Kalman filtering was applied in the literature [106, 107, 108], but the noise variance determination was based on very unrealistic assumptions. This is a significant limitation, because the filtering is then either too low or too high depending on the situation. In this work, a method is developed to estimate the signal variances over time properly.

6.1 Signal model and curve fit

The signal model gives an approximate mathematical description of the signal to be analyzed. It consists of the model function for deterministic signal components and indeterministic components like noise. The signal model has unknown parameters, some of which are of interest and the noise is described with certain statistical properties. A signal model is required for a curve fit, which is used to extract unknown parameters from a measured signal. The signal to be analyzed consists of N samples y_i. A typical signal model looks like

$$y_i = f(x_i, \mathbf{u}) + \epsilon_i \qquad i = 1, \ldots, N \tag{6.1}$$

with $f(x, \mathbf{u})$ being the model function, ϵ_i random variables modeling noise, $\mathbf{u}$ the vector of unknown parameters and x_i the independent and known variable, which is swept during the measurement. The model function distinguishes between linear and nonlinear model function. This distinction is important because the methods to solve these models are significantly different.

6.1.1 Linear and nonlinear model function

A linear model function f takes the form [109]:

$$f(x, \mathbf{u}) = u_1\, \psi_1(x) + u_2\, \psi_2(x) + ... + u_M\, \psi_M(x), \tag{6.2}$$

x is the independent variable, and $\mathbf{u} = [u_1, ..., u_M]$ is the unknown parameter vector. $\psi_1(x)$, ...,$\psi_M(x)$ are component functions, which can be polynomials, sinusoidal, logarithms, spectral components, etc... M is defined as the number of parameters in parameter vector. In our model, the variable x is laser current I, but generally can be also laser temperature. Data of N samples is available. λ is not chosen as x variable, because the relationship between laser current and emitting wavelength is not exactly known. The relationship should be considered in the model. $\mathbf{u}$ contains gas concentration, pressure, wavelength offset, etc... . For example:

$$f(x, \mathbf{u}) = u_1\, x + u_2 x^2 + ... + u_M\, \log x, \tag{6.3}$$

is a linear model with $\psi_1(x) = x$, $\psi_2(x) = x^2$ and $\psi_M(x) = \log x$. In contrary,

$$f(x, \mathbf{u}) = u_1\, x + u_2 e^{x\, u_3} \tag{6.4}$$

is a nonlinear model because its relationship to parameter u_3 is nonlinear. The task of a least squares curve fit is to find the parameter solutions $\widehat{\mathbf{u}}$, defined by:

$$\widehat{\mathbf{u}} = \widehat{\mathbf{u}}(\mathbf{y}) = \underset{\mathbf{u}}{\operatorname{argmin}} ||\mathbf{y} - f(x, \mathbf{u})||^2. \tag{6.5}$$

The ansatz is equivalent to $\sigma(\widehat{\mathbf{u}}) \rightarrow \min$ for a linear model [110]. A linear model for measurement data $\mathbf{y}$ can be written as:

$$\mathbf{y} = \mathbf{\Psi}\, \mathbf{u} + \epsilon, \tag{6.6}$$

with $\mathbf{\Psi}$ being the observation matrix:

$$\mathbf{\Psi} = \begin{pmatrix} \psi_1(x_1) & \cdots & \psi_M(x_1) \\ \vdots & & \vdots \\ \psi_1(x_N) & \cdots & \psi_M(x_N) \end{pmatrix} \tag{6.7}$$

The optimum solution for the parameter vector $\widehat{\mathbf{u}}$ is given by [111]:

$$\widehat{\mathbf{u}} = (\mathbf{\Psi}^T \mathbf{\Psi})^{-1} \mathbf{\Psi}^T \mathbf{y} \tag{6.8}$$

Furthermore, the noise variance of the estimated parameter is derived from Eq. (6.8) as [111]:

$$\operatorname{cov}(\hat{\mathbf{u}}) = (\mathbf{\Psi}^T \mathbf{\Psi})^{-1} \operatorname{cov}(\mathbf{y}) \tag{6.9}$$

with the variance of the i-th estimated parameter u_i given by:

$$\sigma^2(\widehat{u}_i) = \operatorname{cov}(\hat{\mathbf{u}})_{ii} \tag{6.10}$$

σ^2 stands for variance and σ stands for standard deviation. $\operatorname{cov}(\hat{\mathbf{u}})$ is the covariance matrix of the vector $\mathbf{u}$.

In case of a nonlinear model, closed form expression exist neither for $\widehat{\mathbf{u}}$ like Eq. (6.8), nor for the noise variance on the estimated parameters like Eq. (6.9). However, the nonlinear model can be linearized at good approximate values of the solution parameters. If the vector $\overline{\mathbf{u}}$ symbolizes a set of good approximate values, then

$$\begin{pmatrix} y_1 - f(x_1, \overline{\mathbf{u}}) \\ y_2 - f(x_2, \overline{\mathbf{u}}) \\ \vdots \\ y_N - f(x_N, \overline{\mathbf{u}}) \end{pmatrix} = \underbrace{\begin{pmatrix} \frac{\partial f(x_1, \overline{\mathbf{u}})}{\partial u_1} & \cdots & \frac{\partial f(x_1, \overline{\mathbf{u}})}{\partial u_M} \\ \vdots & & \vdots \\ \frac{\partial f(x_N, \overline{\mathbf{u}})}{\partial u_1} & \cdots & \frac{\partial f(x_N, \overline{\mathbf{u}})}{\partial u_M} \end{pmatrix}}_{\text{Jacobian}} \begin{pmatrix} u_1 - \overline{u}_1 \\ u_2 - \overline{u}_2 \\ \vdots \\ u_M - \overline{u}_M \end{pmatrix} \tag{6.11}$$

is a linear equation in u_1, ..., u_M, that is to be solved in a least squares sense. The Jacobian matrix is the derivative of the model function $f(x, \mathbf{u})$, with respect to $\mathbf{u}$. The linearization will be only useful if good approximate values for the parameters i.e. $\overline{\mathbf{u}}$ exist. This is at least the case for the nonlinear parameters i.e. the parameters the Jacobian matrix depends on.

If linearization can not be carried out, traditional nonlinear curvefit methods like the Gauss - Newton or Marquardt - Levenberg method for local minimum search [112] or statistical methods like genetic algorithm [113] for global minimum search, have to

be applied. These methods operate iteratively and provide a numerical solution to the problem of minimizing the error function Eq. (6.5). The solution of nonlinear curve fit for local minimum i.e. Marquardt Levenberg algorithm may not converge or converge to a local minimum if the initial values are too far away from the solution. For the type of problem here, the computing complexity with statistic algorithms is typically higher than for local minimum search methods. According to the investigations in this work, using genetic algorithm, 20 population, 5 generation are needed for fitting data to a single line model (see section 6.2) with the same precision as local minimum search. It corresponds to $100N$ times evaluation of model function, which is unsuitable for microcontroller programming. For comparison, local minimum search with numerical approximation of Jacobian matrix corresponds to 24 N evaluations of model function and with analytical calculation of the Jacobian matrix corresponds to 4 N evaluations of model function (assuming 4 iterations). With a linear curve fit, only N evaluations are needed.

Therefore, it is advantageous to find a method to eliminate the nonlinear parameters: if these are estimated separately with heuristic methods, a linear curve fit can be utilized for a nonlinear model. In this case, the set of good approximate values can be used to linearize the nonlinear model or can be used as initial values for nonlinear curve fit, which then needs less iterations and has improved convergence. Alternatively, the linear curve fit is applied directly and the nonlinear parameters are replaced by the good approximate value. Thus heuristic methods with subsequent curve fit may achieve the same exactness like a standard curve fit, but with less iteration or no iteration at all, and it is more likely to find the global minimum. These methods are introduced in section 6.2. A comparison between linear and nonlinear curvefit is given in Tab. 6.2.

	linear least squares (LLS)	**nonlinear least square**
Implementation	scalar product	iterative numerical minimization
Convergence of algorithm	yes	uncertain
Computing speed	fast	low
Closed expression for solution	yes (Eq. (6.8))	no
Closed expression for noise variance	yes (Eq. (6.9))	no

Tab. 6.2: Summary of the main difference between the linear and nonlinear curve fitting.

6.1.2 Signal model for wavelength modulation spectroscopy based system

In this work, no measured reference spectra are used for curve fitting, but an analytical signal model. This is easier adapted to other gases by simply replacing the spectral data available from databases like HITRAN. In addition to this flexibility, pressure and temperature influences are also easily modeled. The signal model for wavelength modulation spectroscopy utilizing VCSEL is developed here. It is an analytical expression considering the influence of laser nonlinear P-I-characteristic, using a theory developed by Hangauer [114]. The models for gas and laser behavior are given at first and then combined for the WMS measured signal. These are schematically displayed

in Fig. 6.3, Fig. 6.4 and Fig. 6.5, respectively. The noise on the WMS signal is modeled as well.

Laser behavior

In WMS the current of the laser diode I_L is sinusoidally modulated around a bias current I with a modulation frequency f_m and a current modulation amplitude I_a.

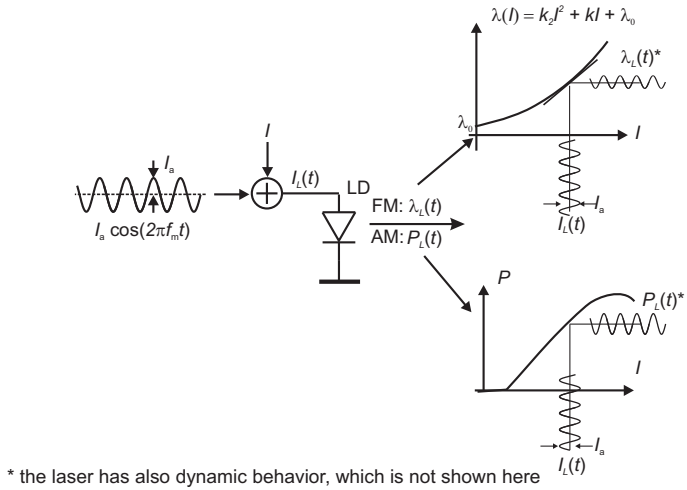

Fig. 6.3: Laser behavior: the sinusoidally modulated injection current $I_L(t)$ causes laser amplitude modulation (AM) $P_L(t)$ and frequency modulation (FM) $\lambda_L(t)$.

$$I_L(t) = I + I_a \cos(2\pi f_m t) \tag{6.12}$$

The current causes a wavelength variation of $\lambda_L(t)$:

$$\lambda_L(t) = \lambda + \lambda_a \cos(2\pi f_m t + \phi), \tag{6.13}$$

where $\lambda_a = \lambda_a(I, f_m)$ is the modulation amplitude in wavelength and $\phi = \phi(f_m)$ the phase shift between wavelength and current variation. It was shown in [49] that the current-to-wavelength tuning behavior of VCSELs can be described with a second order polynomial. This is because the internal laser temperature, which is linear to emitted wavelength, increases quadratically with the laser current.

$$\lambda(I) = k_2\, I^2 + k\, I + \lambda_0 \tag{6.14}$$

k_2 is the nonlinear coefficient, k is the linear coefficient for laser tuning behavior, λ_0 is the wavelength offset. For small current variations around a bias point, the differential current to wavelength tuning behavior is linear (see section 4.2.2):

$$\lambda_a = I_a \frac{d\lambda}{dI} H(f_m) = I_a\,(2\,k_2\,I + k)\; H(f_m) \tag{6.15}$$

$H(f_m)$ is the FM response and has a low pass behavior, with the 3 dB cutoff fre-

quency in the range of 10 to 100 kHz for VCSELs (section 4.2) [46, 41, 42]. λ_a increases with bias current I because k_2 is usually positive, and drops with increasing tuning frequency f_m. The laser amplitude modulation $P_L(t)$ is modeled as following:

$$P_L(t) = P_0 + |P_1| \cos(2\pi\, f_m\, t + \angle P_1) + |P_2| \cos(4\pi\, f_m\, t + \angle P_2) + \ldots \tag{6.16}$$

with the complex harmonic coefficients P_n. The nonlinearity of the laser P-I-characteristic causes the nonzero higher harmonics P_2, P_3, ..., which are responsible for the laser induced offset and slope on the measured harmonic spectra.

Gas behavior

The gas transmission $T_{gas} = T_{gas}(\lambda, c, p, T)$ is described by Beer-Lambert law Eq. (3.8) as shown in section 3.1.2. c, p, T are the gas concentration, pressure and temperature,

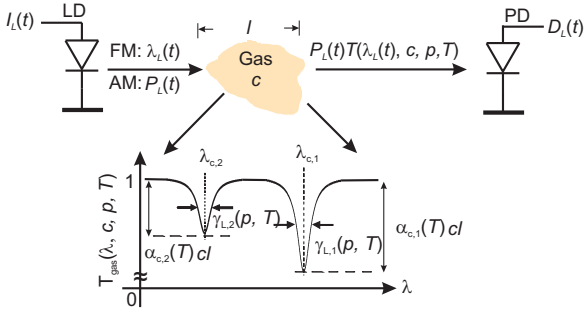

Fig. 6.4: Gas behavior: the Lorentzian shaped gas absorptions are described with line width γ_L, peak line absorbance $\alpha_c\, c\, l$ and line center wavelength λ_c

respectively. At ambient pressure and temperature, the absorption line is Lorentzian-shaped as shown in section 3.1.3. For unsaturated Lorentzian shaped lines, gas transmission T_{gas} can be written as:

$$T_{\text{gas}}(\lambda, c, p, T) = 1 - \sum_j \frac{\alpha_{c,j}(T)\, c\, l}{1 + \left(\frac{\lambda - \lambda_{c,j}}{\gamma_{L,j}(p,T)}\right)^2} \tag{6.17}$$

with l is the interaction length between gas and light, $\alpha_{c,j}$ the peak absorption coefficient (unit: (ppm m)$^{-1}$) Eq. (3.11), $\lambda_{c,j}$ the absorption line center (unit: μm) and $\gamma_{L,j}$ the HWHM of the j-th absorption line (Fig. 6.4). The latter is temperature and pressure dependent (see Eq. (3.20)), i.e.

$$\gamma_L(p, T) = p\, \gamma_{air} \left(\frac{T}{296K}\right)^{\zeta} \tag{6.18}$$

The remaining coefficients γ_{air}, ζ_j, $\lambda_{c,j}$ and $S_j(296K)$, $E_{L,j}$, $Q(T)$ for the peak absorption coefficient are taken from HITRAN [10]. According to Eq. (3.20) and Eq. (3.23), we have:

$$\frac{\gamma_L(T)}{\gamma_L(296K)} = \left(\frac{T}{296K}\right)^{\zeta}, \tag{6.19}$$

with absorption line dependent ζ in the range of 0.5...1, and

$$\frac{\alpha_c(T)}{\alpha_c(296K)} = \frac{296K}{T}\,\frac{Q(296K)}{Q(T)}\,\frac{\exp\left(-\frac{E_L}{k_B\,T}\right)}{\exp\left(-\frac{E_L}{k_B\,296K}\right)}\,\left(\frac{296K}{T}\right)^{\zeta}. \tag{6.20}$$

$Q(T)$ is the total internal partition sum [10], E_L is the lower state energy of the transition corresponding to the absorption line. Both are gas molecule parameters. k_B is the Boltzmann constant.

WMS signal

The intensity arriving at the photodetector creates the photodetector current $D_L(t)$ (unit: A), which is given as the product of gas transmission signal $T(\lambda_L(t), c, p, T)$, the laser intensity modulation signal $P_L(t)$ and the responsivity r of the detector (unit: W/A) (Fig. 6.5). Since the tuning range of the lasers is very narrowband compared to the sensitivity range of the detector, the responsivity is assumed to be wavelength independent.

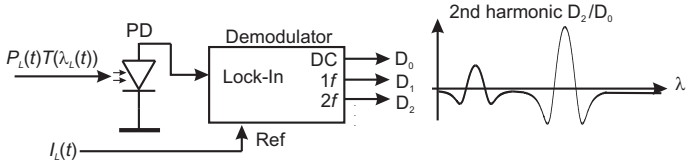

Fig. 6.5: Model for the demodulation with a Lock-in amplifier used in WMS.

$$D_L(t) = \frac{1}{r} T(\lambda_L(t), c, p, T)\, P_L(t) \tag{6.21}$$

The total transmission $T(\lambda, c, p, T)$ is given by gas transmission $T_{\text{gas}}(\lambda, c, p, T)$ superimposed with cell background $A_{bg,cell}(\lambda)$ and attenuated with cell transmission $T_{0,cell}$ (Eq. (5.2)).

The detector signal is not sinusoidal because the gas transmission is nonlinear and has many harmonic components. These harmonic components $D_n(I, \mathbf{u})$ are determined via Lock-In amplifier/Fourier analysis.

$$D_n(I, \mathbf{u}) = \frac{\epsilon_n}{2\pi} \int_{-\pi}^{\pi} D_L\left(\theta/2\pi f_m\right) e^{-jn\theta} d\theta \tag{6.22}$$

$$= \frac{\epsilon_n}{2\pi}\,\frac{1}{r} \int_{-\pi}^{\pi} T(\lambda_L\left(\theta/2\pi f_m\right), c, p, T) P_L\left(\theta/2\pi f_m\right) e^{-jn\theta} d\theta \tag{6.23}$$

with $\theta = 2\pi f_m t$. ϵ_n equals to one for $n = 0$ and equals to two for $n > 0$. The Fourier coefficients of the gas transmission $T_{\text{gas}}(\lambda_L(t), c, p, T)$ and laser power intensity function $P_L(t)$ are denoted as harmonic spectra $H_{n,gas}$ and P_n:

$$P_n(I) = \frac{\epsilon_n}{2\pi} \int_{-\pi}^{\pi} P_L\left(\theta/2\pi f_m\right) e^{-j\,n\,\theta} d\theta \tag{6.24}$$

$$H_{n,gas}(I, \mathbf{u}) = \frac{\epsilon_n}{2\pi} \int_{-\pi}^{\pi} T_{\text{gas}}\left(\lambda_L\left(\theta/2\pi f_m\right), c, p, T\right) e^{-j\,n\,\theta} d\theta \tag{6.25}$$

According to Hangauer [114] and Kluczynski [52], the normalized harmonic signal D_n (Fourier coefficient of photodetector current $D_L(t)$) is approximately composed of the influence of gas transmission H_n and influence of laser P_n. H_n contains the wanted information. P_n and $T_{0,cell}$ give unwanted influence and are removed by normalization with detector DC signal D_0 in this work:

$$\frac{D_n(I,\mathbf{u})}{D_0(I,\mathbf{u})} \approx \frac{H_{n,gas}(I,\mathbf{u})}{H_{0,gas}(I,\mathbf{u})} + \frac{P_n(I)}{P_0(I)} \tag{6.26}$$

Here the additive optical cell background $A_{bg,cell}(\lambda)$ is neglected. As described in Chap. 5, it has a random structure, but is rather time-invariant compared to white noise. Due to the complicated and random structure no deterministic model for the cell background can be given. Therefore, the cell background is required to be very small, i.e. 10^{-5} in absorbance, so that the usual sensor resolution can be obtained. However, it could be modeled with a polynomial, if the interference has a large frequency spectral range, or, alternatively, by white noise if vibration is applied to the cell, which makes the spectral background random with respect to time, i.e., 'noise like'. Furthermore, for small absorbance $H_{0,gas}$ is approximately 1.

Empirically it was found that P_n/P_0 can be approximated by superposition of polynomials, i.e. offset, slope, ...:

$$\frac{P_n(I)}{P_0(I)} = \sum_{k=0}^{n_{\mathrm{PI}}-n} b_k\, I^k \tag{6.27}$$

n_{PI} is the order of the polynomial of the laser P-I-characteristic. It is found out in our experiments that $n_{\mathrm{PI}} = 3$ is sufficient for the sensors realized in this work. The higher harmonic signals (i.e. D_n with $n > 3$) have therefore no influence from the laser amplitude modulation and D_n/D_0 directly represents the harmonic gas spectrum $H_{n,gas}$.

For unsaturated Lorentzian profile, $H_{n,gas}$ has a closed analytical expression based on Arndt's formula $S_n(x,m)$ as given in Eq. (3.2.2) in section 3.2.2. The appropriate normalized wavelength x and modulation amplitude m for a single line read

$$x = \frac{\lambda - \lambda_c}{\gamma_L(p,T)} = \frac{k_2 \cdot I^2 + k \cdot I + \lambda_0 - \lambda_c}{p\,\gamma_{air}(T/296K)^{\zeta}} \tag{6.28}$$

$$m = \frac{\lambda_a}{\gamma_L(p,T)} = \frac{I_a\,(2\,k_2\,I + k)\;H(f_m)}{p\,\gamma_{air}(T/296K)^{\zeta}} \tag{6.29}$$

Using harmonic detection with $n > 0$, the signal model for measurement data $\mathbf{y}$ is therefore:

$$\boxed{f(I,\mathbf{u}) = \frac{D_n(I,\mathbf{u})}{D_0(I,\mathbf{u})} = c\,l \sum_j \alpha_{c,j}(T)\; S_n(x_j,m_j) + \sum_{k=0}^{n_{\mathrm{PI}-n}} b_k I^k} \tag{6.30}$$

with x_j and m_j being the normalized wavelength and normalized modulation am-

plitude for jth line (see Eq. (6.14) and Eq. (6.18)):

$$\boxed{\begin{aligned} x_j &= \frac{k_2\, I^2 + k\, I + \lambda_0 - \lambda_{c,j}}{p\, \gamma_{air,j}\, (T/296K)^{\zeta_j}} \\ m_j &= \frac{I_a\, (2\, k_2\, I + k) H(f_m)}{p\, \gamma_{air,j}\, (T/296K)^{\zeta_j}} \end{aligned}} \tag{6.31}$$

For second harmonic detection, i.e. $n = 2$, the parameter vector is $\mathbf{u} = [c, p, T, k_2, k, \lambda_0, H(f_m), b_0, b_1]$. b_0 and b_1 are linear parameters of the model and the rest are nonlinear parameters. Here only one gas is considered, whereas the number of gas absorption lines is unlimited. j is the index of the absorption line being considered in the spectrum.

In summary, we have an closed analytical model for WMS second-harmonic signal including the residual amplitude modulation influence from the laser. The latter simply modeled as slope and offset on the second harmonic spectrum.

Noise model

The signal model for the measured data vector $\mathbf{y}$ is given as the sum of model function $f(I, \mathbf{u})$ with noise vector ϵ:

$$y_i = f(I_i, \mathbf{u}) + \epsilon_i \qquad i = 1, \ldots, N \tag{6.32}$$

$$\mathrm{cov}(\epsilon) = \mathrm{cov}(\mathbf{y}) = R\, N\, S_{yy} \mathbf{I} \qquad E(\epsilon) = \mathbf{0}, \tag{6.33}$$

$\mathbf{I}$ is the identity matrix and E stands for expectation value. ϵ is a vector of uncorrelated white noise [110]. This is because thermal noise and shot noise are white noise, and the 1/f noise component of the pre-amplifier and laser noise is suppressed by the modulation spectroscopy. $\mathrm{cov}(\mathbf{y})$ can be expressed by the product of noise power density S_{yy} on measured data $\mathbf{y}$ and the noise bandwidth $R\,N$. N is the number of sampling points per spectrum (unit: 1) and R is the concentration or spectrum measurement rate. S_{yy} (unit: 1/Hz) is a function of detector DC current D_0 [115] (see Fig. 6.6):

$$S_{yy}(D_0) = \mathrm{RIN} + \underbrace{\frac{2\,(D_0 + I_{\mathrm{dark}})\, e}{D_0^2}}_{\text{PD shot noise}} + \underbrace{\frac{4\, k_B\, T_{PA}}{R_v\, D_0^2}}_{\text{thermal noise}} \tag{6.34}$$

RIN is the laser relative intensity noise (typically $10^{-12}, \ldots, 10^{-14}$ Hz^{-1}); I_{dark} is the dark current of the photodetector; R_v is the transimpedance gain of the pre-amplifier; k_B is Boltzmann constant and T_{PA} is the temperature of the pre-amplifier. An example is given in Fig. 6.6, where the noise components and the total noise are plotted in a doubly logarithmic scale. It is evident, that in this typical case well above 3 μA photocurrent, the laser noise is dominating and the noise level S_{yy} stays constant.

6.1.3 Linear form of the signal model and its closed form solution

The signal model Eq. (6.30) can be considered as a linear model if nonlinear parameters e.g. λ_0, k, k_2 and $H(f_m)$ are known. This is important because the linear curve-fit has significant advantages over the nonlinear curve-fit as summarized in Tab. 6.2 in section 6.1.1. In this case, the measurement vector $\mathbf{y}$ is expressed with the following

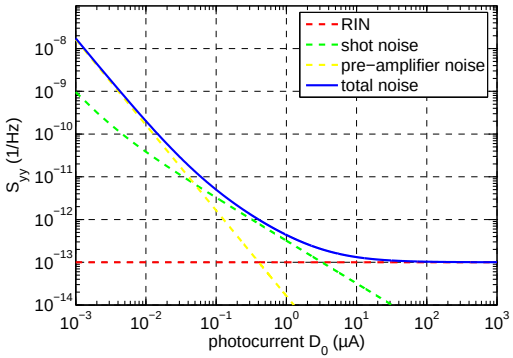

Fig. 6.6: The simulated dependence of laser noise, shot noise and thermal noise as well as the total noise on DC photodetector current D_0 given by Eq. (6.34). Typical values of RIN $= 10^{-13}$ Hz^{-1}, $I_{\mathrm{dark}} = 2$ nA (for NIR), $R_v = 10^6$ V/A and $T_{PA} = 296$ K are assumed. The laser noise is dominating and noise level stays constant for a DC current $D_0 \gg 3$ μA.

model:

$$\underbrace{\begin{pmatrix} y_1 \\ y_2 \\ \vdots \\ y_N \end{pmatrix}}_{\mathbf{y}} = \underbrace{\begin{pmatrix} \psi_1(I_1) & 1 & I_1 \\ \psi_1(I_2) & 1 & I_2 \\ \vdots & \vdots & \vdots \\ \psi_1(I_N) & 1 & I_N \end{pmatrix}}_{\mathbf{\Psi}} \cdot \underbrace{\begin{pmatrix} c \cdot \alpha_c \cdot l \\ b_0 \\ b_1 \end{pmatrix}}_{\mathbf{u}} + \underbrace{\begin{pmatrix} \epsilon_1 \\ \vdots \\ \epsilon_N \end{pmatrix}}_{\epsilon} \tag{6.35}$$

$\mathbf{\Psi}$ is the observation matrix with each column representing the components ψ_i forming the measured spectrum:

$$\psi_1(I_i) = \frac{1}{\alpha_c} \sum_j \alpha_{c,j}(T)\, S_n(x_j, m_j) \tag{6.36}$$

$$\psi_2(I_i) = 1 \tag{6.37}$$

$$\psi_3(I_i) = I_i \tag{6.38}$$

α_c is defined as the peak absorption coefficient in the measured spectrum and b_0 and b_1 are the slope and offset in the background given by laser AM (Eq. (6.30)). $S_n(x_j, m_j)$ is the Arndt formula with $x_j = x_j(I_i, p, T)$ and $m_j = m_j(I_i, p, T)$ being the normalized wavelength and normalized modulation amplitude for the j-th absorption line given in Eq. (6.28) and Eq. (6.29).

The first parameter is $u_1 = c\,\alpha_c\,l$, so $\widehat{c}$ has the closed solution according to Eq. (6.8):

$$\boxed{\widehat{c} = \frac{1}{\alpha_c\, l} \left((\mathbf{\Psi}^T \mathbf{\Psi})^{-1} \mathbf{\Psi}^T \right)_1 \mathbf{y}} \tag{6.39}$$

which is simply a scalarproduct. While $\left((\mathbf{\Psi}^T \mathbf{\Psi})^{-1} \mathbf{\Psi}^T \right)_1$ denotes the first row of $(\mathbf{\Psi}^T \mathbf{\Psi})^{-1} \mathbf{\Psi}^T$. The scalar product is simple and efficient, only products and sums are

to be calculated. This is suitable for programming in microcontroller. According to Eq. (6.9) and Eq. (6.10), the variance of $\widehat{c}$ then takes the form:

$$\boxed{\begin{aligned}\sigma(\widehat{c}) &= \frac{1}{\alpha_c\, l}\sqrt{(\mathbf{\Psi}^T\mathbf{\Psi})^{-1}_{11} N \cdot S_{yy} \cdot R} \\ &= \sigma_0 \sqrt{(\mathbf{\Psi}^T\mathbf{\Psi})^{-1}_{11} N}\end{aligned}} \tag{6.40}$$

with σ_0 being the smallest concentration noise that can be obtained:

$$\sigma_0 = \frac{\sqrt{S_{yy}\, R}}{\alpha_c\, l} \tag{6.41}$$

and $(\mathbf{\Psi}^T\mathbf{\Psi})^{-1}_{11}$ is the left top element of the inverse matrix of $\mathbf{\Psi}^T\mathbf{\Psi}$. Note that $\sqrt{(\mathbf{\Psi}^T\mathbf{\Psi})^{-1}_{11} N}$ is a factor depending on the shape of the observed spectra. It is also denoted as 'observation factor' in this work. Smaller values are better and indicate that the observed spectrum has a high information content of the gas concentration. The 'observation factor' has a minimum value of 1 when only the peak value of the absorption line is sampled. Since $(\mathbf{\Psi}^T\mathbf{\Psi})^{-1}_{11}$ is asymptotically inversely proportional to N, the whole factor achieves a steady value for $N \to \infty$, which also represents the continuous situation without sampling.

As given by Eq. (6.34), S_{yy} depends on the laser and detector parameters and the DC photocurrent: the lower the noise induced by laser and detector, the better the sensing sensitivity. α_c and l are gas parameters depending on the gas absorption line to be detected. Probing a strong absorption line and/or increasing optical pathlength, the sensor sensitivity improves. If the measurement rate R is higher, the sensor noise also increases. σ_0 represents the smallest standard deviation of noise on measured concentration that can be achieved when sensor system, measurement rate and absorption line to be detected is fixed. The observation matrix $\mathbf{\Psi}$ can be optimized by adjusting the way of recording of the spectral data. By scanning the wavelength nonlinearly or modifying the WMS modulation index m or varying the scanned wavelength range, the spectral components ψ_i change, which results in the variation of the 'observation factor' and possibly lower values of $\sigma(\widehat{c})$. This concept is introduced in section 6.3.

The analytical closed expression of $\sigma(\widehat{c})$ enables the systematical minimization of the sensor noise and is also advantageous for using time-variant filtering e.g. Kalman filtering (section 6.4), because the time-variant filter coefficients depend on the noise variance, which is also time-variant. However, in order to apply the theories introduced in this section, a linear model is required. For a nonlinear model, the nonlinear parameters would have to be known. The estimation of nonlinear parameters is a challenging task, which is introduced in the following section with two cases discussed: isolated and multi-line model.

6.2 Heuristic parameter estimation

In Tab. 6.2, a comparison between linear and nonlinear least squares curve fit was given. The signal model for the sensor system is a nonlinear signal model containing the nonlinear parameters e.g. gas temperature, gas pressure, spectral wavelength offset, etc... . Although the gas concentration - the parameter of interest - has linear influence in the model, other nonlinear parameters have to be exactly determined for the determination of gas concentration. Furthermore, nonlinear parameters like

pressure or laser tuning coefficients can also be of interest. An additional pressure sensor would increase the sensor cost, and monitoring of laser tuning parameter enables calibration-free operation. Therefore, we estimated the nonlinear parameters using heuristic methods and combine it with linear curve fit for gas concentration estimation or employ a nonlinear fit which needs then only one to two iterations.

Most parts of this section was published within the frame of this work in [116, 68].

6.2.1 Isolated line model: heuristic parameter determination

For an isolated single line, the signal model (Eq. (6.30)) is simplified to a single gas absorption line, i.e. $j_{max} = 1$, background polynomial of zeroth order, i.e. $b_1 = 0$ and only linear tuning ($k_2 = 0$). Because of the small tuning range, the background is modeled with an offset b_0 only and higher order terms like a slope b_1 are omitted, which is however not a limitation and can be extended. Also, the nonlinear laser tuning coefficient k_2 is eliminated because of the small wavelength range that is scanned (less than 1 nm):

$$y = \alpha_c(T)\, c\, l\, S_n(x, m) + b_0 + \epsilon \tag{6.42}$$

where Arndt's formula $S_n(x, m)$ is given in Eq. (3.2.2), with the normalized wavelength x and normalized modulation amplitude m:

$$x = \frac{k}{\gamma_L}\,(I - I_{\text{ofs}}) \qquad I_{\text{ofs}} = \frac{\lambda_c - \lambda_0}{k} \tag{6.43}$$

$$m = \frac{\lambda_a}{\gamma_L} = \frac{k}{\gamma_L}\, I_a\, H(f_m) \qquad \gamma_L = p\,\gamma_{air}(T/296K)^{\zeta} \tag{6.44}$$

The variation of line width γ_L has the same effect as the changing of the linear

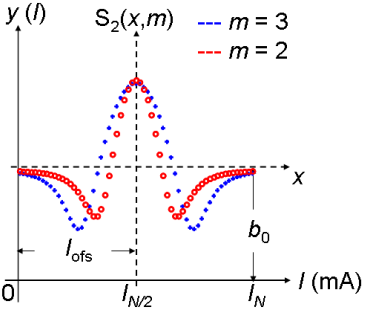

Fig. 6.7: Schematical description for measurement signal and its parameters m (Eq. (6.44)), I_{ofs} and b_0. The scaling parameter between y and $S_2(x, m)$ is the peak absorbance $\alpha_c\, c\, l$

tuning coefficient k. Therefore, it is expected that only the the ratio of k to γ_L can be estimated, i.e. normalized tuning coefficient. The same argument holds also for the normalized wavelength offset $\frac{\lambda_c - \lambda_0}{k}$. Without the knowledge of α_c, c can not be determined and without the knowledge of $\gamma_{air}(T/296K)^{\zeta}$, the pressure p can not be determined. For known normalized tuning coefficient $\frac{k}{\gamma_L}$, the estimation of $H(f_m)$ is

equivalent to the estimation of m, because I_a is known. c, p and T cannot be estimated at the same time with a single line model. Both c and T scale the linestrength and both p and T influence γ_L. Usually, the gas temperature is easily measured with a separate sensor, so this is not really a limitation. The unknown parameters are $\mathbf{u} = [\alpha_c\, c\, l, k/\gamma_L, I_{\text{ofs}}, H(f_m), b_0]$. They are explained in Tab. 6.3 and schematically shown in Fig. 6.7.

Model Parameter	**Definition and explanations**	**Spectrum characteristic values applied for initial value determination**
I_{ofs}	current offset (unit: mA)	the position of max/mins
b_0	y offset (unit: absorbance)	mean value of the whole spectrum
m or equivalently $H(f_m)$	m: normalized modulation amplitude, $H(f_m)$: FM response at modulation frequency f_m	max to min ratio R
$\frac{k}{\gamma_L}$	normalized laser tuning coefficient	max to min ratio R and distance between zero crossings I_z
$\alpha_c\, c\, l$	gas absorbance at center wavelength (unit: 1)	maximum value

Tab. 6.3: The linear/nonlinear parameters of the model as well as the methods to determine their initial values.

Besides baseline offset b_0, the other parameters are nonlinear to the signal model. Now a heuristic method is developed to get good approximation/start values for the parameters. The procedure is shown in Fig. 6.8, and explained in the following steps as well as in Tab. 6.3.

- Step 1: the maximum and the adjacent two minima of the measured data are determined. The average of the minima positions as well as the position of the maximum give the current offset $\widehat{I}_{ofs}$ (Fig. 6.8(a)).
- Step 2: the spectrum is averaged in a symmetrical manner around the maximum to determine y-offset $\widehat{b}_0$, because the second harmonic spectrum theoretically has a mean of zero (Fig. 6.8(b)) according to Hangauer [16].
- Step 3: once the y-offset b_0 is known, the maximum-to-minimum ratio R can be computed and $\widehat{m}$ is obtained by applying the $m(R)$ relationship numerically determined from the Arndt formula (shown in Fig. 6.8(c)). R is defined as $R(m) := \max(S_2(x,m))/\text{-}\min(S_2(x,m))$.
- Step 4: the initial value of the normalized laser tuning coefficient k/γ_L is determined by the distance between the two zero crossings. For this, the difference between zeros in current I_z and its theoretical value x_z is divided, which gives $\widehat{k/\gamma_L} = x_z(R)/I_z$. The $x_z(R)$ relationship is numerically determined from the Arndt formula. I_z is determined from the measured spectrum (see Fig. 6.8(d)).
- Step 5: the initial value of $\alpha_c\, l\, c$ is determined by using maximum point of the measured spectrum divided by $S_2(0,m)$.

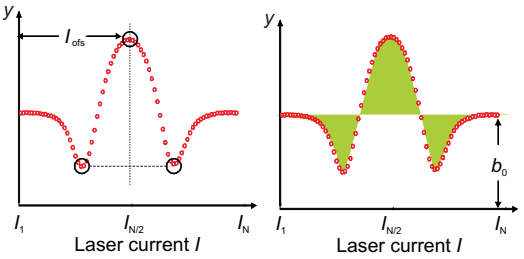

(a) step 1: current of maximum point for I_{ofs}

(b) step 2: averaging of all points for the y-offset: b_0

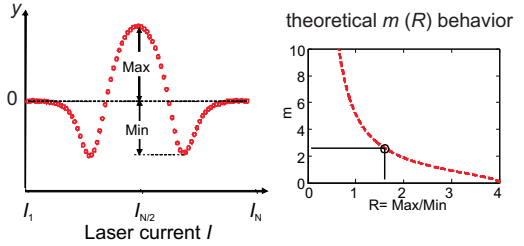

(c) step 3: max/min ratio (R) for m

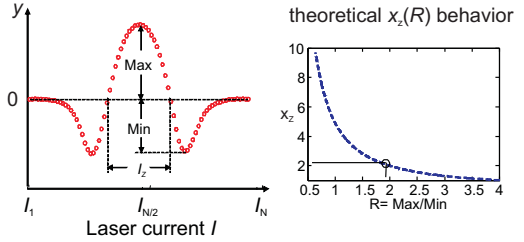

(d) step 4: max/min ratio (R) for x_z, and the ratio between I_z and x_z for normalized tuning coefficient k/γ_L.

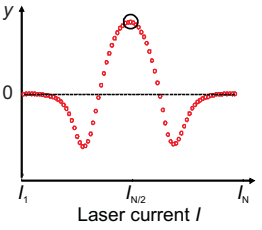

(e) step 5: maximum point for $\alpha_c\, c\, l$

Fig. 6.8: The procedure of pre-calculation: different steps to determine the initial values for different parameters

If the slope b_1 is included in the model, it can be also easily determined by interpolating the two minima. The pre-calculation gives good start values for linearization of the nonlinear model, so that linear curve fits can be carried out. Alternatively, the nonlinear Levenberg-Marquardt curve fit routine is carried out iteratively, with the Jacobian matrix Eq. (6.11) containing the derivatives of the model function with respect to estimated parameter set in the last iteration [117]. To save computing time and capacity in the microcontroller, the Jacobian matrix is programmed analytically instead of estimating it numerically. The operating time is at least two times less compared to numerical estimation of the Jacobian matrix.

In this algorithm, gas temperature is assumed to be known and the temperature correction is applied after the curve fit. m is inversely proportional to gas pressure p with proportionality factor $\frac{\lambda_a}{\gamma_{air}}$ and has a temperature correction term Eq. (6.19).

$$\widehat{p} = \frac{1}{\widehat{m}} \frac{\lambda_a}{\gamma_{air}} \left(\frac{296K}{T} \right)^{\zeta} \tag{6.45}$$

For pressure, $\frac{\lambda_a}{\gamma_{air}}$ and ζ are calibration parameters. The same holds for concentration, which is obtained by dividing the parameter $\widehat{u}_1$ by $\alpha_c\, l$ and corrected with the temperature correction term Eq. (6.20):

$$\widehat{c} = \frac{\widehat{u}_1}{\alpha_c(296K)\, l} \frac{\alpha_c(296K)}{\alpha_c(T)} \tag{6.46}$$

6.2.2 Multi-line model: heuristic pattern recognition

When the scanned spectrum is consisting of multi-absorption lines, the absorption features can be used for determination of the absolute wavelength scale including nonlinear laser tuning coefficient k_2.

In the spectrum scan, at least three gas absorption lines (either reference gas and/or target gas) are used to determine the linear/nonlinear current to wavelength tuning coefficient k, k_2 and wavelength offset λ_0 from Eq. (6.14). It is advantageous to use an integrated reference cell as shown in Fig. 6.2(b) so that always gas absorption lines are present in the scanned spectrum. An example for wavelength scale identification at 2.3 μm using methane as reference gas is shown in Fig. 6.9. A variation of the coefficients (λ_0, k, k_2) is caused by the laser aging, heat sink (T_s) or ambient temperature (T_{amb}) changes, i.e. $\lambda_0 = \lambda_0(T_{\mathrm{amb}}, T_{\mathrm{s}}, t)$. Although the laser heat sink temperature (T_{s}) is controlled by the TEC to be a constant with a precision of 10 mK, there is still an influence of the air temperature (T_{amb}) on the laser chip, because the temperature sensor, which gives a feedback to the TEC, measures the laser chip temperature not directly, but the submount temperature next to the laser chip as shown in Fig. 3.9.

The pattern recognition method for extraction of the wavelength information from a broad second harmonic spectrum (several nm) is briefly outlined here for CO detection at 2.3 μm with CH_4 as reference gas. A detailed description of the developed wavelength identification from the complex spectrum fingerprint was published in [118]. The following steps are taken:

- Estimation of the spectral baseline of the spectrum: Symmetric averaging around each line i.e. red marked area in Fig. 6.9 is used to determine the local baseline offset. This uses the fact that the second harmonic spectrum always has a mean value of zero regardless of the physical line shape (see section 6.2). Then spectral

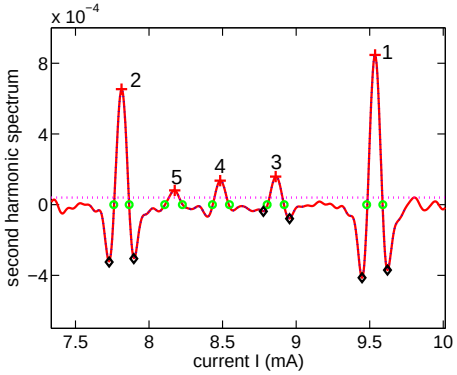

Fig. 6.9: Wide scan (duration: 640 ms, $N = 512$ samples): measured second harmonic spectrum of CO and CH_4 absorption lines at 2.365 μm. The wavelength scale is evaluated by the known wavelength positions of the two strong methane lines (1), (5) and either (3) or (4), depending on which is larger. The resulting wavelength is shown in Fig. 6.10(a) and Fig. 6.10(b)

baseline in the whole scan range is interpolated with a polynomial using the five average values for local areas.

- Determination of the nonlinear current to wavelength tuning behavior $\lambda(I)$: apply a threshold in the measured spectrum (dotted line in Fig. 6.9). Detect the peak values above the threshold. The maxima ('crosses' in Fig. 6.9) are assigned to CO line or methane line peak and the position in current are determined. Then a second order polynomial fit with the found maxima positions in current and the theoretically known center wavelengths of the absorption lines is done to interpolate the parameters λ_0, k and k_2. The measured results are shown in Fig. 6.10 and Fig. 6.11.

- Determination of the bias-current dependent modulation amplitude: the value λ_a (Eq. (6.15)) increases with bias current I as shown in Fig. 6.10(b) and typically decreases with modulation frequency f_m. $d\lambda/dI$ can be derived from the known relationship between λ and current I (Fig. 6.10(b)). $H(f_m)$ can not assumed to be one, especially if the modulation frequency f_m is above or near the 3 dB cutoff frequency of the thermal tuning. For VCSELs the relevant cutoff frequency is several kHz to 100 kHz. f_m is set to 6 kHz, in which case, we determine λ_a additionally from the distance between the zero crossings ('Diamonds' in Fig. 6.9) of the measured second harmonic spectrum λ_z. This is similar as for the single line model except that the absolute wavelength scale is known. By comparing these values and the value given by Eq. (6.15), $H(f_m)$ can be calculated. When calculating the reference spectra for the linear curve fit, λ_a is interpolated from Fig. 6.10(b) and scaled with $H(f_m)$.

Practically, the presented method is used periodically (every few seconds) to recalibrate the wavelength scale, whereas the actual concentration measurement is done

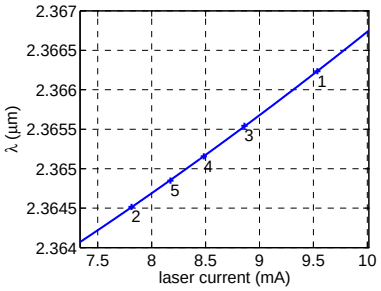

(a) Fitted quadratic relationship between laser current and wavelength for determination of λ_0, k and k_2 Eq. (6.14) for a 2.3 μm InP-based VCSEL

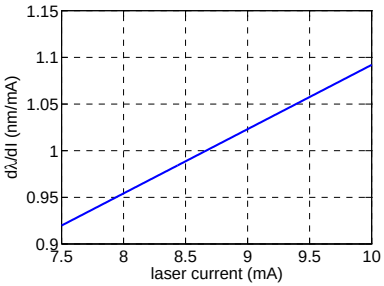

(b) The derivative of the curve shown on the left. λ_a, the modulation amplitude is calculated by applying $d\lambda/dI$ scaled with $H(f_m)$ and I_a (see Eq. (6.15)).

Fig. 6.10: The static laser tuning behavior determined from the absorption features in the 'wide scan' Fig. 6.9

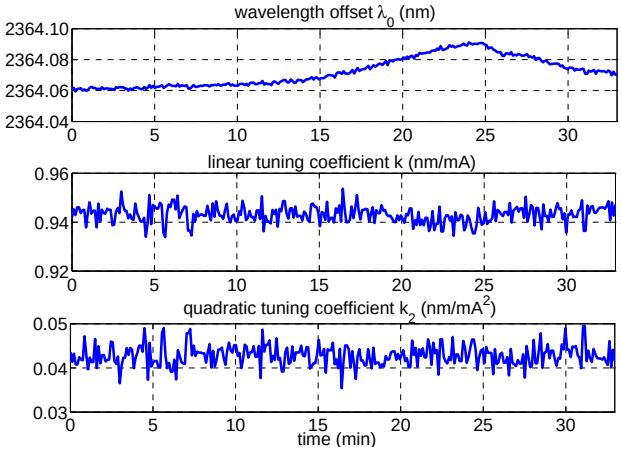

Fig. 6.11: Experimentally determined wavelength offset λ_0, k and k_2 in variation of time for an 2.3 μm InP-based laser. A 40 pm wavelength shift in about half an hour is observed. It corresponds to the HWHM of the absorption line of CO at 2.3 μm.

with narrow spectral scans that only cover the absorption line of the gas of interest. In Fig. 6.11 the measured variation of λ_0, k and k_2 using the heuristic pattern recognition from Fig. 6.9 in half a hour is shown. Laser emission wavelength drift λ_0 is detected with precision < 0.01 nm, which is sufficient for spectral curve fitting. The wavelength drift is due to slight ambient temperature changes that influence the laser chip temperature. No short-term drift is observed for linear and quadratic coefficients. (Might be observable at timescales > 1 year, when laser aging happens). This method is universal and is also used at other wavelengths, e.g. for CO_2 and H_2O detection at 2.004 μm. This was published in [119].

With this method, the absolute wavelength offset, the absolute linear/nonlinear wavelength tuning coefficient can be determined without using an extern reference cell. Furthermore, the dependency on bias-current of modulation amplitude λ_a is also determined, which enables an advantageous linear curve fit, as only the linear parameters c, b_0 and b_1 remain.

6.2.3 Comparison of signal evaluation for the multi-line and the single-line model

parameter	**single-line**	**multi-line**
laser wavelength offset	relative value: $(\lambda_0 - \lambda_c)/\gamma_L$, determined by peak position in spectrum	absolute value: λ_0, determined by line identification
laser wavelength tuning coeff.	relative value: $\frac{k}{\gamma_L}$, nonlinear tuning k_2 neglected, determined by distance of zero crossings	absolute values: k (linear), k_2 (nonlinear), determined by line identification
laser FM response $H(f_m)$	estimated with max-to-min ratio R	estimated with R or better λ_z
modulation amplitude	relative value $m = \frac{\lambda_a}{\gamma_L}$, determined by R	absolute value λ_a, determined by λ_z
background caused by laser AM	only offset b_0 is estimated, determined by averaging whole spectrum	offset b_0 and slope b_1, determined by averaging around each line and interpolation

Tab. 6.4: Comparison between the parameters of single-line and multi-line model.

Here a comparison between the isolated line model and the multi-line model is given (see Tab. 6.4). The isolated line model is applied when the laser tuning range is small or tuning in the spectral range where only single isolated line exist e.g. methane molecule at 1.6 μm or oxygen at 763 nm. In other cases, the multi-line model is applied. For the isolated-line model, estimation of relative parameters is sufficient for the curve fit, neither absolute wavelength scale, nor absolute wavelength difference between two measurement points is needed for concentration determination. Furthermore, in the single line model a curve fit is carried out without knowledge of any molecule parameters and is thus universal to all gases if once calibration with one known gas concentration is performed. Molecule parameters enter the computation only as a calibration factor after the curve fit. The same is true for the temperature correction which is applied to the determined parameter values after the curve fit, with either a theoretical or a

measured correction. For the multi-line model, absolute wavelength scale information including nonlinear tuning parameters are determined periodically, which are used for system monitoring to achieve fail-save operation.

6.3 Optimum spectral sampling

Now the question arises - how to achieve the highest possible sensing sensitivity? This investigation was published in the frame of this work in [120].

According to Eq. (6.40), the analytical expression for the noise variance for a linear curve-fit is:

$$\sigma(\widehat{c}) = \sigma_0 \sqrt{(\mathbf{\Psi}^T \mathbf{\Psi})^{-1}_{11} N} \tag{6.47}$$

$\sigma(\widehat{c})$ can be minimized by changing the observation matrix $\mathbf{\Psi}$, which is varied by optimizing the sampled wavelength points $\lambda_1, \ldots, \lambda_N$.

Usually the laser wavelength/laser current is linearly ramped with respect to time to scan the absorption, so a linear wavelength scanning function [1] as shown in Fig. 6.12(a) is used, i.e.:

$$\lambda_i = \lambda_c + \Delta\lambda\,(i - N/2) \qquad\qquad i = 1, \ldots, N \tag{6.48}$$

The recorded spectrum waveform [2] is equal to gas absorption spectrum. An example is shown in Fig. 6.12 (b) for direct spectroscopy [121], and (c) for WMS second harmonic [14], respectively. After each spectral scan, a curve fit is applied to determine the gas concentration, which is then an output value of the sensor.

However, with linear laser wavelength scanning the signal-to-noise ratio (SNR) on the estimated gas concentration $\sigma(\widehat{c})$ may not be optimal. Basically, if a single line is probed, the gas absorption at center wavelength carries the highest information content of the gas concentration and thus should be sampled more often than the other spectral ranges. This requires nonlinear wavelength sampling. An example is shown in Fig. 6.12 (d), the resulting spectrum waveform is shown in Fig. 6.12 (e) and (f) for direct spectroscopy and WMS, which are more flat at the center wavelength, because more time is spent to sample the center wavelength. An interesting approach was described in [105], which can also be considered as nonlinear scanning. The wavelength scanning jumps over the spectral range where no absorption line is present and therefore optimizes scanning of two separate absorption lines. In the following this approach is generalized and the optimum scanning method and corresponding signal to noise ratio (SNR) improvement is determined.

Here only the white noise contribution of sensor noise is considered, which is the dominating noise source for sensors whose averaging time is well below minimum of the Allan plot. The aim here is to analyze the optimum case, i.e. to determine the upper limit of improvement that is possible to achieve by nonlinear scanning. This method may reduce the optimum averaging time (minimum of the Allan plot), because the white noise suppression is improved. For white noise limited systems (high measurement rate) the concentration resolution is enhanced. The nonlinear scanning method thus either improves sensor response time (for drift or 1/f noise limited systems) or concentration resolution (for white noise limited systems).

[1] The wavelength scanning function is the function describing the laser emission wavelength over time. The wavelength scanning function is applied to scan the gas absorption spectrum.

[2] The spectrum waveform is the signal obtained by scanning the gas absorption spectrum over time with a given wavelength scanning function.

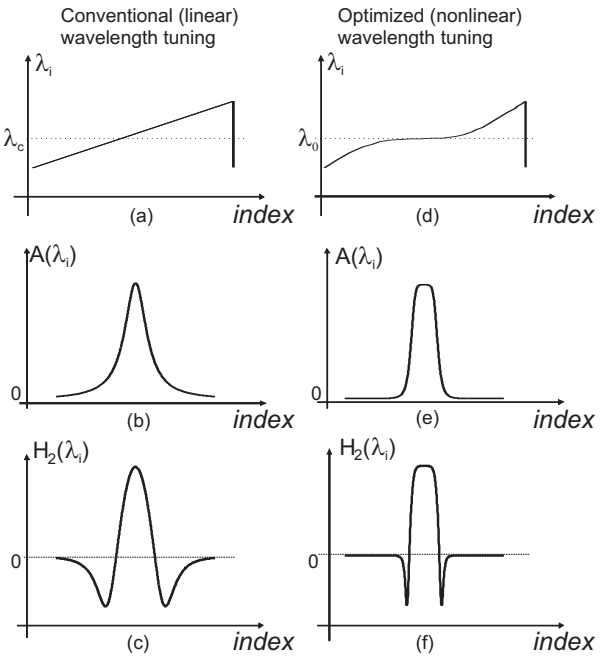

Fig. 6.12: Schematic illustration of the wavelength scanning: conventional (linear) (a) and optimized (nonlinear) (d). The resulting spectrum waveform is shown for direct spectroscopy in (b) for linear scanning and (e) for nonlinear scanning as well as for WMS (second harmonic detection) in (c) and (f).

At first, a simple example is given demonstrating the influence of scan width on the concentration noise. Here, the experiments agree very well with the theory. After that, three different signal models are examined and optimal solutions for optimal scanning waveform are given.

6.3.1 Optimum linear scanning width

A very simple example of this optimum scanning method can be utilized to find out the optimum scanning width of the spectrum in terms of low sensor noise.

For different scanning width, i.e. $\lambda_N - \lambda_1$, the ψ vectors are different. The normalized standard deviation $\sigma(\widehat{c})/\sigma_0 = \sqrt{(\mathbf{\Psi}^T\mathbf{\Psi})^{-1}_{11}}\,N$, i.e. the observation factor versus the width of the narrow scan is shown in Fig. 6.13. The signal model used here is a linear model consisting of four components: target gas spectrum, interfering gas spectrum, slope and offset. [3]

Theory and experiment agree that optimal sampling width in this case is 9 times HWHM of the absorption line. The improvement over a scan with width of 20 times

[3] A low pass filter is utilized before the curve fit to filter the measurement noise of $\mathbf{y}$. Then the

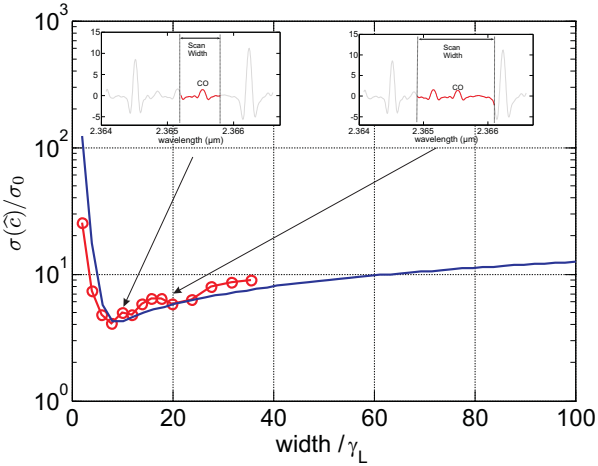

Fig. 6.13: Standard deviation $\sigma(\hat{c})$ versus spectrum scanning width for CO detection at 2.3 μm. $9 \times \gamma_L$ is the optimum value. 100 times scan width (Fig. 6.9) is too broad for optimum curve fit because the information content of CO absorption in the outside range is low. Scanning of a too small spectral range dismisses the information of baseline, so that the estimation of c and baseline b_0 and b_1 becomes difficult.

HWHM is about 33 % . The good agreement of experiment and theory proves the applicability of the theory, so it can also be applied for other spectral regions as well.

In the following, an universal criterion to determine the optimum spectrum waveform and thus also the corresponding wavelength scanning function is given. This includes how broad the scanned spectral range should be and - if WMS is applied - the optimum modulation index m.

6.3.2 Optimal nonlinear wavelength scanning and spectrum waveform

The optimal spectral waveform depends on the signal model. The more components are included in the signal model and more parameters are fitted, the less gain in SNR on the estimated target gas concentration value by the curve fit is achieved. Degradation in signal to noise ratio is only avoided if the additional components are orthogonal to the existing ones. Different signal models for the measurement data can be distinguished by the a-priori information which is available in the specific situation. The 'value' of the a-priori information can be determined, because different models give different SNR improvement in the curve fit. For example, it turns out that by knowing the

normalized standard deviation of gas concentration noise can be written as:

$$\sigma(\hat{c}) = \sigma_0 \sqrt{N} \left| ((\mathbf{\Psi}^T \mathbf{\Psi})^{-1} \mathbf{\Psi}^T)_1 * h \right| \tag{6.49}$$

The * denotes the convolution operator. $(X)_1$ specifies the first row of a matrix X. h is the impulse response of the low pass filter with its mean square value $|h|$ normalized to one.

spectral baseline the sensor resolution can theoretically be a factor of 2 better than without the knowledge of spectral baseline (see Tab. 6.5).

Here three linear signal models are discussed: (I) only the gas concentration is fitted (spectral baseline and spectral components and concentration of interfering gases are known) (II) target gas concentration and linear baseline are fitted and (III) concentration of target gas and interfering gas, spectral baselines and the amplitude and phase of etalon fringes with known period length are fitted. We derive the optimum wavelength scanning function analytically for model (I) and (II) and numerically for model (III).

Signal model I: only target gas concentration is unknown

If the spectral baseline is known, and there is no interfering gas or the concentration and spectrum of the interfering gas is known, the model is written as:

$$\mathbf{y} = (\psi_1)\,(\alpha_c\, c\, l) + \epsilon \tag{6.50}$$

where $\mathbf{y}$ is the measured data with baseline and interfering gas spectrum removed.

Substituting the model in Eq. (6.40) gives:

$$\sigma(\widehat{c}) = \frac{\sigma_0}{|\psi_1|/\sqrt{N}} \tag{6.51}$$

It is evident that Eq. (6.51) is minimized, if the root mean square (RMS) $|\psi_1|/\sqrt{N}$ of the vector ψ_1 is maximized. This is achieved by sampling the absorption spectrum only at its absorption maximum (peak) value. This gives

$$\psi_{1,opt} = (\psi_1(\lambda_c), ..., \psi_1(\lambda_c))^T\,, \tag{6.52}$$

with

$$\lambda_{i,opt} = \lambda_c = \underset{\lambda}{\operatorname{argmax}}(\psi_1(\lambda)), \tag{6.53}$$

which results in:

$$\sigma(\widehat{c})_{opt} = \frac{\sigma_0}{\psi_1(\lambda_c)} \tag{6.54}$$

The corresponding spectrum waveform carries the constant value $\psi_1(\lambda_c)$, which is 1 for direct spectroscopy and 0.343 for second harmonic detection, with the modulation index $m = 2.2$. m is chosen for a maximum signal peak height. For this model with known baseline and known interfering gas spectrum, if there is any, it is thus optimal to sample only the maximum value of the gas absorption spectrum or the WMS harmonic spectrum.

Signal model II: target gas concentration and baseline (slope, offset) are unknown

In this case the signal model is consisting of the spectral component belonging to the target gas and spectral baseline consisting of a slope and offset.

$$\mathbf{y} = (\psi_1|\psi_2|\psi_3) \begin{pmatrix} \alpha_c\, c\, l \\ b_1 \\ b_0 \end{pmatrix} + \epsilon \tag{6.55}$$

with the new baseline components for offset and slope:

$$\psi_2(\lambda_i) = (1, ..., 1)^T \qquad \text{(offset)} \tag{6.56}$$

$$\psi_3(\lambda_i) = (-1, ..., 1)^T \qquad \text{(slope)} \tag{6.57}$$

Note that the slope component of the spectral baseline also changes in a nonlinear fashion when the wavelength is scanned nonlinearly. Under the assumption that $\psi_1(\lambda)$ is symmetric, $\sigma(\widehat{c})$ is given by :

$$\sigma(\widehat{c}) = \frac{\sigma_0}{\sqrt{|\psi_1|^2/N - \overline{\psi}_1^2}} \tag{6.58}$$

$\overline{\psi}_1$ denotes the average value of the elements of vector ψ_1. Note $\sqrt{|\psi_1|^2/N - \overline{\psi}_1^2}$ gives the standard deviation of the values of vector ψ_1. By maximizing this value, $\sigma(\widehat{c})$ is minimized. It is evident that N also has almost no influence on the optimal case. It follows that this requires sampling the minimum and maximum points of the spectrum only. Knowing this, it follows by a simple calculation that the optimum is achieved by sampling the maximum and minimum of the spectrum equally often and in a symmetrical manner as required by the assumption:

$$\psi_{1,opt} = (\underbrace{\psi_1(\lambda_m)...}_{N/4}\underbrace{\psi_1(\lambda_c)...}_{N/2}\underbrace{\psi_1(\lambda_m)...}_{N/4})^T, \tag{6.59}$$

with

$$\lambda_c = \underset{\lambda}{\text{argmax}}(\psi_1(\lambda)) \qquad\qquad \lambda_m = \underset{\lambda}{\text{argmin}}(\psi_1(\lambda)) \tag{6.60}$$

The minimized noise variance then has the expression:

$$\sigma(\widehat{c})_{opt} = \frac{2\,\sigma_0}{|\psi_{1,max} - \psi_{1,min}|} \tag{6.61}$$

For direct spectroscopy we have $\psi_1(\lambda_c) = 1$, $\psi_1(\lambda_m) \approx 0$, and $\sigma(\widehat{c})_{opt} = 2\,\sigma_0$. For second harmonic detection, the peak to peak amplitude of the second harmonic spectrum is maximum when m is set to 3 [67], which gives $\psi_1(\lambda_c) = 0.33$, $\psi_1(\lambda_m) \approx -0.22$ and $\sigma(\widehat{c})_{opt} = 3.6\,\sigma_0$. The optimum spectral waveforms for target gas ψ_1 and the wavelength scanning function are shown in Fig. 6.14.

Signal Model III: target gas, baseline, interfering gases and etalon fringes are unknown

In this section, also an interfering gas spectrum and etalon fringes are included in the model.

$\sigma(\widehat{c})$ can be only minimized numerically. The optimization problem is:

$$\textbf{minimize}(\boldsymbol{\Psi}^T\boldsymbol{\Psi})^{-1}_{11} \tag{6.62}$$

$$\textbf{subject to } \lambda_{\min} \le \lambda_1 \le \lambda_2 \le \cdots \le \lambda_N \le \lambda_{\max} \tag{6.63}$$

The algorithms for constraint optimization problem [122] is described in [123, 124], and implemented in the MATLAB function 'fmincon'. We demonstrate the numerical optimization for CO detection at 2.365 μm with the interfering gas methane. For this case, the spectral compositions ψ_i are shown in Fig. 6.15. The results obtained are shown in Fig. 6.16(a) and Fig. 6.16(b) for direct spectroscopy and second harmonic detection, respectively. It is remarkable that also in the numerically optimized case

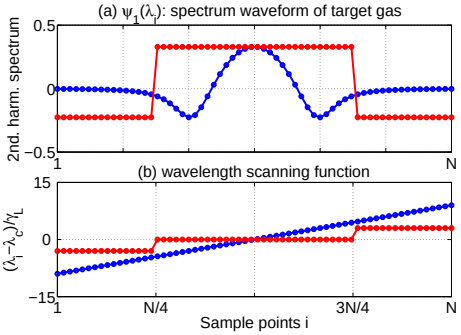

Fig. 6.14: The scanning waveform (second harmonic spectrum) for target gas (a) and the wavelength scanning function (b) for model II (including baseline, but no interfering gas). Traditional linear scanning (blue) and proposed optimum scanning (red) are both presented. The y-axis of (b) is normalized wavelength, which is relative to the line center λ_c normalized with the HWHM of the gas absorption line γ_L.

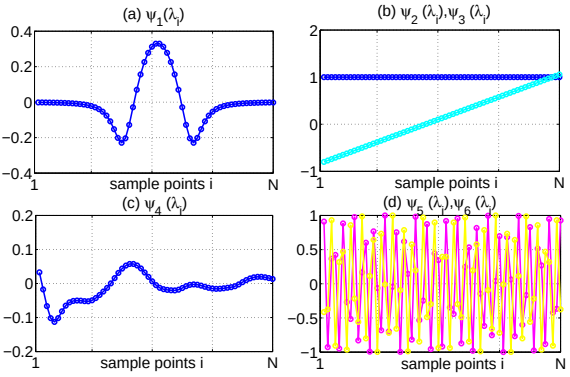

Fig. 6.15: Example of simulated spectral compositions ψ_i in Model III: ψ_1 is second harmonic spectrum of CO at 2.365 μm (a) with interfering gas methane ψ_4 (second harmonic spectrum of 20 methane lines) (c); ψ_2 and ψ_3 (b) are the spectral baseline: offset and slope; ψ_5 and ψ_6 (d) are the sampled sine and cosine components forming the etalon fringes.

the optimum wavelength scanning function has a cascade structure. The maximum is more often sampled than in the linear scanning case. The algorithm determines the modulation index m to 3, so the peak to peak amplitude of the second harmonic spectrum is maximized as in model II theoretically derived. On the other hand, the transitions from minimum to maximum are also sampled to obtain the information of the methane spectrum and to average over one period of the etalon fringes.

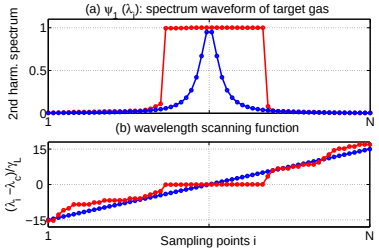

(a) The spectral waveform (direct absorption spectrum) for target gas CO (top) and the wavelength scanning function (bottom). Traditional linear scanning (blue) and proposed optimum scanning (red) are both presented.

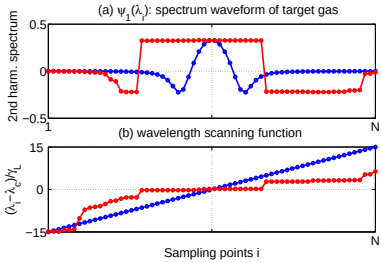

(b) The spectral waveform (second harmonic spectrum) for target gas CO (top) and the wavelength scanning function (bottom). Traditional linear scanning (blue) and proposed optimum scanning (red) are both presented.

Fig. 6.16: Numerically determined optimum wavelength scanning for model III

One interesting thing to note is that, sampling at K discrete wavelength points appears to be sufficient for the estimation of K unknown parameters. The results for Model I and II approve this theory: i.e. if only the target gas concentration is to be estimated, sampling only at maximum is sufficient; if gas concentration, slope and offset are to be estimated, maximum and two minima are to be sampled. This theory gives additionally the fraction of the total time these points should be sampled. Another knowledge is that once the spectral baseline is unknown, the modulation index m for WMS is optimally chosen to maximize the peak to peak value of the signal ($m = 3$), not the maximum value ($m = 2.2$), which is however usually applied in the literature [14].

To use this method, knowledge of wavelength and the laser current-to-wavelength relationship is essential. To obtain the laser current to wavelength relationship $\lambda(I)$, an inherent wavelength calibration technique is needed as in section 6.2.2. $I_i = \lambda^{-1}(\lambda_i)$ can be thus computed. Furthermore, exact knowledge on λ_a is necessary, because it strongly influence the position of the minimum.

6.3.3 Comparison between linear and nonlinear wavelength scanning

The observation factor $\sqrt{(\mathbf{\Psi}^T\,\mathbf{\Psi})^{-1}_{11}\,N}$ is a figure of merit for spectral scanning. It is used for comparison of linear scanning and nonlinear wavelength scanning applying direct spectroscopy (section 3.2.1) or WMS (Tab. 6.5). This value is independent of the absorption coefficient (given by α_c), optical path length l, sensor time resolution R and noise power density on measured spectra S_{yy}. The lower values are better. Different models represent different levels of available a-priori information. For model I the spectral baseline is known, for model II, it is unknown and model III additionally

handles interfering gases and interference fringes section 6.3.2).

$\frac{\sigma(\widehat{c})\,\alpha_c\,l}{\sqrt{S_{yy}\,R}} = \sqrt{(\mathbf{\Psi}^T\mathbf{\Psi})^{-1}_{11}N}$	direct spectroscopy		WMS (2nd harm.)	
	optimum nonlinear scanning	linear scanning [1]	optimum nonlinear scanning	linear scanning [1]
I	1	2.8	2.9 [2]	5.9
II	2	3.6	3.6 [3]	5.9
III	2.2	4.2	4.2 [3]	7.6

[1] The width of the linear wavelength scanning is chosen as 12 × HWHM of gas absorption line for model I and II, and 20 × HWHM of gas absorption line for model III.
[2] Modulation index adjusted to maximize spectrum waveform peak ($m_{opt} \approx 2.2$)
[3] Modulation index adjusted to maximize spectrum waveform amplitude (peak to peak) ($m_{opt} \approx 3$)

Tab. 6.5: List of $\frac{\sigma(\widehat{c})\,\alpha_c\,l}{\sqrt{S_{yy}\,R}}$ values for the comparison of linear scanning and nonlinear wavelength scanning applying direct spectroscopy or WMS. Lower values are better.

The width of the linear wavelength scanning is chosen as 12× HWHM of gas absorption line for model I and II, and 20× HWHM of gas absorption line for model III because of the involvement of interfering gas. According to the Tab. 6.5, the standard deviation of concentration noise/ sensor detection sensitivity can be improved by a factor ∼2 by applying nonlinear wavelength scanning instead of linear scanning for direct spectroscopy and WMS. Furthermore, an additional factor of ∼2 lower standard deviation can be achieved theoretically if direct spectroscopy instead of second harmonic detection is applied. This can be explained by the two times larger peak to peak value of the direct spectroscopy spectrum compared to the second-harmonic spectrum.

Using the data of CO sensor (section 7.3.3), the sensor sensitivity is calculated as 2.1 ppm, and measured as 2 ppm. This can theoretically be improved by a factor of 1.8 (1.2 ppm), if nonlinear wavelength scanning with second harmonic detection is applied or by a factor of 3.3 (0.6 ppm) using direct spectroscopy with optimum nonlinear wavelength scanning.

6.4 Post curve fit Kalman filtering

The linear curve fit with optimal scan width is the best of any linear time-invariant filtering. The performance can be further improved, if time invariant filter e.g. Kalman filtering is applied to separate the system noise from the real concentration variation.

Kalman filter is initially utilized for tracking of the position of objects. It combines and weights two noisy information to give a better estimation. The weighting factor is 'Kalman gain' and changes iteratively depending on the actual situation. Therefore, unlike conventional linear filter e.g. Wiener-filter [103], Kalman filter [106] is time-variant. It is a least squares estimator in the context of time-variant models. Its 'bandwidth' changes over time depending on the actual situation of the sensor and gas, i.e. the variance of system noise introduced by the sensor itself and real gas concentration fluctuation.

Signal Model for Kalman filtering

The block diagram of Kalman filter employed for gas sensing is shown in Fig. 6.17. The input and output of Kalman filter are $\widehat{c}(k)$ and $\widetilde{c}(k)$, respectively. The index k is a discrete time and denotes the k-th measurement. To employ the Kalman filter, models

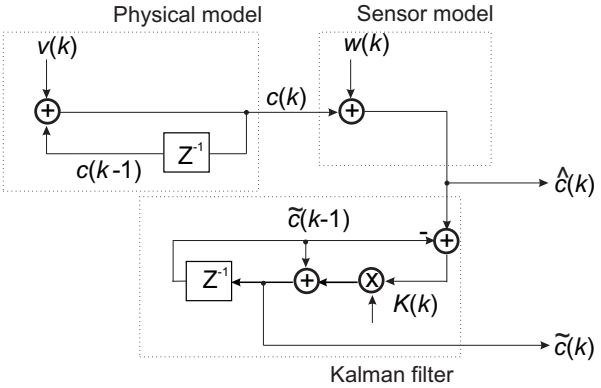

Fig. 6.17: The block diagram of the functionality of Kalman filter. $\widetilde{c}(k)$ is the concentration value estimated with utilization of Kalman filtering. $\widehat{c}(k)$ is estimated concentration value after the curve fit, without utilization of Kalman filter. The physical model depicting the real concentration fluctuation $c(k)$ is a random walk model described by Riris (Eq. (6.64)); the detected value by the sensor $\widehat{c}(k)$ is the real concentration value overlapped with white noise $w(k)$. Kalman filtering gives an estimation $\widetilde{c}(k)$ of the real concentration using the Kalman gain $K(k)$, which is calculated by knowing the variances of the measurement noise and the variance of the real concentration fluctuation.

are needed for the two informations required by the Kalman filter: a dynamical signal model to describe the real gas concentration fluctuation and a model of the sensor systems induced noise. Here the random walk model given by Riris [107] to describe the real gas concentration variation is applied, because during the investigations, it turned out to give the best results.

$$\text{Physical model:} \qquad c(k+1) = c(k) + v(k) \tag{6.64}$$

The gas concentration is modeled to change randomly. $v(k)$ is assumed to have white noise character, i.e. its noise power density is constant.

The detected concentration value of the sensor without Kalman filter is the real concentration superimposed with $w(k)$, which is the measurement noise introduced by the sensor system. This also assumed to have white noise character:

$$\text{Sensor model:} \qquad \widehat{c}(k) = c(k) + w(k) \tag{6.65}$$

Both $v(k)$ and $w(k)$ are time-variant processes, i.e. their statistical properties change with time. To adjust its filter bandwidth, Kalman gain $K(k)$ is determined by knowing the time-variant $\sigma^2(v(k))$ and $\sigma^2(w(k))$. The difficulty for applying Kalman filter in gas spectroscopy lies in the real time estimation of the noise variances. The Kalman

filter output is given by:

$$\widetilde{c}(k) = \widetilde{c}(k-1) + K(k)\,(\widehat{c}(k) - \widetilde{c}(k-1)) \tag{6.66}$$

$$K(k) = \frac{\sigma^2(w(k-1))\,K(k-1) + \sigma^2(v(k))}{\sigma^2(w(k)) + \sigma^2(v(k)) + \sigma^2(w(k-1))\,K(k-1)} \tag{6.67}$$

Determination of $\sigma^2(v(k))$ and $\sigma^2(w(k))$

The determination of both variances is usually a difficult task for employing Kalman filtering, inaccurate estimation of the variances will result in time delay (estimation of $\sigma^2(w(k))$ is too large) or less filtering effect (estimation of $\sigma(w^2(k))$ is too small). In literature for laser spectroscopic application, it is assumed that $\sigma(v^2(k))$ and $\sigma(w^2(k))$ have a certain ratio to each other [108]. This is usually not the case in a real physical environment, because real concentration fluctuations and the sensor system noise are two independent processes and their variations are independent.

To overcome this limitation, a new method to determine both variances is developed and applied for the first time: $w(k)$ is the noise of the measurement system and $\sigma^2(w(k))$ has a linear relationship to S_{yy} (Eq. (6.40)) with the proportional factor $\sqrt{(\mathbf{\Psi}^T\,\mathbf{\Psi})^{-1}_{11}N}$ specifying the signal-model used for curve-fitting. S_{yy} can be theoretically calculated by knowing the DC photocurrent D_0, laser RIN and preamplifier resistance R_v (see Eq. (6.34)). Practically, additional noise from the electronics may be present. Also for a nonlinear curve fit, the 'observation factor' $\sqrt{(\mathbf{\Psi}^T\,\mathbf{\Psi})^{-1}_{11}N}$ has a value that is not known a-priori. Therefore, an optional calibration for the S_{yy} as a function of detector current D_0 and a one-time calibration for $\sqrt{(\mathbf{\Psi}^T\,\mathbf{\Psi})^{-1}_{11}N}$ can be carried out.

Tab. 6.6: The variances needed for Kalman filtering and their determination methods

Variance	**Determination Method**
$\sigma^2(w(k))$	Using Eq. (6.40) with $S_{yy}(D_0)$ determined by Eq. (6.34) or by a one-time calibration.
$\sigma^2(v(k))$	$\sigma^2(v(k)) = \sigma^2(\widehat{c}(k)) - \sigma^2(w(k))$, $\sigma^2(\widehat{c}(k))$ is determined by estimating the variance of the past 20 concentration values

$v(k)$ and $w(k)$ are assumed to be uncorrelated to each other, this is reasonable because the real concentration fluctuation has no influence on the measurement noise introduced by the sensor. Therefore, the variance of their sum, which is the variance of the measured concentration, equals the sum of their variances. Deriving from Eq. (6.65), it is obtained:

$$\sigma^2(\widehat{c}(k)) = \sigma^2(c(k)) + \sigma^2(v(k)) \tag{6.68}$$

$$= \sigma^2(w(k)) + \sigma^2(v(k)) \tag{6.69}$$

$\sigma^2(\widehat{c})$ is determined by evaluating several previously estimated concentration values (Eq. (6.70)).

$$\sigma^2(\widehat{c}(k)) \approx \frac{1}{W}\sum_{i=0}^{W-1}\widehat{c}(k-i)^2 - \left(\frac{1}{W}\sum_{i=0}^{W-1}\widehat{c}(k-i)\right)^2 \tag{6.70}$$

W is the number of the values being used. There is a trade off between the accuracy of the estimated variance and the system time response. In our case, $W = 20$ values are taken with concentration measurement rate $R = 1$ Hz, which is an empirical value given a good compromise with respect to system time response and estimation accuracy of the variance. An overview of the determination of $\sigma^2(v(k))$ and $\sigma^2(w(k))$ is shown in Tab. 6.6.

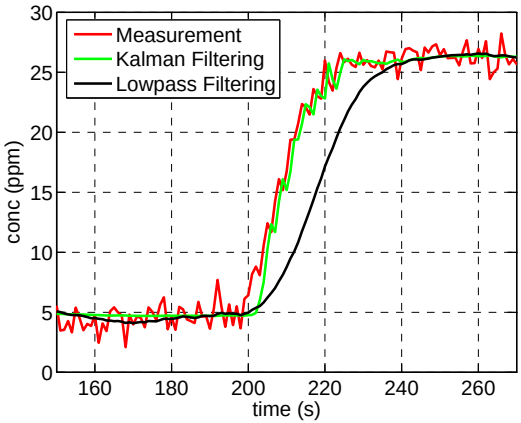

Fig. 6.18: Simulated comparison of Kalman filtering and time-invariant low pass filtering. It is clearly visible that the first order lowpass has a certain delay, when a sudden concentration change occurs. This is not the case for the Kalman filter.

A comparison of Kalman filtering and a time-invariant low pass is shown in Fig. 6.4. For the time-invariant lowpass filter (i.e. bandwidth fixed), there is a trade-off between filter bandwidth and real time operation. Using a small bandwidth to filter the overall noise, a certain delay is given when a sudden concentration change occurs like the case shown in the Figure. In contrary, the bandwidth of Kalman filter is adjusted to the measurement data, i.e. gas concentration. For low fluctuations in the real gas concentration, low bandwidth is applied, whereas when the real concentration strongly varies, the bandwidth is set high. Four times sensitivity improvement was achieved with Kalman filter applied in an oxygen sensor for combustion optimization in a gas furnace (section 7.2).

6.5 Conclusion

In this chapter, signal processing methods with low-complexity were developed, aiming at high-sensitivity and fail-save operation. No separate reference cells or etalons are used.

Heuristic algorithm and linear curve fit All laser parameters are extracted from the measured spectra. These consist of DC current to wavelength tuning parameters k, k_2, λ_0 and the FM response $H(f_m)$. For detection of trace gases, the spectral features

are provided by a reference gas that is a non-target gas integrated into the absorption path, for example within the photodetector housing. Monitoring of laser operation and wavelength stabilization is therefore possible, which enables fail-save operation without using the extra optical components. For the curve fit, a VCSEL-specified signal model for measured WMS signal is developed. To achieve fast and reliable operation, the nonlinear parameters are estimated with heuristic methods at first. Then either a nonlinear curve fit with very few iterations is carried out because of very good initial values, or linear curve fit is directly implemented. Linear curve fit is non-iterative and provides both a closed expression for the sensor output (Eq. (6.39)) as well as the sensor noise variance (Eq. (6.40)). In this case even the entire sensor performance can be predicted theoretically.

Optimum spectral sampling With respect to sensitive gas sensing, optimal wavelength sampling is investigated based on the derived analytical formula for sensor noise (Eq. (6.40)). Optimal wavelength scanning enables a more efficient curve fit than for traditional linear wavelength scanning and therefore minimizes the influence of white noise on the determined concentration values. The optimal scanning function depends on signal models for curve fit. While for the simple models, analytical solutions for minimal sensor noise are found, the more comprehensive cases like model including interfering gas components, etalon fringes, were handled numerically. The optimum spectrum waveforms have a cascade structure which means that the optimum scanning only samples important points of the spectrum. The theory not only shows that sampling at N discrete points for N unknown parameters is both necessary and sufficient for the determination of minimum noise concentration, but also gives which points are to be sampled and in which fraction of time. Maximum sampling is preferred if baseline is known and otherwise, minima and maxima should be sampled equally often. The normalized modulation amplitude m is set to 3 to give the maximal peak-to-peak value of the WMS signal. This shows that the previous approach in literature with setting $m = 2.2$ for maximum signal peak is not optimum. According to the figure of merit for spectral scanning, the observation factor $\sqrt{(\mathbf{\Psi}^T \mathbf{\Psi})^{-1}_{11} N}$, the new method theoretically enables a factor of $\sim$2 improvement on concentration noise compared to linear wavelength scanning. Furthermore, direct spectroscopy is theoretically superior to second harmonic detection, because the concentration noise can be an additional factor of $\sim$2 lower. The theoretical prediction of sensor noise in Eq. (6.40) is also confirmed by the experimental results of a CO sensor shown in section 7.3.

Optimum filtering Kalman filtering is applied for real-time high sensitive gas sensing. Fur this purpose, the variances of measurement noise and real concentration fluctuation have to be estimated continuously. This work overcomes the limitation in the literature that the variations are poorly determined and the filtering effect of the Kalman filter is either too low or too high for the specific situation. The new method to determine the variances is based on linear model system, by calculating the noise variance theoretically with Eq. (6.40) or by using an empirically determined dependence of sensor noise on incident detector power. Kalman filtering shows promising result for noise filtering of the oxygen concentration for application in gas furnaces (section 7.2.4).

7 Practical sensor realization

7.1 Introduction

Within this work, three sensor prototypes were developed utilizing the components and methods investigated in the previous sections:

- An oxygen sensor for combustion optimization. While complex and rather expensive TDLS sensor systems are already employed in process monitoring applications e.g. in power plants [125], they are not yet applied in medium or small scale burners e.g. for domestic heating appliances because there compact and low cost sensors are needed. Results were published within frame of this work in [68, 69, 70].

- A carbon monoxide sensor for safety monitoring, e.g. threshold value (TLV) monitoring in working places (TLV: 30 ppm), fire detection or industry applications e.g. optimization of burning process in gas/oil furnaces. Here operation at medium sensitivity is required (ppm resolution). Results were published within frame of this work in [116, 126, 127].

- A carbon monoxide sensor for medical applications e.g. breath analysis or fire detection. Here operation at high sensitivity is required (100 ppb resolution). Published within frame of this work in [128, 84].

7.2 Oxygen sensor using a diffuse reflector-based optical cell and advanced signal processing

7.2.1 Motivation

For combustion applications in gas furnaces, optimization of the burning process is very important for energy savings, reduction of pollutants emission and avoiding toxic pollutants emission. Monitoring of the oxygen (O_2) content of the exhaust gas allows for an effective combustion control. For a large scale gas furnaces with several MW power, the oxygen concentration is regulated to 1 vol% - 2 vol% with utilization of an oxygen sensor and a control loop. Without using an oxygen sensor the burner has to be adjusted in a way that with varying gas quality and varying air density (summer/winter) the burning process is still complete, i.e. no high levels of carbon monoxide are generated. In this case the O_2 content in the exhaust can be 4 vol% - 6 vol%. For wall-hanging gas-boilers in households the oxygen content is adjusted to 4 vol% - 6 vol%, compared to 7 vol% - 8 vol% without regulation with an oxygen sensor [129]. Deriving from Siegert's formula [130], the following relationship between the improvement of efficiency Δq_A and oxygen context change Δc_{O_2} is obtained:

$$\Delta q_A = (T_{exh} - T_{air})\, A_2\, \frac{\Delta c_{O_2}}{(21 - c_{O_2})\,(21 - c_{O_2} + \Delta c_{O_2})} \tag{7.1}$$

For natural gas, the constant A_2 is 0.66 %/K. For gas furnace, the difference between the temperature of exhaust T_{exh} and the temperature of the ambient air T_{air} is 100 K. Therefore, by reducing the O_2 content in the exhaust by $\Delta c_{O_2} = 4.5$ vol% from $c_{O_2} = 6$ vol% the efficiency of the furnace can be improved by approximately 1 % because the energy used to heat up this oxygen is no longer lost (This is in agreement with Ref. [131]).

An oxygen sensor thus enables optimum operation under different gas quality and ambient temperature conditions and eliminates the need for manual adjustment. This is especially important with a liberalized gas-market in the E.U. since the gas quality (i.e. calorific value) can not be assumed to be constant.

The requirements for such oxygen sensors are fast time response (second range), high accuracy (0.1 vol% resolution), selectivity, in-situ measurement capability, and long term stable operation even under harsh conditions in an exhaust gas pipe. The conventional technology - the ZrO_2 based lambda probes [132] are widely used in cars and also in medium or large scale heater appliances. Nevertheless, these sensors suffer from several drawbacks:

- Despite the normal aging of the probe (up to three years are typically guaranteed in a furnace application), these sensors can be poisoned with heavy metals (e.g. Mn, Pb).

- Grids for flame protection or porous sinter metals as gas inlet are needed due to the high operating temperature of the sensor, to prevent ignition of unburned gas. This increases both complexity and response time of the sensor.

- The high operating temperature of ZrO_2 sensor of above 600 °C has to be well controlled, because any temperature variation will result in a change of the measured signal (Nernst potential). Furthermore, the high temperature operation causes a high continuous power consumption and introduces a delay time of several seconds until the sensor is ready to measure after switching-on.

Thus, a tunable diode laser spectroscopy (TDLS) based sensor is a very attractive alternative to the ZrO_2 sensor for combustion optimization, since it has superior properties with respect to all mentioned factors.

However, the challenges for the laser-optic oxygen sensor are:

- The sensor must be long-term stable, which means the sensor optics must withstand the temperature cycles in the exhaust gas and must not get misaligned during the whole sensor lifetime (up to 10 years). And the sensor must also be robust against condensation or contamination on the optical surfaces. These may cause a certain decrease of the light power arriving on the photodiode. However, TDLS based sensors are intrinsically insensitive to overall attenuation in the optical path because of the spectroscopic measurement. Just the resolution depends on the absolute light intensity arriving at the photodetector (see Eq. (6.34)).

- The sensor must be compact (dimension: around 10 cm × 10 cm) and based on computationally efficient algorithms. This is because for in-situ measurement, the sensor optic must be compact enough, so that it can be mounted in the exhaust gas pipe. Extractive gas measurement is too slow for real time operation.

The presented solution to these problems is the utilization of a diffuse reflector (section 5.4) and a development of a microcontroller-suited on-line curvefit algorithm

based on the single line model (section 6.2.1), combining the heuristic parameter pre-calculation and nonlinear curve fit (Fig. 7.1). These are explained in section 7.2.2 and section 7.2.3, respectively. Additionally, Kalman filtering (section 6.4) is applied to further reduce the measurement noise of the concentration value without increasing the sensor response time. Furthermore, gas pressure can be estimated simultaneously using the on-line curve fit algorithm (section 7.2.4).

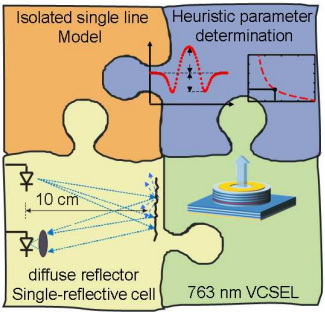

Fig. 7.1: The components of the O_2 sensor: diffuse reflector based single-reflective cell (section 5.4), 763 nm GaAs-based VCSEL, isolated single line model with heuristic parameter pre-calculation (section 6.2.1) and nonlinear curve fit (VCSEL image by O. Dier).

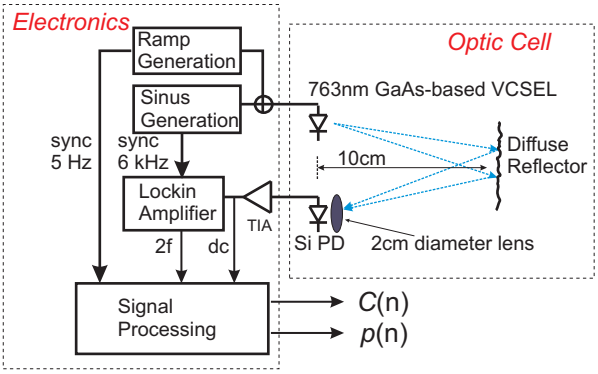

Fig. 7.2: Layout of the oxygen sensor consisting of an optic cell with diffuse reflective geometry and microcontroller-based electronics. $C(n)$ and $p(n)$ are the sensor outputs, which represent the n-th estimated gas concentration and pressure value.

7.2.2 Design of sensor optics

The sensor probes an O_2 absorption line at a wavelength of 763 nm, where low cost VCSELs are available [53]. A structural diagram of the whole sensor is shown in Fig. 7.2. The sensor has a reflective geometry with laser and photodetector side by side

and both directed at a reflector at 10 cm distance. A photograph of the sensor's optic cell is shown in Fig. 7.3(a). The laser beam passes through a window with Brewster angle and is reflected at the rough surface of the diffuse reflector, which is made of anodized aluminum with a surface roughness of 1-2 μm. The reflected light interferes at different positions on the photodetector, which results in a laser speckle pattern, i.e. a spatial distribution of interfering light modes on the surface of the detector. To collect as much light as possible, the 3 mm diameter silicon photodetector is equipped with a 2 cm diameter lens, which projects an image of the reflector onto the detector (Fig. 7.3(b)). The spectral background of the cell was measured to be the order of 10^{-5} (Fig. 5.7), given by a reflection between laser chip and the Brewster window. The back-reflection from the laser window to the laser chip is because the laser beam has a certain divergence. The speckle noise is far below 10^{-5} as derived in section 5.4. If the laser window is improved, the cell background would be even lower.

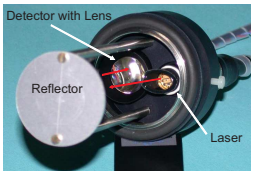

(a) Photograph of the sensor optic cell. The VCSEL emitted light is reflected by the diffuse reflector to a 2 cm diameter lens, which collects the light and images the speckle pattern to the 3 mm diameter silicon photodiode. The optical path length is 2 × 10 cm.

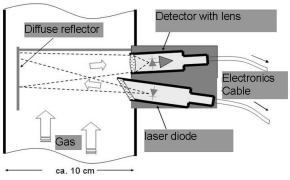

(b) Schematic plot of the diffuse reflector based optical cell [133] of the oxygen sensor. The reflections between laser and window with Brewster angle causes etalon with a FSR of 10 GHz. This is because the laser beam has a divergence (FWHM: 15 degrees). The light, that does not fulfill the Brewster condition, will give rise to a parasitic etalon .

Fig. 7.3: The photograph and schematic figure of the optic cell of oxygen sensor

7.2.3 Design of spectral evaluation algorithm

The O_2 A-band [134] (Fig. 7.4) at 763 nm consists of isolated lines, which do not interfere with species present in the exhaust gas in significant amounts, like H_2O, CO_2, CO, NO_x [10]. The band corresponds to an magnetic dipole electronic transition with rotational fine structure [10]. The gas absorption line at ambient pressure has a Voigt profile with dominating Lorentzian halfwidth (pressure broadening) of ∼92 % of the Voigt halfwidth, in the range of room temperature to 170 degrees (temperature range in the exhaust of a gas furnace). Therefore, computation of line shape is simplified by assuming a Lorentzian-based gas absorption line profile and the error caused by neglecting the Gaussian broadening is accepted. Then the isolated single-line model developed in section 6.2.1 can be applied. The VCSEL is tuned by current (Fig. 7.2), which consists of a linear ramp signal superimposed with a f_m = 6 kHz sinusoidal modulation. The measurement rate R^1 of one spectrum and gas concentration value is 5 Hz. The signal processing and control are done by a compact microcontroller-based electronics (board dimensions: 10 cm × 6 cm).

[1] measurement rate is 1/(time span between two ramps)

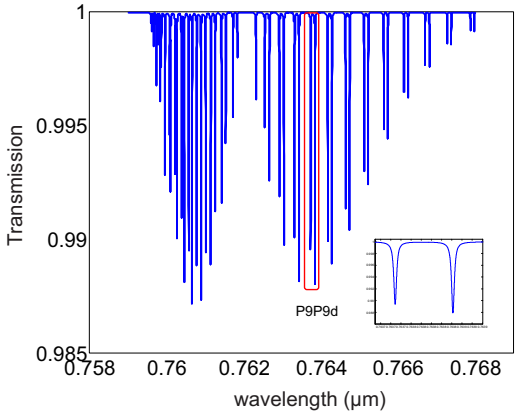

Fig. 7.4: Calculated absorption band spectrum of oxygen at 760 nm. The parameters are $c\,l = 5$ vol% $\times 0.2$ m, $p = 1$ Bar, $T = 296$ K.

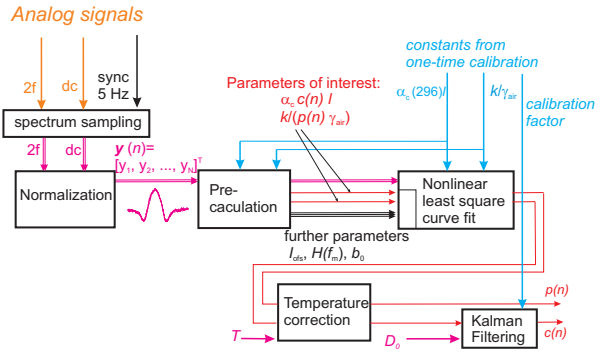

Fig. 7.5: Block diagram of signal processing chain for spectral evaluation: data recording, signal normalization, pre-calculation (section 6.2.1), nonlinear least-square curve fit, temperature correction and Kalman filtering.

The task of signal processing is to extract the gas concentration and pressure from the recorded gas spectra, which is described with the following steps (Fig. 7.5): data recording, signal normalization, pre-calculation, nonlinear least-square curve fit, temperature correction and Kalman filtering. With initial values given by the heuristic estimation method (section 6.2.1) only one to three iterations of the Levenberg-Marquardt fitting routine [112] are required to obtain a good fit to the model given in Eq. (6.42). The Levenberg-Marquardt algorithm requires the knowledge of the Jacobian matrix, which contains the derivatives of the model function with respect to each parameter [117]. To save computing time and capacity in the microcontroller, the Jacobian matrix is programmed analytically instead of estimating it numerically, which reduces the operating time by a factor of at least of two.

After the nonlinear curve fit, a temperature correction based on the signal of an additional temperature sensor and according to theoretical calculations is carried out to the concentration and/or pressure value (section 6.2).

After the curve fitting, time-variant noise is still superimposed on the concentration values. To separate the system noise from the real concentration variation, time-variant Kalman filtering is applied (section 6.4).

7.2.4 Sensor performance: O_2 concentration and gas pressure measurement

The sensor was mounted in the exhaust pipe of a wall-hanging condensing gas boiler with 10-20 kW heat power. The oxygen concentration was measured when the gas furnace was switched on and off for several times which is comparable to real operation. During first switching on, the photo detector current decreases by a factor of ∼3 due to condensing on the optical surfaces (Fig. 7.6(a)). Contamination on optic surfaces

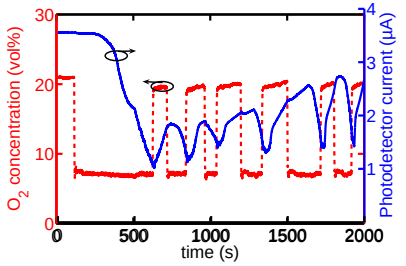

(a) The estimated concentration value during burner on/off switching. The photodetector current decreases by a factor of ∼3 due to condensation in this measurement. A decrease of factor 5 is observed on a longer time scale (Tab. 5.1).

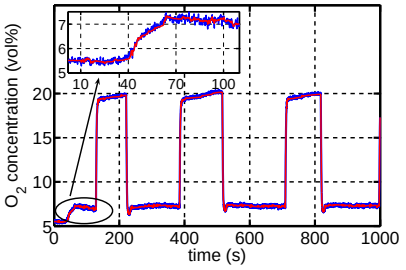

(b) The measured O_2 concentration (blue) and filtered result (solid curve) with Kalman filter (dashed curve). Unlike conventional lowpass filter, no detection delay is introduced additionally by the Kalman filter compared to the unfiltered sensor data.

Fig. 7.6: Concentration measurement results with the oxygen sensor

turned out to be no issue in a gas furnace because of the high purity of the natural gas used for combustion. Reference measurements with electrochemical cell and lambda probe were carried out by Siemens Building Technology, compared to which, TDLS-based sensor shows a faster response time [70]. The fitting result is shown in Fig. 7.7.

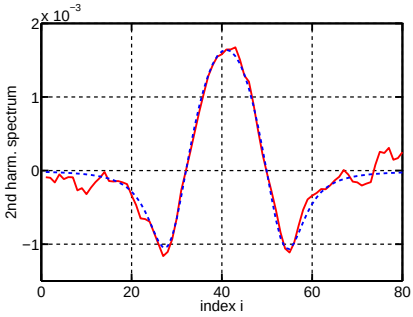

Fig. 7.7: Measured second harmonic spectrum (red, solid curve) of oxygen at 763 nm and its minimal mean square curve fit with the model (Eq. (6.42)) (dashed curve). The tuning range approximately 60 pm (tuning current ∼100 μA). The detected photodetector power is 500 nW and the power of detected second harmonic is about 500 pW. The O_2 concentration is about 4 vol%.

The received detector power in this case is 500 nW and the detected power of second harmonic component is 500 pW. The fit guarantees long term stability of the sensor. The standard deviation of the measurement i.e. the O_2 concentration uncertainty during boiler operation for one constant concentration value is 930 ppm (1σ in 5 Hz) without Kalman filter. For 1 Hz measurement, this value is converted to 417 ppm by dividing by $\sqrt{5}$, which corresponds to an absorbance resolution of $a_{res} = 1.1 \times 10^{-5}$. With the utilization of Kalman filter, 250 ppm standard deviation with 5 Hz is achieved (Fig. 7.6(b)). Additional to four times improvement of sensing sensitivity, no additional detection delay is introduced by the Kalman filter compared to the unfiltered sensor data, which is very important for measurements in a furnace, where fast control loops are needed. For determination of the sensor noise $\sigma^2(w(k))$ Eq. (6.40) was used. There, however, S_{yy} is higher than theoretically predicted in Eq. (6.34) as experimentally identified in Fig. 7.8. A factor of ~ 1.6 deviation is observed.Therefore, a one-time calibration for sensor noise $\sigma^2(w(k))$ is done and considered in the Kalman filter algorithm.

The consistence of the noise measurement in furnace and laboratory (Fig. 7.8) is again a confirmation that the condensation caused intensity noise has no influence on the measurement.

The developed theory for the sensor sensitivity $\sigma(\widehat{c})$ in Eq. (6.40) reads:

$$\sigma(\widehat{c}) = \frac{1}{\alpha_c\, l} \sqrt{(\mathbf{\Psi}^T \mathbf{\Psi})^{-1}_{11}\, N}\, \sqrt{S_{yy}\, R} \tag{7.2}$$

Since the employed curve fit is nonlinear, prior to the application of the formula the model has to be linearized. Then an observation factor $\sqrt{(\mathbf{\Psi}^T \mathbf{\Psi})^{-1}_{11}\, N} = 7.0$ is obtained. By applying the oxygen line strength from HITRAN database [10] ($\alpha_c = 0.00130$ cm^{-1}) and $S_{yy} = 2 \times 10^{-13}$ Hz^{-1} (see Fig. 6.6, for 3 μW detector power), $\sigma(\widehat{c}) \approx 120$ ppm is obtained for measurement repetition rate R of 1 Hz. The deviation between theory and experiment is a factor of 3.5. This is partly attributed to the noise given by the electronics. In an experiment with a recently developed improved

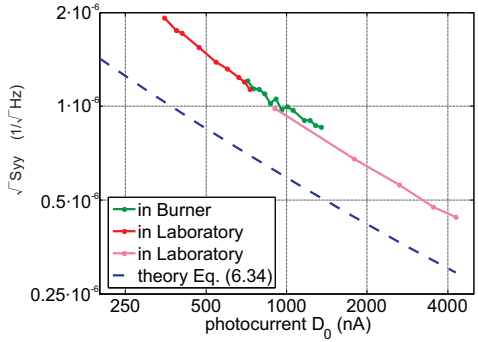

Fig. 7.8: Measured noise density $\sqrt{S_{yy}}$ in laboratory, gas furnace and theoretical value in doubly logarithmic scale. A factor ~ 1.6 deviation to theory is observed. It can further been seen, that condensation caused intensity noise has low/no influence on the measurements. Differing to the other measurements a laser with RIN $= -140$ dBc was used.

electronic, the standard deviation of the oxygen measurement is 283 ppm @ 1 Hz. The electronics uses digital transmitter stage as compared to the old fully analog design, which probably explains the better performance.

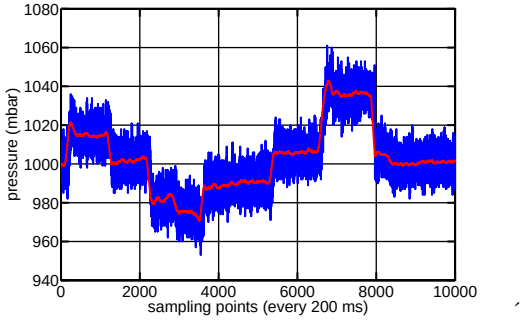

Fig. 7.9: Laboratory pressure measurement in every 200 ms (blue) and the 20 s average (red). The pressure values were set manually to 1000, 1030, 1000, 970, 962, 973, 1000, 1049 and 1000 mbar. The measurement is done with 100 % oxygen and at ambient room temperature.

The utilization of the theoretical formula thus allows for an easy judgment of the overall sensor realization and may help in identification of further design improvements. However, even with the new electronics the performance is still a factor of 2.2 worse than the theory predicts. This residual difference may be caused by the cell background, which is 10^{-5} in absorbance (Fig. 5.7) or the nonlinear curvefit.

The laser spectroscopic overall gas pressure measurement is shown in Fig. 7.9, wherein a non-linear response of the sensor to pressure values is observed. The devi-

ation was traced back to the following reasons: the assumption of a Lorentzian-based absorption line profile is probably too approximate for a pressure determination with high precision; furthermore, the laser residual amplitude modulation (RAM) influence [15] on the spectrum is only considered as an offset in the curve fit. Nevertheless, the pressure output values are reproducible, so a nonlinear correction can be done if gas pressure is to be estimated. The standard deviation of the estimated pressure measurement is 6 mbar at 5 Hz measurement rate. After nonlinear correction, the standard deviation would be approximately 9 mbar.

In Tab. 7.1, summary of laser parameters and characteristics of the O_2 sensor is shown.

Laser	Type	763 nm GaAs-based VCSEL
	Current	$I_0 \approx 4$ mA, $I_a \approx 80\mu$A
Cell	Type	diffuse, double-pass
	Length	20 cm
Signal-Processing	Type	single-line model
	Recording	$N = 64$ spectral points in 200 ms
	Algorithm	heuristic + nonlinear fitting + Kalman filter
	Line Locking	tracking of O_2 line
Performance	Time res.	5 Hz
	Conc. res.	250 ppm
	Pressure res.	6 mbar

Tab. 7.1: Summary of the parameters and characteristics of the O_2 sensor.

7.3 Calibration-free carbon monoxide sensor

Carbon monoxide (CO) is a toxic gas, which affects human health whenever present in the ambient air. CO escaping from home burners is the most frequent cause for unintentional death at home with a death toll of annually 400 persons in the USA [135]. Moreover, it is the most prominent gas to be detected for gas sensor based fire detection [136]. The requirements for such sensors are compactness, long term stability, high sensitivity (ppm range) and selectivity, and highest possible reliability. Applying the recently developed 2.3 μm VCSEL [7, 20], an absorption line in the first-overtone band of CO is sampled, which is approximately 160 times stronger than its second overtone band at 1.5 μm.

Diverse CO measurements were carried out by different groups either at environmental condition [137, 138] or in combustion [125, 139, 140] applying TDLAS using edge-emitting laser diodes. However, the measurement configurations are rather complex. Since the tuning range of DFB lasers at 2.3 μm (<2.1 nm) is too small to cover adjacent absorption lines for wavelength scale identification, traditional line locking or reference etalon has to be utilized (Fig. 6.2(a)). In this section, a light-weight and small sensor concept (optical cell: ≈ 7 cm overall extent feasible) capable of CO detection in ppm range with 1 Hz bandwidth is presented (Fig. 7.10). It utilizes the wide tuning capability of VCSELs. No separate gas reference cell was used. It marks an important technological step in CO sensing providing a reliable, cost-efficient and mobile solution for toxic gas monitoring.

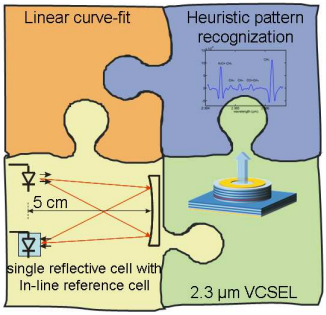

Fig. 7.10: The components of the carbon monoxide sensor: spherical-mirror based single-reflective cell with in-line reference cell, 2.3 μm InP-based VCSEL, multi-line model with heuristic pattern recognition (sec. 6.2.2) and linear curve fit (section 6.1.3).

7.3.1 Design of sensor optics

Because CO is a trace gas, the measured gas absorption spectrum in ambient air gives no indication of the CO absorption line position. Furthermore, the VCSEL current to wavelength relationship and its dependency on modulation frequency are not exactly known and can not assumed to be constant for long-term stable sensor operation. The nonlinear current to wavelength tuning behavior may change when the laser ages. Therefore, the laser current used to scan the CO absorption line can not be determined a priori even though the wavelength position of the absorption line is known from the HITRAN database [10]. Therefore, the concept of wavelength identification with in-line reference cell containing methane (section 6.2.2) is utilized.

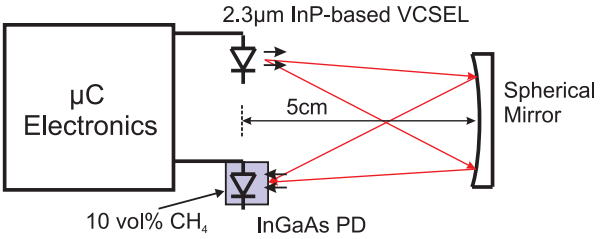

Fig. 7.11: Schematic design of the CO sensor: a compact absorption cell with 2×5 cm optical path length (reflective geometry) is used in combination with microprocessor controlled electronics (board dimensions: 10 cm×10 cm). 10 vol% reference gas (CH_4) is filled in the photodetector housing and therefore directly integrated in the measurement optical path.

To accomplish a defined methane absorbance of 2.5×10^{-3}, a reference gas containing 10 % CH_4 is included in the cap of the photodetector forming an optical absorption path of about 0.6 mm. Since methane is not the target gas, limited outdiffusion during the lifetime of the methane does not affect the lower detection limit of CO.

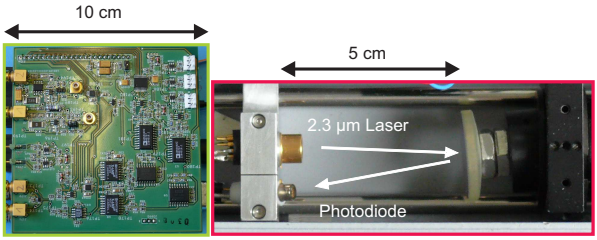

Fig. 7.12: Photograph of the absorption cell and the microprocessor controlled electronics of the CO sensor.

Moreover, leaking of methane can be detected in the wide spectrum scan. Recently developed 2.3 μm InP-based VCSELs [7, 141] with a current tuning coefficient of around 1.1 nm/mA (2.0 cm^{-1}/mA) were used in this sensor. Single-mode GaSb-based VCSELs at 2.3 μm [58] could be alternatively used. A spherical mirror based cell is applied because there is no requirement for harsh condition for the CO sensor. It could be easily replaced by a diffuse reflector. The laser can has no window and the photodiode is tilted to avoid fringes. A compact, microcontroller-based electronics (board dimensions: 10 cm $\times$ 10 cm) serves as sensor control, signal processing and data evaluation. The current of the laser device is tuned periodically to scan the absorption spectrum and the temperature of the laser chip is kept constant by a controlled thermoelectric cooler (TEC).

7.3.2 Design of spectral evaluation algorithm: wide/narrow scan

Because of the large current to wavelength tuning range of the VCSEL, a broad wavelength range can be scanned to cover the strong adjacent methane absorption lines from the reference gas in the detector housing. These are used to identify the wavelength scale, so that the required laser current for the CO line wavelength position is known exactly. For the wavelength scale identification, the heuristic pattern recognition is applied introduced in section 6.2.2 is applied. The wide scan covers about 3 nm every 6 seconds. A typical wavelength shift is shown in Fig. 6.11 (40 pm in 25 min).

More frequent narrow scans covering 0.7 nm around the absorption line P8 of the first overtone vibrational band of CO at 2.3 μm are performed to determine the CO concentration using a linear least-squares curve fit. The narrow scan is repeated every 0.1 s, so the measurement rate is $R = 10$ Hz.

The measured second harmonic spectrum $\mathbf{y} = (y_1, ..., y_N)^T$ (Fig. 7.13(b)) consists of $N = 64$ samples and is linearly composed by four components (Fig. 7.14): second harmonic spectrum of CO, second harmonic spectrum of CH_4, a slope and an offset. The signal model described in section 6.1.3 (Eq. (6.35)) is utilized with the extension to an additional interfering gas. An offset and a slope in the second harmonic spectrum is caused by the second and third order polynomial components of the laser P-I curve [15].

The wide scan could be in principle utilized both for the identification of the wavelength scale, and also for the determination of the gas concentration value. In that case, however, the noise on the estimated CO concentration is not minimized. This is shown by the developed theory (section 6.3) for optimum wavelength scanning: there is

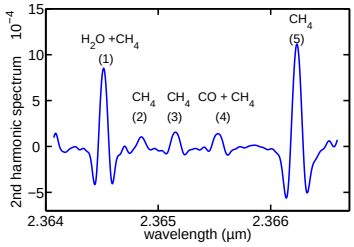

(a) Wide scan (duration: 640 ms, 512 samples): measured second harmonic spectrum of CO and CH_4 absorption lines. The wavelength scale is determined by the known wavelength positions of the two strong methane lines (1), (2) and either (3) or (4), depending on which line is larger. The heuristic pattern recognition method is introduced in section 6.2.2

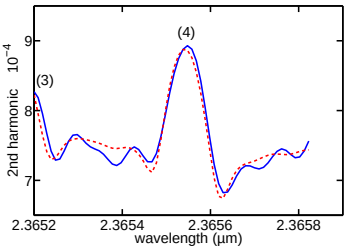

(b) Narrow scan (scan duration: 100 ms, 64 samples): second harmonic spectrum of CO and CH_4 absorption lines (solid curve), and the analytically computed and fitted reference curve (dashed curve) using the model basically described by Eq. (6.35) for a spectrum scan of 0.7 nm via current. The wavelength scale was determined before in the wide-scan. The CO absorption corresponds to 10 ppm m (c = 100 ppm, l = 10 cm).

Fig. 7.13: The wide and narrow spectral scan

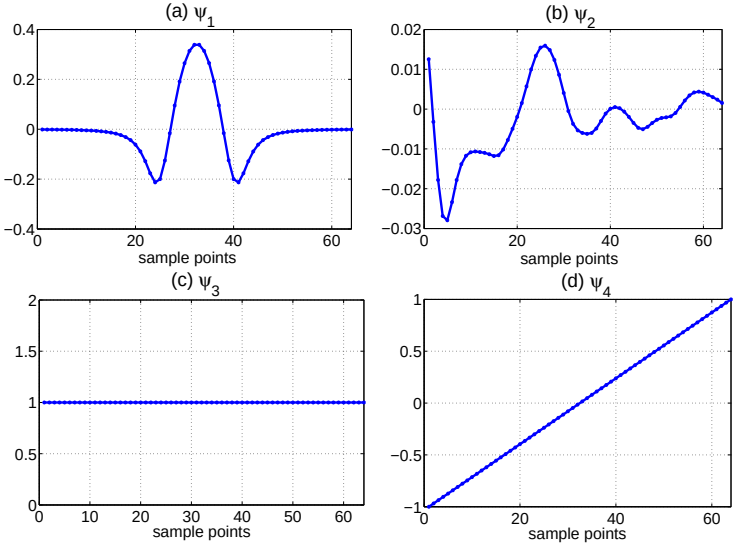

Fig. 7.14: The components of the model for curve fitting: (a) ψ_1, the second harmonic spectrum of CO at 2.365 nm with (b) interfering gas methane ψ_2 (second harmonic spectrum of 20 methane lines) (c) ψ_3 (offset) and (d) ψ_4 (slope) are the spectral baseline caused by the second and third order polynomial components of the laser P-I curve.

was concluded that also for linear scanning an optimum scan width exists. For this the observation factor $\sqrt{(\Psi^T\Psi)^{-1}\,N}$ is minimized by changing the scanwidth. It turned out, that a scanning width of 9 times HWHM is optimum (Fig. 6.13). Scanning of a too broad range is thus not optimal because the information content of the CO absorption line in the outside range is low. Scanning of a too small spectral range dismisses the information of baseline, so that the simultaneous estimation of c and baseline b_0 and b_1 becomes difficult.

For the CO concentration determination using the wide and narrow scan concept, neither background measurement nor reference spectra measurements nor further calibration factors except for the line parameters from the HITRAN database and the gain of the second harmonic signal path of the sensor electronics are required. With this method a lifetime-stable self-calibration is within reach. This analytical approach reduces the enormous complexity of storage of measured reference spectra, especially if temperature dependence of spectra is involved, which is easily included in the analytical model.

7.3.3 Sensor performance and application results

The sensor was characterized with an Allan variance plot and tested for fire detection as well as for combustion optimization in the exhaust gas pipe of a gas furnace.

Laser	Type	2365 nm InP-based VCSEL
	Current	$I_0 = 7.5$-10 mA, $I_a \approx 120$ μA
Cell	Type	spherical, double-pass
	Length	10 cm
Signal-Processing	Type	multi-line model
	Recording	$N = 64$ spectral points (1 ms each)
	Algorithm	heuristic pattern recognition + linear fitting
	Line Locking	tracking of CH_4 lines
Performance	Time res.	10 Hz
	Conc. res.	2 ppm

Tab. 7.2: Summary of the parameters and characteristics of the CO sensor.

Allan plot

Under controlled gas temperature ($T = 30$ °C) and gas pressure ($p = 960$ mbar), a one-day measurement was carried out to characterize the system performance. By averaging the CO concentration, the standard deviation decreases and the standard deviation is 2 ppm with 1 s time resolution. This corresponds to an absorbance resolution of $a_{res} = 1 \times 10^{-5}$. A calculation for the theoretical resolution is done, utilizing the formula for sensing sensitivity (Eq. (6.40)):

$$\sigma(\widehat{c}) = \frac{1}{\alpha_c\, l}\,\sqrt{(\mathbf{\Psi}^T\mathbf{\Psi})^{-1}_{11}\,N}\,\sqrt{S_{yy}\,R} \tag{7.3}$$

Inserting the value $\sqrt{(\mathbf{\Psi}^T\mathbf{\Psi})^{-1}_{11}\,N} = 7.6$ for linear scanning with scanning width of 12 HWHM applied in model III (Tab. 6.5), and $S_{yy} = \mathrm{RIN} = 10^{-13}$ Hz^{-1}, $R = 10$ Hz, $\alpha_c = 3.5714 \times 10^{-5}$ ppm m^{-1} and $l = 10$ cm, the theoretical sensing resolution is 2.1 ppm, which agrees very well with the experiment.

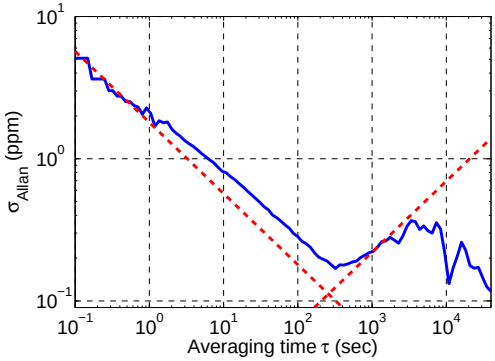

Fig. 7.15: The measured Allan standard deviation σ_{allan} as a function of the averaging time τ (solid line). It consists of two components: τ^{-1} and τ^1 (dashed lines), which indicate the existence of the white noise and Brownian noise ($1/f^2$ noise), respectively.

The Allan variance plot [142] is shown in Fig. 7.15, which can be divided into two parts: τ^{-1} and τ^1, the latter term indicate the existence of the Brownian noise ($1/f^2$ noise) [143]. The optimum integration time τ_{opt}, where the Allan variance curve is minimum, is approximately 300 s.

It is not clear what the cause of the observed drift is, which leads to a rise of σ_{allan} with averaging time τ. It could be an instability in the optical cell, which can be handled by improving the optical set up. Alternatively, the accuracy of the wavelength stabilization may be still too low. Since the repetition rate of the wavelength stabilization of 6 s is far below the time constant of the wavelength drift (see Fig. 6.11), averaging will substantially enhance the wavelength scale accuracy. Furthermore, background instabilities of the first available sample lasers may also have some impact on the observed drift.

Fire detection and exhaust gas monitoring

To carry out fire detection tests according to the European Standard EN 54 [145], an extractive set-up was used. The extraction inlet is mounted at the ceiling of a test room on a 3 m radius circle around the test fire and the gas is fed via a 15 mm diameter and 10 m long plastic tube with a flow rate of several liter pro minute to the detector. The end of each individual fire by purging the room is visible in Fig. 7.16(a) as a steep decrease in CO concentration. Since the room has a very high volume (∼228 m^3), the CO concentration stays below 120 ppm for the wood fire and the pyrolysis ('smoldering', e.g. wood on a hot plate). Smouldering is a very incomplete burning with no flame and very high CO generation (up to vol % range). Therefore, the CO concentration at Smouldering increases much faster than the CO concentration produced by the wood fire. In case of open fires like n-heptane (Fig. 7.16(a)), much less CO is generated. These kinds of fires are also typically more difficult ones to detect for smoke detectors, due to less particle generation.

CO measurement in the exhaust gas of gas furnaces is relevant for the optimization

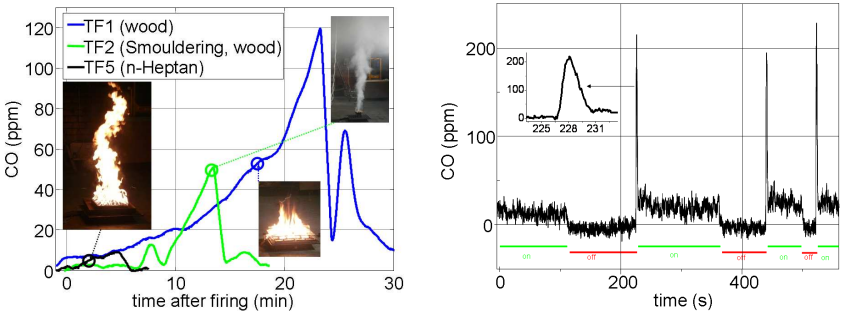

(a) Measurement results of different test fires (TF) with one minute integration time. All of the fires are detected via an increase of the CO concentration. The steep concentration drop results from the ventilation of the room. (Details in paper [144])

(b) A CO measurement in exhaust gas of a gas furnace: the burner is turned on and off frequently simulating the real operating condition. The CO peak could be measured in this application because of the very fast time resolution of 100 ms.

Fig. 7.16: Test results of the CO sensor

of the burning process. Usually detection of CO in the 10 ppm range is requested. When the furnace is turned on, a CO concentration peak occurs for approximately 2 s full-width at half-maximum (Fig. 7.16(b)), which demonstrates the advantage of the high time resolution of the CO sensor.

7.4 Fiber-based carbon monoxide sensor

Utilizing a single-reflective cell with only 10 cm optical path length, a sensor resolution of 3 ppm (1σ @ 1 Hz) is already achieved at 2.3 μm (section 7.3.3). Using a 3 m hollow fiber, an additional sensitivity improvement of a factor of 30 is expected. Possible applications are more sensitive fire detection, industrial process monitoring and breath analysis, where sensitive measurements are needed.

7.4.1 Design of sensor optical cell

In Fig. 7.18(a) the design of the fiber-based CO sensor is shown. Due to the low divergence of the VCSEL light emission (FWHM: 10-20 degrees), direct in- and outcoupling to the fiber (measured FWHM: ~10 degrees) could be employed. This enabled a robust and miniaturized sensor design, because possible optical interferences caused by parallel optical surfaces are eliminated. In contrast to multi-pass cells almost no optical alignments have to be made. In-line reference cell concept is also employed here, the wavelength scale is calibrated inherently without a need of an external reference cell.

A 200 Hz vibration is employed to the fiber end used for incoupling with an optimized vibration amplitude (Δr in the range of several 100 μm). As mentioned in section 5.7.4, the smoothing effect of vibration does not depend on the vibration frequency, as long as it is higher than cutoff frequency of system filters e.g. analog lowpass filter or curvefit. 200 Hz is therefore sufficient for 10 Hz concentration measurement rate and it can

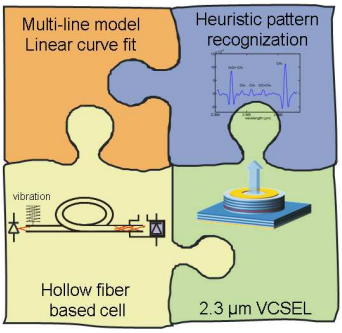

Fig. 7.17: The components of the carbon monoxide sensor: 3 m hollow capillary fiber (section 5.7), InP-based 2.3 μm VCSEL, multi-line model with heuristic pattern recognition (section 6.2.2) and linear curve fit (section 6.1.3).

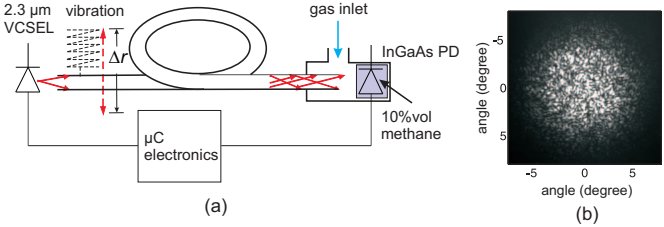

Fig. 7.18: (a) Experimental setup of the fiber sensor. Mechanical vibration is employed to the fiber at the incoupling end. A reference gas (10 vol% CH_4) is filled in the photodetector housing, which forms an integrated reference cell. A compact, microcontroller-based electronics serve as sensor control, signal processing and data evaluation. (b) Farfield of the fiber. A speckle pattern is observed indicating highly multi-mode propagation of the light. The full-width half-maximum of the far field emission is around 9°.

probably be chosen even lower.

Laser	Type Current	2365 nm InP-based VCSEL $I_0 \approx 7.5$-10 mA, $I_a \approx 120$ μA
Cell	Type Length	hollow fiber based cell 3 m
Signal-Processing	Type Recording Algorithm Line Locking	multi-line model $N = 64$ spectral points (1 ms each) heuristic pattern recognition + linear fitting tracking of CH_4 lines
Performance	Time res. Conc. res.	10 Hz 180 ppb

Tab. 7.3: Summary of the parameters and characteristics of the fiber-based CO sensor.

7.4.2 Sensor performance and application results

Allan plot and comparison with theoretically expected performance

The Allan plot for the fiber sensor (3 m fiber length) is shown in Fig. 7.19. A 180 ppb

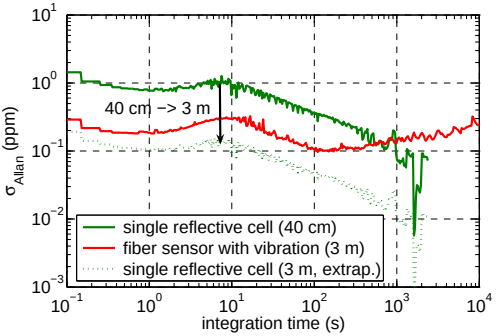

Fig. 7.19: Allan variance σ_{allan} [142] versus the sensor integration time is shown for the fiber sensor with 3 m optical path length (red curve). For comparison, the Allan plot of the 40 cm single-reflective cell based sensor (green curve) as well as the extrapolated performance of 3 m single-reflective cell based sensor (green dotted curve) are shown as well.

concentration resolution (1σ) was obtained for 1 s averaging time. For comparison, the sensor with a single-reflective cell (using the same laser and photodiode, 40 cm optical path length) was also characterized and the expected performance of a 3 m single-reflective cell is extrapolated by scaling with the path length ratio (Fig. 7.19). In contrast to single-reflective cell, a drift of the fiber sensor is indicated by the increase of the Allan standard deviation σ_{Allan} above 100 s. Therefore, the drift must be caused by the fiber itself or the mechanical vibration. The optimal integration time of the fiber sensor is given by the position of minimum (approx. 100 s). At this point, the resolution of fiber sensor is two fold worse compared to the extrapolated performance of single-

reflective cell based sensor (section 7.3). It is possibly due to additional mechanical noise given by vibration.

Utilizing the formula for sensing sensitivity Eq. (6.40):

$$\sigma(\widehat{c}) = \frac{1}{\alpha_c\, l}\sqrt{(\mathbf{\Psi}^T\mathbf{\Psi})^{-1}_{11}\, N}\,\sqrt{S_{yy}\, R} \tag{7.4}$$

Inserting the value $\sqrt{(\mathbf{\Psi}^T\mathbf{\Psi})^{-1}_{11}\, N} = 7.6$ for linear scanning with scanning width of 12 HWHM applied in model III (Tab. 6.5), and $S_{yy} = \text{RIN} = 10^{-13}$ Hz^{-1}, $R = 10$ Hz, $\alpha_c = 3.5714 \times 10^{-5}$ ppm m^{-1} for CO absorption line at ambient temperature, $l = 3$ m, the theoretical sensing resolution is 70 ppb, which is two times lower than the measured value. Recalling, that the experimental and theoretical values for the spherical mirror based CO sensor agree very well, it is concluded that the inconsistence comes probably from the noise introduced by the mechanical vibration.

Breath analysis test

The sensor was tested by measuring the exhalation of a smoker. The cigarette smoke contains high concentration of carbon monoxide, which is very easily taken up by the blood. The affinity of hemoglobin to carbon monoxide is approx. 200 times higher than to oxygen. Exhalation of a smoker was sampled into the fiber, where a CO

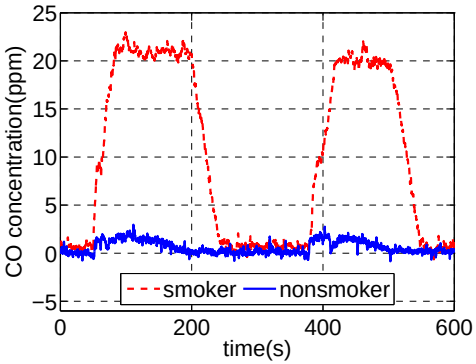

Fig. 7.20: Measured carbon monoxide concentration in the exhaled air of a smoker (red dashed curve) and non-smoker (blue solid curve) in 1 s time resolution. Each measurement consists of 1) sampling of exhalation into the fiber 2) keeping the gas in the fiber 3) purging with nitrogen.

concentration of 20 ppm is measured (Fig. 7.20). For comparison, the exhalation of a non-smoker was sampled as well indicating a concentration of below 2 ppm in the exhalation. The result is consistent with another study of over 100000 people in the EU [146]: carbon monoxide concentration in exhalation rises by 1-2 ppm per cigarette per day, whereas an average CO concentration of a non-smoker is 1-2 ppm.

7.5 Conclusion

An oxygen sensor for combustion optimization in gas furnaces was developed, the measurement was realized in the exhaust gas pipe of gas furnace. Utilizing a diffuse reflector based cell, the problem of possible misalignment of the optics due to thermal cycles, the condensation problem on optic surfaces and the problem of etalon fringes is solved. A real-time least-squares curve fit algorithm is presented, which improves the long term stability of the sensor compared to conventionally-utilized fixed detection at the absorption line center [97], because the baseline drift is taken into account. Real-time operation with a microcontroller is assured by determining good initial values using characteristic values of the second harmonic spectra (less iterations) and by programming the Jacobian matrix analytically (less computing complexity). There the maximum to minimum ratio R of the second harmonic curve is a very important characteristic value, it fully represents the curve shape, whereas the gas concentration is only a y-scale factor of the curve once the curve shape is fixed. Neither absolute wavelength scale, nor absolute wavelength difference between two measurement points are needed for a concentration determination. Kalman filtering improves the detection sensitivity with factor of four at $R = 5$ Hz, without losing the reliability and the time response of the sensor operation. Both concentration and pressure measurements are carried out in the gas furnace and the detection limit of concentration is 250 ppm in 5 Hz measurement rate. The sensing resolution can be however improved by reducing the electronic noise to further lower S_{yy}. The diffuse reflector-based optical cell and the signal processing method described above are not limited to oxygen sensing, but can be applied also for the sensing of other gas molecules.

A compact and calibration-free carbon monoxide sensor approach utilizing the wide current-tunability of 2.3 μm VCSELs is reported. A separate reference cell is avoided by filling the photodetector housing with a reference gas (methane). By applying a bandwidth optimized wide/narrow wavelength scan concept, inherent wavelength scale calibration and self-monitoring of the sensor are realized, with which the laser aging process is also under control. An efficient linear least-squares curve fit using an analytic signal model in the narrow spectrum scan is done, utilizing knowledge of the absolute wavelength scale, and the estimated WMS modulation amplitude obtained from the wide scan. The scan width of the narrow spectrum is optimized aiming at the maximum signal to noise ratio on the determined CO concentration. The sensor was tested under diverse applications e.g. fire detection and combustion optimization. The concepts allow for the realization of compact gas sensors and demonstrate how the specific properties of VCSELs can be used to improve laser optical gas sensors. Neither background measurement nor reference spectra measurements nor further calibration factors except for the line parameters from the HITRAN database are required.

As a further improvement to the CO sensor, a fiber-based low volume and low level optical carbon monoxide sensor (1σ: 180 ppb @ 1 Hz) was developed. The utilization of a surface-emitting laser directly coupled to a hollow capillary fiber as gas cell, is proven to be a compact, sensitive and cost-efficient gas sensing concept, which is demonstrated for the first time. By applying vibration to the fiber with a moderate frequency of 200 Hz and an amplitude of several 100 μm, the fiber transmission function becomes smooth, so that absorbance in the order of 10^{-5} is resolvable with the sensor, which is comparable to conventional cells. Compared to a single-reflective cell based sensor (section 7.3.3), the fiber sensor has a 16 fold improvement in concentration resolution with a 30 times enhancement of the optical pathlength, while the needed sample volume is simultaneously lowered by several orders of magnitude to 1.3 ml. This

clearly demonstrates the potential of laser spectroscopic hollow capillary fiber based sensors. An additional several fold sensitivity improvement is expected using longer fibers, for which no technical difficulty is anticipated.

The sensing resolutions of all three sensors demonstrated are compared with the theory given in Eq. (6.40), using the observation factor $\sqrt{(\mathbf{\Psi}^T\mathbf{\Psi})^{-1}_{11}\,N}$ values given in Tab. 6.5. For the oxygen sensor the sensing resolution is 3.5 times worse than the theoretical value. The deviation is partly due to the noise caused by the analog electronics proved by the experiment with an improved electronic. In contrast, the theory shows good agreement with the experiments for CO sensor with single-reflective cell, which is also based on the new electronic. Apparently, the additional noise given by the analog electronics does not exist for the improved digital electronics. The sensor performance has reached the theoretical value and can be only improved by nonlinear scanning (section 6.3) and/or Kalman-filtering (section 6.4) and/or the use of direct spectroscopy. The fiber-based CO sensor using vibration exhibits 2 times lower sensing resolution than the theory, which is probably given by the distortion of vibration.

8 Conclusion and Outlook

The main achievements of this thesis are here discussed. Firstly the results of general nature are itemized:

- The FM response of VCSELs shows a square root law behavior (section 4.2.2), which is caused by the infinitely thin heat generation, i.e. the two-dimensional heat conduction in a three-dimensional space. A closed analytical expression for the FM response was found (Eq. (4.12)), derived from a simplified analytical thermal model (section 4.2.3). Here also an accurate method for the FM response using a gas absorption line is developed (section 4.2.1).

- The spectral background of a hollow capillary fiber is inversely proportional to the number of the speckle points integrated by the photodiode, both spatially and over time. Therefore, the novel concept for a low-background in-fiber based cell was discovered: namely the close placing of photodiode to fiber end, and the mechanical vibration at fiber incoupling. For the vibration it was found that there is an optimal vibration amplitude, but vibration frequency turned out not to be critical, as long as it is higher than the spectral scan rate (section 5.7).

- A formula for prediction of sensor noise was found (Eq. (6.40)), which also agrees with experiments. For this, the newly defined 'observation factor' describes the influence of the shape of the recorded spectra on the sensor noise. Not only a closed form expression for this factor is given, but also explicit values for different spectral models and spectroscopic methods are shown. Using this factor, the optimum method for sampling the spectrum could be found. It shows that sampling at N different discrete spectral points for N unknown parameters is both necessary and also sufficient for minimum noise concentration determination. Furthermore, it gives which points are to be sampled and in which fraction of the total measuring time. As a special case, the optimized spectrum scan width for linear sweeping is also found, where theory again agrees well with experiments (section 6.3.1). Theoretically, direct spectroscopy is superior to second harmonic detection, because the concentration noise can be an additional factor of $\sim$2 lower (section 6.3). Using the formula for sensor noise, also the determination of signal variances is possible, which enables proper utilization of Kalman filtering (section 6.4).

Other results of general nature include the finding that single mode lasers could have kinks in the P-I-characteristic and generate a high spectral background in the measured harmonic spectrum. Two possible reasons for kinks on the laser P-I characteristic of the examined laser are excluded: mode flips and transversal mode rotation (section 4.3.2). Furthermore, a new figure of merit definition for gas cells, enables comparison of resolvable number of gas molecules (Tab. 5.1 and Chap. 5). A truly unexpected finding is that the supposed single mode photonic crystal fiber is not strictly single mode by observing a high spectral background of fiber (10^{-3}). It is caused by interfering of fundamental mode and several weak core modes (section 5.6). Speckle noise caused by the diffuse reflector is significantly lower than spectral background

caused by the laser, which is usually 10^{-5} (section 5.4.2). The intensity noise caused by condensation is found to have a lowpass first order characteristic with a cutoff frequency in Hz range (section 5.4.3).

Using the scientific results shown above, the following successes in applications and sensors are achieved:

- Development of an oxygen sensor for combustion optimization in gas furnaces, including a real-time least-squares curve fit algorithm with Kalman filtering. Demonstration of a diffuse reflector as a superior candidate for harsh conditions because of its low speckle noise, its robustness against thermal cycles and condensation (section 5.4 and section 7.2).

- Development of a fiber-based sensor for carbon monoxide in sub-ppm range (1 σ: 180 ppb) and compact size (10 cm $\times$ 10 cm) capable for detection of pico-Liter carbon monoxide at 2.3 μm (section 7.3). This corresponds to a minimum resolvable number of molecules in the order of 10^{12} (Tab. 5.1). The sensor has a low gas exchanging time, which is in the 100 ms range for a 3 m long fiber at a pressure difference of one bar according to a theoretical calculation (Fig. 5.18).

- Development of a VCSEL-suitable signal model for WMS (Eq. (6.30)) and heuristic methods for parameters extraction out of measured gas spectrum with low computing complexity (section 6.2, Fig. 6.8). Development of heuristic pattern recognition algorithms: identification of wavelength scale from measured spectra. For this, a non-target gas as reference gas is integrated in the photodiode for compact sensor designs and self-monitored operation. This is also a method for monitoring the laser aging process (section 6.2.2).

All these findings can be used for a multitude of gas sensing applications.

Outlook

Based on the knowledge discovered in this work, there appear to be several logical next steps:

For the oxygen sensor, line identification could be developed. Then the absorption line looked for can be identified, and the line parameters can be read from the HITRAN database. The one-time calibration would then no longer be necessary, or the laser selection for an appropriate wavelength could be less strict. The same concept with the diffuse reflector can also be utilized for detection of water vapor at 950 μm, where cost-efficient GaAs VCSELs are available, due to the widespread application of VCSEL mice. An application for this could be regulation of humidity in professional cooking appliances.

A crucial issue for application in the field which has not yet been completely solved, is the contamination problem. Heating of optical surfaces may be a possible solution for this contamination, and further investigation has to be carried out. Further applications such as flame-on monitoring in furnaces, may also be possible with TDLS-based O_2 sensors because of their fast response time and intrinsic self-checking capability. This would give the laser spectroscopic oxygen sensor an additional advantage, and partly compensate for the higher cost because the conventional flame-on monitoring within furnaces can be simplified.

The wide/narrow scan concept is universal and can also be used for sensing of other gases, for example NO/H_2O and CO_2/H_2O using VCSELs at 1.8 μm and 2.0 μm,

respectively. When the 2.7 μm GaSb VCSEL are realized, the concept could be also implemented with a highly compact air quality sensor with optical path length of 1 mm.

For the fiber sensor, first, the vibration unit has to be made small and compact. It could be implemented using piezos or inductors. Second, holes could be utilized in the fiber to enable a faster gas exchange time or distributed gas sensing. Furthermore, simulation of the wave propagation inside the fiber can be done to find out the reason for the residual spectral background. The influence of scattering at the fiber ends or inside the fiber, or mode-mixing, could be separated with possible suggestions for reduction of the background.

Abbreviations and Symbols

Abbreviations

HWHM	Half-width at half-maximum
FWHM	Full-width at half-maximum
UV	Ultra-violet
NIR	Near-infrared
MIR	Mid-infrared
WMS	Wavelength modulation spectroscopy
VCSEL	Vertical-cavity surface-emitting laser
DFB	Distributed feed-back
HITRAN	High resolution transmission (molecular absorption line database)
FSR	Free spectral range
HGW	Hollow glass waveguide
TLV	Threshold limit value (maximum allowed concentration in work-place environments)

Symbols

Name	*Unit*	*Definition*
a_{res}	1	absorbance resolution
$a_{res,cell}$	1	absorbance resolution due to cell background
$a_{res,laser}$	1	absorbance resolution due to laser background
$a_{res,noise}$	1	absorbance resolution due to noise
$A_{bg,cell}(\lambda)$	1	cell background ('one minus transmission')
b_0	1	offset of the spectral background
b_1	1/mA	slope of the spectral background
c	1 (or ppm)	gas concentration
$\widehat{c}$	1 (or ppm)	sensor output value of estimated gas concentration
C_{CO}	ppm	gas concentration of CO
$C_{\mathrm{CH_4}}$	ppm	gas concentration of methane
c_{res}	1 (or ppm)	concentration resolution
$\mathrm{cov}(\mathbf{y})$	-	covariance matrix of $\mathbf{y}$
d	1	VCSEL form factor
D	μm or m	distance between active region and heatsink of VCSEL or thickness of optical elements
D_n	A	n-th harmonic component of detector signal
$D_L(t)$	A	detector signal
E_L	J	lower state energy of a transition
f, f_m	Hz	modulation frequency
f_0	Hz	thermal frequency scale parameter

f_c	Hz	3 dB cutoff frequency
$F(z)$	1	correction function for zero crossings of the second-harmonic spectrum
h	Js or m	Planck constant or surface roughness of a diffuse surface
$H(f)$	1	laser FM response
$H_n(\nu)$,$H_n(\lambda)$	1	n-th harmonic transmission spectrum
$H_{n,bg,cell}(\lambda)$	1	cell background (n-th harmonic spectrum)
$H_{n,bg,speckle}(\lambda)$	1	cell background due to speckle noise (n-th harmonic spectrum)
$H_{n,gas}(\lambda)$	1	n-th harmonic spectrum of the gas
i	1	imaginary unit
I	mA or W	laser bias current or light intensity
$\mathbf{I}$	1	the identity matrix
I_a	mA	laser current modulation amplitude
I_{dark}	A	dark current of the photodetector
I_i	mA	laser bias current at the i-th spectral sample
I_{ofs}	mA	laser current that corresponds to the absorption line center
$\widehat{I_{ofs}}$	mA	estimated laser current that corresponds to the absorption line center
$I_L(t)$	mA	laser current signal
j	1	rotational quantum number
k	nm/mA	linear current tuning coefficient
k_2	nm/mA^2	quadratic current tuning coefficient
$K(k)$	1	Kalman gain at time step k
l	m	optical interaction path length
l_0	m	physical cell length
m	1 or kg	normalized modulation amplitude or reduced mass
$\widehat{m}$	1	estimated normalized modulation amplitude
M	1	number of unknown parameters
n	cm^{-3} or 1	molecule number density, refractive index, index of the n-th harmonic spectrum, order of lowpass or discrete time step
N	1	number of points per spectrum scan (dimension of ψ_i), number of speckle points or number of light spots
OPD	m	optical path length difference
p	bar	gas pressure
$\widehat{p}$	bar	sensor pressure output value
$P_n(I)$	W	n-th harmonic component of laser intensity modulation signal
$P_0(I)$	W	DC component of laser intensity
$P_L(t)$	W	laser intensity modulation signal
q_A	1	Burner efficiency
$Q(T)$	1	total internal partition sum for a molecule
r	A/W or m	detector responsivity or radius

R	Hz or 1	measurement rate or the max to min ratio of the second harmonic spectrum
R_0, R_1	μm	radius of current aperture and light mode
R_v	V/A	gain of the pre-amplifier
$S_n(x, m)$	1	n-th harmonic spectrum for Lorentzian line (Arndt's formula)
S_{yy}	1/Hz	the noise power density on $\mathbf{y}$
$T(\nu)$, T	1 or K	transmission spectrum or gas temperature
$T_{0,cell}$	1	empty cell attenuation factor
$T_{cell}(\lambda)$	1	the transmission spectrum of the empty gas cell
$T_g(x, y, z, t)$	K	transient thermal response (spatial)
$\overline{T}_g(t)$	K	transient thermal response (average temperature)
$\widehat{T}_g(f)$	K	thermal frequency response (average temperature)
$T_{gas}(\lambda)$	1	transmission spectrum of the gas
$\mathbf{u}$	various	vector of unknown parameters $\mathbf{u} = (u_1, \ldots, u_M)$
V	cm^3	cell volume
$v(k)$	1 (or ppm)	random process modeling the gas concentration fluctuation at time step k
$w(k)$	1 (or ppm)	random process modeling the sensor noise at time step k
x	1	normalized wavelength or independent variable in the signal model
$\mathbf{y}$	1	measured second harmonic spectrum vector $\mathbf{y} = (y_1, \ldots, y_N)$
$\alpha(\nu)$	cm^{-1}	absorption coefficient
α_c	cm^{-1}	absorption coefficient at absorption line center or peak absorption coefficient
β	nm/s	speed of spectral scanning
Δf	Hz	interference periodicity in frequency scale
Δr	cm	distance between laser and center of fiber cross-section
Δz	cm	distance between detector and fiber end
γ	cm^{-1}/bar	pressure broadening coefficient
γ_{air}	cm^{-1}/bar	pressure air-broadening coefficient
γ_{self}	cm^{-1}/bar	pressure self-broadening coefficient
γ_G	cm^{-1}	Doppler broadened linewidth (HWHM)
γ_L	cm^{-1}	pressure broadened linewidth (HWHM)
$\gamma_{L,nat}$	cm^{-1}	natural linewidth (HWHM)
γ_V	cm^{-1}	Voigt linewidth (HWHM)
ϵ	1	noise vector $\epsilon = (\epsilon_1, \ldots, \epsilon_N)$
ζ	1	exponent of temperature dependence for pressure broadening coefficient
θ	deg	far-field acceptance angle
κ	$\mathrm{s/cm}^2$	thermal diffusivity
λ	nm	wavelength
λ_0	nm	laser emission wavelength extrapolated to $I = 0$
λ_a	nm	laser wavelength modulation amplitude

λ_i	nm	laser emission wavelength at the i-th spectral sample
$\lambda_{i,opt}$	nm	laser emission wavelength at the i-th spectral sample for optimum spectral sampling
λ_m	nm	wavelength of the minimum of the second harmonic spectrum
λ_z	nm	distance of zero crossings of $H_2(\lambda)$
$\lambda(I)$	nm	laser bias wavelength at current I
$\lambda_L(t)$	nm	laser wavelength modulation signal
ν	cm^{-1} or 1	wavenumber or vibrational quantum number
ν_c, λ_c	cm^{-1}, nm	center wavenumber or wavelength of an absorption line
σ_0	ppm	normalization factor for the noise on the measured gas concentration $\sigma(\widehat{c})$
$\sigma(\nu)$, $\sigma(X)$	cm^2 or $[X]$	absorption cross-section at wavenumber ν or standard deviation of X
$\sigma(\widehat{c})$	1 (or ppm)	standard deviation of sensor output values
$\sigma(\widehat{c})_{opt}$	1 (or ppm)	standard deviation of sensor output values for optimum spectral sampling
τ	s	time constant, upper state lifetime or gas exchanging time
$\phi(f)$	rad	laser FM phase shift response
Φ	1	light power fraction in air
Φ_L,Φ_G,Φ_V	cm	Lorentzian, Gaussian and Voigt absorption line profile
$\Phi(\nu)$	cm	normalized absorption line profile
$\boldsymbol{\Psi}$	1	observation matrix (columns ψ_i), for linear model
ψ_i	1	spectral component vectors
$\psi_{i,opt}$	1	spectral component vectors for optimum spectral sampling
$\sqrt{(\boldsymbol{\Psi}^T\boldsymbol{\Psi})^{-1}_{11}N}$	1	'observation factor' for spectral scan

Bibliography

[1] E. Symons, *Gas Sensors* (Kluwer Academic Publishers, 1992), chap. Catalytic Gas Sensors, p. 169.

[2] C. Mari and G. Barbi, *Gas Sensors* (Kluwer Academic Publishers, 1992), chap. Electrochemical Gas Sensors, p. 329.

[3] D. Kohl, *Gas Sensors* (Kluwer Academic Publishers, 1992), chap. Oxidic Semiconductor Gas Sensors, p. 43.

[4] J. B. McManus, P. L. Kebabian, and M. S. Zahniser, "Astigmatic mirror multipass absorption cells for long-path-length spectroscopy," Applied Optics **34**, 3336–3348 (1995).

[5] D. D. Nelson, J. B. McManus, S. C. Herndon, M. S. Zahniser, B. Tuzson, and L. Emmenegger, "New method for isotopic ratio measurements of atmospheric carbon dioxide using a 4.3 μm pulsed quantum cascade laser," Applied Physics B: Lasers and Optics **90**, 301–309 (2008).

[6] P. Werle, "Tunable diode laser absorption spectroscopy: recent findings and novel approaches," Infrared Physics & Technology **37**, 59 – 66 (1996).

[7] M. Ortsiefer, G. Böhm, M. Grau, K. Windhorn, E. Rönneberg, J. Rosskopf, R. Shau, O. Dier, and M.-C. Amann, "Electrically pumped room temperature CW VCSELs with 2.3 μm emission wavelength," Electronics Letters **42**, 640–641 (2006).

[8] M. Ortsiefer, J. Rosskopf, E. Rönneberg, Y. Xu, K. Maisberger, R. Shau, C. Neumeyr, W. Hofmann, G. Böhm, A. Hangauer, J. Chen, R. Strzoda, and M.-C. Amann, "Extended near-infrared wavelength VCSELs for optical sensing," in "IEEE Semiconductor Laser Conference (ISLC)," (2008), pp. 167–168.

[9] P. Werle, B. Scheumann, and J. Schandl, "Real-time signal-processing concepts for trace-gas analysis by diode-laser spectroscopy," Optical Engineering **33**, 3093–3105 (1994).

[10] L. Rothman, D. Jacquemart, A. Barbe, D. C. Benner, M. Birk, L. Brown, M. Carleer, C. Chackerian, Jr., K. Chance, L. Coudert, V. Dana, V. Devi, J.-M. Flaud, R. Gamache, A. Goldman, J.-M. Hartmann, K. Jucks, A. Maki, J.-Y. Mandin, S. Massie, J. Orphal, A. Perrin, C. Rinsland, M. Smith, J. Tennyson, R. Tolchenov, R. Toth, J. V. Auwera, P. Varanasi, and G. Wagner, "The HITRAN 2004 molecular spectroscopic database," Journal of Quantitative Spectroscopy and Radiative Transfer **96**, 139 – 204 (2005).

[11] G. Herzberg, *Molecular Spectra and Molecular Structure I - Spectra of Diatomic Molecules* (D. van Nostrand Company, 1950), 2nd ed.

[12] W. Demtröder, *Laser Spectroscopy*, vol. 3 (Springer, 2003).

[13] J. Olivero and R. Longbothum, "Empirical fits to the Voigt line width: a brief review,," Journal of Quantitative Spectroscopy and Radiative Transfer **17**, 233–236 (1977).

[14] J. Reid and D. Labrie, "Second-harmonic detection with tunable diode lasers - comparison of experiment and theory," Applied Physics B: Lasers and Optics **26**, 203–210 (1981).

[15] P. Kluczynski, J. Gustafsson, Åsa M. Lindberg, and O. Axner, "Wavelength modulation absorption spectrometry – an extensive scrutiny of the generation of signals," Spectrochimica Acta Part B: Atomic Spectroscopy **56**, 1277 – 1354 (2001).

[16] A. Hangauer, J. Chen, and M.-C. Amann, "Modeling of the n-th harmonic spectra used in wavelength modulation spectroscopy and their properties," Applied Physics B: Lasers and Optics **90**, 249 – 254 (2008).

[17] R. Arndt, "Analytical line shapes for Lorentzian signals broadened by modulation," Journal of Applied Physics **36**, 2522–2524 (1965).

[18] Vertilas GmbH, "Sensor Technology Products," http://www.vertilas.com/produkte_produktuebersicht.php.

[19] Nanoplus GmbH, "Data sheets and application notes of nanoplus DFB laser diodes," http://www.nanoplus.com/content/view/64/.

[20] A. Bachmann, T. Lim, K. Kashani-Shirazi, O. Dier, C. Lauer, and M.-C. Amann, "Continuous-wave operation of electrically pumped GaSb-based vertical cavity surface emitting laser at 2.3 μm," Electronics Letters **44**, 202–203 (2008).

[21] S. Arafin, A. Bachmann, K. Kashani-Shirazi, and M.-C. Amann, "Electrically-pumped continuous-wave vertical-cavity surface-emitting lasers at $\sim$ 2.6 μm," Applied Physics Letters pp. 131120 – 131122 (2009).

[22] S. Belahsene, L. Naehle, M. Fischer, J. Koeth, G. Boissier, P. Grech, G. Narcy, A. Vicet, and Y. Rouillard, "Laser diodes for gas sensing emitting at 3.06 μm at room temperature," IEEE Photonics Technology Letters **22**, 1084 –1086 (2010).

[23] T.-C. Lu, S.-W. Chen, T.-T. Wu, P.-M. Tu, C.-K. Chen, C.-H. Chen, Z.-Y. Li, H.-C. Kuo, and S.-C. Wang, "Continuous wave operation of current injected GaN vertical cavity surface emitting lasers at room temperature," Applied Physics Letters **97**, 071114 (2010).

[24] A. Muller, S. Blaser, L. Hvozdara, and H. Page, "Singlemode room-temperature cw operation and high power pulsed operation of quantum cascade lasers," in "Laser Applilcations to Chemical, Security and Environmental Analysis," (Optical Society of America, 2006), p. MD3.

[25] Alpes Lasers, "List of CW-RT-DFB-QC lasers," http://www.alpeslasers.ch/lasers-on-stock/lasersSTANcw-rt.html.

[26] M. Rahim, M. Arnold, F. Felder, K. Behfar, and H. Zogg, "Midinfrared lead-chalcogenide vertical external cavity surface emitting laser with 5 μm wavelength," Applied Physics Letters **91**, 151102 (2007).

[27] H.-E. Li and K. Iga, *Vertical-Cavity Surface-Emitting Laser Devices* (Springer, Berlin, 2002).

[28] F. Koyama, S. Kinoshita, and K. Iga, "Room-temperature continuous wave lasing characteristics of a GaAs vertical cavity surface-emitting laser," Applied Physics Letters **55**, 221–223 (1989).

[29] B. Weigl, M. Grabherr, R. Michalzik, G. Reiner, and K. J. Ebeling, "High-power single-mode selectively oxidized vertical-cavity surface-emitting lasers," IEEE Photonics Technology Letters **8**, 971–973 (1996).

[30] M. Grabherr, R. Jaeger, R. Michalzik, B. Weigl, G. Reiner, and K. J. Ebeling, "Efficient single-mode oxide confined GaAs VCSELso emitting in the 850 nm wavelength regime," IEEE Photonics Technology Letters **10**, 1304–1306 (1997).

[31] M. Ortsiefer, R. Shau, G. Böhm, F. Köhler, and M.-C. Amann, "Low-threshold index-guided 1.5 μm long-wavelength vertical-cavity surface-emitting laser with high efficiency," Applied Physics Letters **76**, 2179–2181 (2000).

[32] M.-C. Amann and M. Ortsiefer, "Long-wavelength ($\lambda \geq 1.3$ μm) InGaAlAs-InP vertical-cavity surface-emitting lasers for applications in optical communication and sensing," Phys. Status Solidi A **203**, 3538–3544 (2006).

[33] R. D. Esman and D. L. Rode, "Semiconductor-laser thermal time constant," Journal of Applied Physics **59**, 407–409 (1986).

[34] H. I. Abdelkader, H. H. Hausien, and J. D. Martin, "Temperature rise and thermal rise-time measurements of a semiconductor laser diode," Review of Scientific Instruments **63**, 2004–2007 (1992).

[35] P. K. L. Chan, K. P. Pipe, Z. Mi, J. Yang, P. Bhattacharya, and D. Lüerßen, "Thermal relaxation time and heat distribution in pulsed InGaAs quantum dot lasers," Applied Physics Letters **89**, 011110 (2006).

[36] P. V. Mena, J. J. Morikuni, S.-M. Kang, A. V. Harton, and K. W. Wyatt, "A comprehensive circuit-level model of vertical-cavity surface-emitting lasers," Journal of Lightwave Technology **17**, 2612–2632 (1999).

[37] G. Hasnain, K. Tai, L. Yang, Y. H. Wang, R. J. Fischer, J. D. Wynn, B. Weir, N. K. Dutta, and A. Y. Cho, "Performance of gain-guided surface emitting lasers with semiconductor distributed Bragg reflectors," IEEE Journal of Quantum Electronics **27**, 1377–1385 (1991).

[38] M. Lackner, G. Totschnig, F. Winter, M. Ortsiefer, M.-C. Amann, R. Shau, and J. Rosskopf, "Demonstration of methane spectroscopy using a vertical-cavity surface-emitting laser at 1.68 μm with up to 5 MHz repetition rate," Measurement Science and Technology **14**, 101–106 (2003).

[39] R. Michalzik and K. J. Ebeling, "Modelling of gain-guided vertical-cavity laser diodes," Microelectronic Engineering **19**, 123–126 (1992).

[40] M.-C. Amann and J. Buus, *Tunable Laser Diodes* (Artech House publishers, Norwood, 1998), pp. 1–5.

[41] A. Hangauer, J. Chen, R. Strzoda, and M.-C. Amann, "High-speed tuning in vertical-cavity surface-emitting lasers," in "CLEO Europe - EQEC 2009," (2009), CB13.5.

[42] A. Hangauer, J. Chen, and M. C. Amann, "Comparison of plasma-effect in different InP-based VCSELs," Conference on Lasers and Electro Optics (CLEO) p. CMO4 (2010).

[43] R. Strzoda, J. Chen, and A. Hangauer, "Gas sensing with infrared VCSELs," in "10th International Conference on Mid-Infrared Optoelectronics: Materials and Devices," (2010).

[44] P. Corrc, O. Girad, and I. de Faria, "On the thermal contribution to the FM response of DFB lasers: theory and experiment," IEEE Journal of Quantum Electronics **30**, 2485–2490 (1994).

[45] J. Chen, A. Hangauer, R. Strzoda, and M.-C. Amann, "Accurate extraction method for the FM response of tunable diode lasers based on wavelength modulation spectroscopy," Applied Physics B: Lasers and Optics **90**, 243–247 (2008).

[46] J. Chen, A. Hangauer, R. Strzoda, and M.-C. Amann, "Experimental characterization of the frequency modulation behavior of vertical cavity surface emitting lasers," Applied Physics Letters **91**, 141105 (2007).

[47] J. Chen, A. Hangauer, and M.-C. Amann, "Simplified model of the dynamic thermal tuning behavior of VCSELs," IEEE Photonics Technology Letters **20**, 1082–1084 (2008).

[48] S. Schilt and L. Thévenaz, "Experimental method based on wavelength-modulation spectroscopy for the characterization of semiconductor lasers under direct modulation," Applied Optics **43**, 4446–4453 (2004).

[49] A. Lytkine, W. Jäger, and J. Tulip, "Frequency tuning of long-wavelength VCSELs," Spectrochimica Acta Part A **63**, 940–946 (2006).

[50] A. Lytkine, W. Jäger, and J. Tulip, "Long-wavelength VCSELs for applications in absorption spectroscopy: tuning rates and modulation performances," Proceedings of SPIE **5737**, 157–166 (2005).

[51] G. Hernandez, *Fabry-Perot Interferometers* (Cambridge University Press, Cambridge, 1986).

[52] P. Kluczynski and O. Axner, "Theoretical description based on fourier analysis of wavelength-modulation spectrometry in terms of analytical and background signals," Applied Optics **38**, 5803–5815 (1999).

[53] M. Grabherr, D. Wiedenmann, R. Jaeger, and R. King, "Fabrication and performance of tunable single-mode VCSELs emitting in the 750 to 1000 nm range," Proceedings of SPIE **5737**, 120–128 (2005).

[54] M.-C. Amann and J. Buus, *Tunable Laser Diodes* (Artech House publishers, Norwood, 1998), pp. 94–99.

[55] H. Carslaw and J. Jaeger, *Conduction of Heat in Solids* (Clarendon Press, Oxford, U.K., 1990).

[56] M. Abramowitz and I. A. Stegun, *Handbook of Mathematical Functions* (Dover, New York, 1970).

[57] J. Liu, J. Jeffries, and R. Hanson, "Wavelength modulation absorption spectroscopy with $2f$ detection using multiplexed diode lasers for rapid temperature measurements in gaseous flows," Applied Physics B: Lasers and Optics **78**, 503–511 (2004).

[58] A. Bachmann, K. Kashani-Shirazi, T. Lim, O. Dier, C. Lauer, and M.-C. Amann, "Single-mode continuous wave operation of electrically pumped 2.25 μm GaSb-based VCSEL," 20th International Conference on Indium Phosphide and Related Materials, Versailles, France (2008).

[59] A. Hangauer, J. Chen, R. Strzoda, M. Ortsiefer, and M.-C. Amann, "Wavelength modulation spectroscopy with a widely tunable InP-based 2.3 μm vertical-cavity surface-emitting laser," Optics Letters **33**, 1566 – 1568 (2008).

[60] J. Chen, A. Hangauer, R. Strzoda, and M.-C. Amann, "Simultaneous CH_4 and CO sensing with 2.3 μm vertical surface emitting lasers and their application," in "Proceedings of the Fifth Joint Symposium on Opto- & Microelectronic Devices and Circuits (SODC)," (2009), pp. 58–61.

[61] J. Chen, A. Hangauer, A. Bachmann, T. Lim, K. Kashani, R. Strzoda, and M.-C. Amann, "CO and CH_4 sensing with single mode 2.3 μm GaSb-based VCSEL," in "Conference on Lasers and Electro Optics (CLEO)," (Baltimore, USA, 2009), p. CThI2.

[62] Y. L. Hoo, W. Jin, C. Shi, H. L. Ho, D. N. Wang, and S. C. Ruan, "Design and modeling of a photonic crystal fiber gas sensor," Applied Optics **42**, 3509–3515 (2003).

[63] M. Born and E. Wolf, *Principles of Optics* (Cambridge University Press, 1999), 7th ed.

[64] J. C. Dainty, J. W. Goodman, A. Ennos, T. S. Mckechnie, M. Francon, and G. Party, *Laser Speckle and Related Phenomena* (Springer-Verlag, 1975).

[65] J. Hodgkinson, D. Masiyano, and R. P. Tatam, "Gas cells for tunable diode laser absorption spectroscopy employing optical diffusers. part 1: single and dual pass cells," Applied Physics B: Lasers and Optics **100**, 291–302 (2010).

[66] *Manual of model SR830 DSP Lock-In Amplifier, Standford Research Systems.*

[67] S. Schilt, L. Thévenaz, and P. Robert, "Wavelength modulation spectroscopy: combined frequency and intensity laser modulation," Applied Optics **42**, 6728–6738 (2003).

[68] J. Chen, A. Hangauer, R. Strzoda, and M.-C. Amann, "Laser spectroscopic oxygen sensor using diffuse reflector based optical cell and advanced signal processing," Applied Physics B: Lasers and Optics **100**, 417 – 425 (2010).

[69] J. Chen, A. Hangauer, R. Strzoda, M. Fleischer, and M.-C. Amann, "VCSEL-based oxygen sensor for combustion optimization in gas/oil furnaces," in "Conference on Laser Electro-Optics (CLEO)," (Baltimore, USA, 2009), p. CTuA4.

[70] A. Hangauer, A. Spitznas, J. Chen, R. Strzoda, H. Link, and M. Fleischer, "Laser spectroscopic oxygen sensor for real time combustion optimization," Procedia Chemistry **1**, 955 – 958 (2009).

[71] D. Herriott, H. Kogelnik, and R. Kompfner, "Off-axis paths in spherical mirror interferometers," Applied Optics **3**, 523–526 (1964).

[72] J. U. White, "Long paths of large aperture," Journal of the Optical Society of America **32**, 285 (1942).

[73] J. Herbst, "Kompakte Langwegmesszellen für die Absorptionsspektroskopie," in "VDI-Berichte 2047," (2008), pp. 233–234. Optische Analysenmesstechnik in Industrie und Umwelt : Tagung, Dortmund.

[74] P. Russell, "Photonic Crystal Fibers," Science **299**, 358–362 (2003).

[75] T. G. Euser, J. S. Y. Chen, M. Scharrer, P. S. J. Russell, N. J. Farrer, and P. J. Sadler, "Quantitative broadband chemical sensing in air-suspended solid-core fibers," Journal of Applied Physics **103**, 103108 (2008).

[76] J. Chen, A. Hangauer, R. Strzoda, T. Euser, J. Chen, M. Scharrer, P. Russell, and M.-C. Amann, "Sensitivity limits for near- infrared gas sensing with suspended-core PCFs directly coupled with VCSELs," in "Conference on Laser Electro-Optics (CLEO)," (San Jose, USA, 2010), p. JThB7.

[77] A. S. Webb, F. Poletti, D. J. Richardson, and J. K. Sahu, "Suspended-core holey fiber for evanescent-field sensing," Optical Engineering **46**, 010503 (2007).

[78] S. Lundqvist, personal communication (2010).

[79] S. Lundqvist and P.-A. Thorsen, "Wavelength modulation spectroscopy method and system (US patent 7193718)," (2007).

[80] S. Lundqvist and P. Kluczynski, "Method for improving the sensitivity in a fiber coupled diode laser spectrometer by selective predistortion," in "Book of Abstracts, Field Laser Applications in Industry and Research (FLAIR)," (2007), p. 36.

[81] T. Euser, personal communication (2010).

[82] Thanks Tijmen Euser (Max-Planck Institute) for sending the SEM figure.

[83] Thanks Tijmen Euser (Max-Planck Institute) for sending the SEM figure.

[84] J. Chen, A. Hangauer, R. Strzoda, and M.-C. Amann, "Resolution limits of laser spectroscopic absorption measurements with hollow glass waveguides," Applied Optics **49**, 5254–5261 (2010).

[85] J. A. Harrington, "A review of IR transmitting, hollow waveguides," Fiber and Integrated Optics **19**, 211–217 (2000).

[86] J. A. Harrington, C. Rabii, and D. Gibson, "Transmission properties of hollow glass waveguides for the delivery of CO_2 surgical laser power," IEEE Journal of Selected Topics in Quantum Electronics **5**, 948–953 (1999).

[87] Y. Matsuura, T. Abel, and J. A. Harrington, "Optical properties of small-bore hollow glass waveguides," Applied Optics **34**, 6842–6847 (1995).

[88] S. Hartwig and A. Lambrecht, "Characterization of hollow fibres for compact infrared gas measurement cells," Technisches Messen **75**, 555–564 (2008).

[89] C. Young, S.-S. Kim, Y. Luzinova, M. Weida, D. Arnone, E. Takeuchi, T. Day, and B. Mizaikoff, "External cavity widely tunable quantum cascade laser based hollow waveguide gas sensors for multianalyte detection," Sensors and Actuators B: Chemical **140**, 24–28 (2009).

[90] C. A. Worrell and N. A. Gallen, "Trace-level detection of gases and vapours with mid-infrared hollow waveguides," Journal of Physics D: Applied Physics **30**, 1984–1995 (1997).

[91] F. de Melas, V. V. Pustogov, N. Croitoru, and B. Mizaikoff, "Development and optimization of a mid-infrared hollow waveguide gas sensor combined with a supported capillary membrane sampler," Applied Spectroscopy **57**, 187–198 (2003).

[92] J. Harrington, *Hollow-glass waveguides have unique properties.*

[93] R. K. Nubling and J. A. Harrington, "Launch conditions and mode coupling in hollow-glass waveguides," Optical Engineering **37**, 2454–2458 (1998).

[94] J. B. McManus, "Paraxial matrix description of astigmatic and cylindrical mirror resonators with twisted axes for laser spectroscopy," Applied Optics **46**, 472–482 (2007).

[95] W. Freude, *Optische Kommunikationstechnik* (Springer-Verlag, 2002), chap. 5.

[96] J. W. Goodman, *Laser Speckle and Related Phenomena* (Springer Verlag, 1975), chap. 2.

[97] T. Iseki, H. Tai, and K. Kimura, "A portable remote methane sensor using a tunable diode laser," Measurement Science and Technology **11**, 594–602 (2000).

[98] D. S. Bomse, D. C. Hovde, S.-J. Chen, and J. A. Silver, "Early fire sensing using near-IR diode laser spectroscopy," in "Diode Lasers and Applications in Atmospheric Sensing," , A. Fried, ed. (SPIE, 2002), 4817, pp. 73–81.

[99] S.-J. Chen, C. Hovde, K. A. Peterson, and A. Marshal, "Fire detection using smoke and gas sensors," Fire Safety Journal **42**, 507–515 (2007).

[100] P. Werle, F. Slemr, K. Maurer, R. Kormann, R. Mücke, and B. Janker, "Near- and mid-infrared laser-optical sensors for gas analysis," Optics and Lasers in Engineering **37**, 101–114 (2002).

[101] L. C. Philippe and R. K. Hanson, "Laser diode wavelength-modulation spectroscopy for simultaneous measurement of temperature, pressure, and velocity in shock-heated oxygen flows," Applied Optics **32**, 6090–6103 (1993).

[102] J. T. C. Liu, J. B. Jeffries, and R. K. Hanson, "Large-modulation-depth $2f$ spectroscopy with diode lasers for rapid temperature and species measurements in gases with blended and broadened spectra," Applied Optics **43**, 6500–6509 (2004).

[103] N. Wiener, *Extrapolation, Interpolation, and Smoothing of Stationary Time Series* (Wiley, New York, 1949).

[104] H. Riris, C. B. Carlisle, R. E. Warren, D. E. Cooper, R. U. Martinelli, R. J. Menna, P. K. York, D. Z. Garbuzov, H. Lee, J. H. Abeles, N. Morris, J. C. Connolly, and S. Y. Narayan, "Signal processing strategies in tunable diode laser spectrometers," Spectrochimica Acta Part A: Molecular and Biomolecular Spectroscopy **52**, 843 – 849 (1996).

[105] A. Fried, B. Henry, and J. R. Drummond, "Tunable diode laser ratio measurements of atmospheric constituents by employing dual fitting analysis and jump scanning," Applied Optics **32**, 821–827 (1993).

[106] R. E. Kalman, "A new approach to linear filtering and prediction problems," Transactions of the ASME - Journal of Basic Engineering pp. 35–45 (1960).

[107] H. Riris, C. B. Carlisle, and R. E. Warren, "Kalman filtering of tunable diode laser spectrometer absorbance measurements," Applied Optics **33**, 5506–5508 (1994).

[108] D. Leleux, R. Claps, W. Chen, F. Tittel, and T. Harman, "Applications of Kalman filtering to real-time trace gas concentration measurements," Applied Physics B: Lasers and Optics **74**, 85–93 (2002).

[109] G. A. F. Seber and C. J. Wild, *Nonlinear Regression* (John Wiley & Sons, 2003).

[110] C. Rao and H. Toutenburg, *Linear models : least squares and alternatives* (Springer, 1995).

[111] S. M. Kay, *Fundamentals of Statistical Signal Processing: Estimation Theory* (Prentice Hall).

[112] D. W. Marquardt, "An algorithm for least-squares estimation of nonlinear parameters," Journal of the Society for Industrial and Applied Mathematics **11**, 431–441 (1963).

[113] Z. Michalewicz, *Genetic algorithms + data structures = evolution programs* (Springer-Verlag New York, Inc., New York, NY, USA, 1994).

[114] A. Hangauer, J. Chen, and M.-C. Amann, "Compact and calibration-free laser spectroscopic sensors using wavelength modulation spectrometry," Submitted to Optics Letters.

[115] C. Hentschel, *Fiber Optics Handbook, An Introduction and Reference Guide to Fiber Optic Technology and Measurement Techniques* (Hewlett Packard, 1989).

[116] J. Chen, A. Hangauer, R. Strzoda, and M.-C. Amann, "VCSEL-based calibration-free carbon monoxide sensor at 2.3 μm with in-line reference cell," Applied Physics B: Lasers and Optics (2010).

[117] A. Bjorck, *Numerical methods for least squares problems* (Society For Industrial and Applied Mathematics, Philadelphia, U.S., 1996).

[118] A. Hangauer, J. Chen, R. Strzoda, and M.-C. Amann, "Laser wavelength stabilization using gases with complex spectral fingerprint," in "Field Laser Applications in Industry and Research (FLAIR)," (Garmisch-Partenkirchen, 2009).

[119] A. Hangauer, J. Chen, K.-U. Seemann, P. Karge, R. Strzoda, and M.-C. Amann, "Compact VCSEL-based CO_2 and H_2O sensor with inherent wavelength calibration for safety and air-quality applications," in "Conference on Lasers and Electro Optics (CLEO)," (San Jose, USA, 2010), p. JThB3.

[120] J. Chen, A. Hangauer, R. Strzoda, and M. C. Amann, "Tunable diode laser spectroscopy with optimum wavelength scanning," Applied Physics B: Lasers and Optics **100**, 331 – 339 (2010).

[121] M. Sigrist, R. Bartlome, D. Marinov, J. Rey, D. Vogler, and H.Wächter, "Trace gas monitoring with infrared laser-based detection schemes," Applied Physics B: Lasers and Optics **90**, 289–300 (2008).

[122] R. Dechter, *Constraint Processing* (Morgan Kaufmann, 2003).

[123] S. Han, "A globally convergent method for nonlinear programming," Journal of Optimization Theory and Applications **22**, 297 (1977).

[124] R. Fletcher and M. Powell, "A rapidly convergent descent method for minimization," Computer Journal **6**, 163–168 (1963).

[125] H. Teichert, T. Fernholz, and V. Ebert, "Simultaneous in situ measurement of CO, H_2O, and gas temperatures in a full-sized coal-fired power plant by near-infrared diode lasers," Applied Optics **42**, 2043–2051 (2003).

[126] J. Chen, A. Hangauer, R. Strzoda, M. Ortsiefer, M. Fleischer, and M. C. Amann, "Compact Carbon Monoxide Sensor Using a Continuously Tunable 2.3 μm Single-Mode VCSEL," Proceedings of the 21st Annual Meeting of the IEEE Lasers and Electro-Optics Society **9**, 721 – 722 (2008).

[127] A. Hangauer, J. Chen, R. Strzoda, M. Fleischer, and M.-C. Amann, "Fire detection with a compact laser spectroscopic carbon-monoxide sensor," accepted for publication in Sensors and Actuators B: Chemical (2010).

[128] J. Chen, A. Hangauer, R. Strzoda, M. Fleischer, and M.-C. Amann, "Low-level and ultra-low volume hollow waveguide based carbon monoxide sensor," Optics Letters **35** (2010).

[129] Amin Spitznas and Hans Link, both with Siemens Building Technologies, private communication (2008).

[130] National Industrial Fuel Efficiency Service LTD, *The Boiler Operators Handbook* (Graham & Trotman Limited, 1989).

[131] Buderus Heiztechnik GmbH, ed., *Handbuch für Heizungstechnik* (Beuth Verlag GmbH, 2002).

[132] E. M. Logothetis, "Resistive-type exhaust gas sensors," in "Proceedings of the 8th Automotive Materials Conference: Ceramic Engineering and Science Proceedings," (1980), 5/6, pp. 281–301.

[133] Diffuse optical cell designed by R. Strzoda and O. Hennig (Siemens AG).

[134] K. J. Ritter and T. D. Wilkerson, "High-resolution spectroscopy of the oxygen a band," Journal of Molecular Spectroscopy **121**, 1 – 19 (1987).

[135] Center for Disease Control and Prevention, "Carbon Monoxide Poisoning: Fact Sheet," Online electronic publication: http://www.cdc.gov/co/faqs.htm (2007).

[136] R. Pohle, E. Simon, R. Schneider, M. Fleischer, R. Sollacher, H. Gao, K. Müller, P. Jauch, M. Loepfe, H.-P. Frerichs, and C. Wilbertz, "Fire detection with low power FET gas sensors," Sensors and Actuators B: Chemical **120**, 669 – 672 (2007).

[137] J.-C. Nicolas, A. N. Baranov, Y. Cuminal, Y. Rouillard, and C. Alibert, "Tunable diode laser absorption spectroscopy of carbon monoxide around 2.35 μm," Applied Optics **37**, 7906–7911 (1998).

[138] A. Vicet, D. Yarekha, A. Pérona, Y. Rouillard, S. Gaillard, and A. Baranov, "Trace gas detection with antimonide-based quantum-well diode lasers," Spectrochimica Acta Part A **58**, 2405–2412 (2002).

[139] V. Ebert, H. Teichert, P. Strauch, T. Kolb, H. Seifert, and J. Wolfrum, "Sensitive in situ detection of CO and O_2 in a rotary kiln-based hazardous waste incinerator using 760 nm and new 2.3 μm diode lasers," Proceedings of the Combustion Institute **30**, 1611–1618 (2005).

[140] J. Wang, M. Maiorov, D. S. Baer, D. Z. Garbuzov, J. C. Connolly, and R. K. Hanson, "In situ combustion measurements of CO with diode-laser absorption near 2.3 μm," Applied Optics **39**, 5579–5589 (2000).

[141] G. Böhm, M. Grau, O. Dier, K. Windhorn, E. Rönneberg, J. Rosskopf, R. Shau, R. Meyer, M. Ortsiefer, and M.-C. Amann, "Growth of InAs-containing quantum wells for InP-based VCSELs emitting at 2.3μm," Journal of Crystal Growth **301**, 941–944 (2007).

[142] D. W. Allan, "Statistics of atomic frequency standards," Proc. IEEE **54**, 221–230 (1966).

[143] P. Werle, R. Muecke, and F. Slemr, "The limits of signal averaging in atmospheric trace gas monitoring by tunable diode-laser absorption spectroscopy," Applied Physics B: Lasers and Optics **57**, 131–139 (1993).

[144] A. Hangauer, J. Chen, R. Strzoda, M. Fleischer, and M.-C. Amann, "Fire detection with a compact, 2.3 μm VCSEL-based carbon monoxide sensor," in "Conference on Lasers and Electro Optics (CLEO)," (2009), p. CTuA3.

[145] European Standard, *EN54-26: Fire detection and fire alarm systems - Part 26: Point fire detectors using carbon monoxide sensors* (Beuth, Berlin, 2008).

[146] B. Dautzenberg, "HELP-COmets-Studie: Erhebung zur Kohlenmonoxid-Belastung bei über 100.000 Raucher- und NichtraucherInnen in der EU," (2007).

Publications

Journal Publications

- J. Chen, A. Hangauer, R. Strzoda, M. Fleischer, and M.-C. Amann, "Low-level and ultra-low volume hollow waveguide based carbon monoxide sensor," Optics Letters **35** (2010).

- A. Hangauer, J. Chen, R. Strzoda, M. Fleischer, and M.-C. Amann, "Fire detection with a compact laser spectroscopic carbon-monoxide sensor," accepted for publication in Sensors and Actuators B: Chemical (2010).

- J. Chen, A. Hangauer, R. Strzoda, and M.-C. Amann, "Resolution limits of laser spectroscopic absorption measurements with hollow glass waveguides," Applied Optics **49**, 5254–5261 (2010).

- J. Chen, A. Hangauer, R. Strzoda, and M.-C. Amann, "Tunable diode laser spectroscopy with optimum wavelength scanning," Applied Physics B: Lasers and Optics **100**, 331 – 339 (2010).

- J. Chen, A. Hangauer, R. Strzoda, and M.-C. Amann, "VCSEL-based calibration-free carbon monoxide sensor at 2.3 μm with in-line reference cell," Applied Physics B: Lasers and Optics (2010).

- J. Chen, A. Hangauer, R. Strzoda, and M.-C. Amann, "Laser spectroscopic oxygen sensor using diffuse reflector based optical cell and advanced signal processing," Applied Physics B: Lasers and Optics **100**, 417 – 425 (2010).

- A. Hangauer, J. Chen, R. Strzoda, M. Ortsiefer, and M.-C. Amann, "Wavelength modulation spectroscopy with a widely tunable InP-based 2.3 μm vertical-cavity surface-emitting laser," Optics Letters **33**, 1566 – 1568 (2008).

- J. Chen, A. Hangauer, and M.-C. Amann, "Simplified model of the dynamic thermal tuning behavior of VCSELs," IEEE Photonics Technology Letters **20**, 1082–1084 (2008).

- J. Chen, A. Hangauer, R. Strzoda, and M.-C. Amann, "Accurate extraction method for the FM response of tunable diode lasers based on wavelength modulation spectroscopy," Applied Physics B: Lasers and Optics **90**, 243–247 (2008).

- A. Hangauer, J. Chen, and M.-C. Amann, "Modeling of the n-th harmonic spectra used in wavelength modulation spectroscopy and their properties," Applied Physics B: Lasers and Optics **90**, 249 – 254 (2008).

- J. Chen, A. Hangauer, R. Strzoda, and M.-C. Amann, "Experimental characterization of the frequency modulation behavior of vertical cavity surface emitting lasers," Applied Physics Letters **91**, 141105 (2007).

Conference Publications

- J. Chen, A. Hangauer, R. Strzoda, T. Euser, J. S. Y. Chen, M. Scharrer, P. Russell, and M.-C. Amann, "Sensitivity limits for near- infrared gas sensing with suspended-core PCFs directly coupled with VCSELs," in "Conference on Laser Electro-Optics (CLEO)," (2010), p. JThB7.

- A. Hangauer, J. Chen, K.-U. Seemann, P. Karge, R. Strzoda, and M.-C. Amann, "Compact VCSEL-based CO_2 and H_2O sensor with inherent wavelength calibration for safety and air-quality applications," in "Conference on Lasers and Electro Optics (CLEO)," (2010), p. JThB3.

- A. Hangauer, J. Chen, and M.-C. Amann, "Comparison of plasma-effect in different InP-based VCSELs," in "Conference on Lasers and Electro Optics (CLEO)," (2010), p. CMO4.

- A. Hangauer, J. Chen, and M.-C. Amann, "Vertical-cavity surface-emitting laser *P-I*-characteristic at constant internal temperature," in "Proceedings of the Sixth Joint Symposium on Opto- & Microelectronic Devices and Circuits (SODC)," (2010).

- J. Chen, A. Hangauer, R. Strzoda, and M.-C. Amann, "Fiber sensor using hollow capillary fiber directly coupled with VCSELs," in "Proceedings of the Sixth Joint Symposium on Opto- & Microelectronic Devices and Circuits (SODC)," (2010).

- A. Hangauer, J. Chen, R. Strzoda, M. Fleischer, and M.-C. Amann, "Laser-spectroscopic, ultra low volume and low level carbon monoxide sensor," in "Proceedings of Eurosensors XXIV," (2010).

- R. Strzoda, J. Chen, and A. Hangauer, "Gas sensing with infrared VCSELs," in "10th International Conference on Mid-Infrared Optoelectronics: Materials and Devices," (2010), (invited).

- J. Chen, A. Hangauer, A. Bachmann, T. Lim, K. Kashani, R. Strzoda, and M.-C. Amann, "CO and CH_4 sensing with single mode 2.3 μm GaSb-based VCSEL," in "Conference on Lasers and Electro Optics (CLEO)," (2009), p. CThI2.

- J. Chen, A. Hangauer, R. Strzoda, M. Fleischer, and M.-C. Amann, "VCSEL-based oxygen sensor for combustion optimization in gas/oil furnaces," in "Conference on Laser Electro-Optics (CLEO)," (2009), p. CTuA4.

- J. Chen, A. Hangauer, R. Strzoda, and M.-C. Amann, "Simultaneous CH_4 and CO sensing with 2.3 μm vertical surface emitting lasers and their application," in "Proceedings of the Fifth Joint Symposium on Opto- & Microelectronic Devices and Circuits (SODC)," (2009), pp. 58–61.

- A. Hangauer, J. Chen, R. Strzoda, M. Fleischer, and M.-C. Amann, "Fire detection with a compact, 2.3 μm VCSEL-based carbon monoxide sensor," in "Conference on Lasers and Electro Optics (CLEO)," (2009), p. CTuA3.

- A. Hangauer, J. Chen, R. Strzoda, and M.-C. Amann, "Analysis of dynamic tuning effects in vertical-cavity surface-emitting lasers," in "Proceedings of the Fifth Joint Symposium on Opto- & Microelectronic Devices and Circuits (SODC)," (2009), pp. 28–31.

- J. Chen, A. Hangauer, R. Strzoda, M. Fleischer, and M.-C. Amann, "Miniaturized laser spectroscopic CO sensor for industrial and safety applications," in "Proceedings of the Eurosensors XXIII conference," , vol. 1 (2009), vol. 1, pp. 1383 – 1386.

- A. Hangauer, A. Spitznas, J. Chen, R. Strzoda, H. Link, and M. Fleischer, "Laser spectroscopic oxygen sensor for real time combustion optimization," in "Proceedings of the Eurosensors XXIII conference," , vol. 1 (2009), vol. 1, pp. 955 – 958.

- A. Hangauer, J. Chen, R. Strzoda, and M.-C. Amann, "Laser wavelength stabilization using gases with complex spectral fingerprint," in "International Conference on Field Laser Applications in Industry and Research," (2009), p. 44.

- J. Chen, A. Hangauer, R. Strzoda, T. Euser, J. S. Y. Chen, M. Scharrer, P. Russell, and M.-C. Amann, "Near-infrared gas sensing using hollow waveguides and PCFs directly coupled to VCSELs," in "International Conference on Field Laser Applications in Industry and Research," (2009), p. 93.

- A. Hangauer, J. Chen, R. Strzoda, and M.-C. Amann, "High-speed tuning in vertical-cavity surface-emitting lasers," in "CLEO Europe - EQEC 2009," (2009), p. CB13.5.

- J. Chen, A. Hangauer, R. Strzoda, and M.-C. Amann, "Tunable diode laser spectroscopy with optimum nonlinear wavelength scanning," in "Book of Abstracts, 7th Conference on Tunable Diode Laser Spectroscopy (TDLS)," (2009), pp. D–4.

- J. Chen, A. Hangauer, R. Strzoda, and M.-C. Amann, "Oxygen sensor with diffuse reflector employed in harsh conditions for concentration and pressure measurements," in "Book of Abstracts, 7th Conference on Tunable Diode Laser Spectroscopy (TDLS)," (2009), pp. E–16.

- A. Hangauer, J. Chen, R. Strzoda, and M.-C. Amann, "Miniaturized sensor without separate reference cell for carbon-monoxide detection at 2.3 μm," in "Book of Abstracts, 7th Conference on Tunable Diode Laser Spectroscopy (TDLS)," (2009), pp. C–4.

- A. Hangauer, J. Chen, R. Strzoda, and M.-C. Amann, "Comparison of GaSb- and InP-based VCSELs at 2.3 μm," in "Book of Abstracts, 7th Conference on Tunable Diode Laser Spectroscopy (TDLS)," (2009), pp. E–4.

- J. Chen, A. Hangauer, R. Strzoda, M. Ortsiefer, M. Fleischer, and M.-C. Amann, "Compact carbon monoxide sensor using a continuously tunable 2.3 μm single-mode VCSEL," in "The 21st Annual Meeting of The IEEE Lasers & Electro-Optics Society," (2008), pp. 721–722.

- A. Hangauer, J. Chen, R. Strzoda, and M.-C. Amann, "Analysis of thermal tuning in vertical-cavity surface-emitting lasers," in "European Semiconductor Laser Workshop," (2008), p. 20.

- J. Chen, A. Hangauer, A. Bachmann, T. Lim, K. Kashani, R. Strzoda, and M.-C. Amann, "CO and CH_4 sensing with electrically pumped 2.3μm GaSb-based vertical-cavity surface-emitting laser," in "European Semiconductor Laser Workshop," (2008), p. 20.

- J. Chen, A. Hangauer, R. Strzoda, and M.-C. Amann, "Dynamic wavelength tuning behavior of vertical-cavity surface-emitting lasers," in "Programme and Abstracts, Conference on Semiconductor and Integrated Optoelectronics," (2008), p. 39.

- A. Hangauer, J. Chen, R. Strzoda, and M.-C. Amann, "Accurate measurement of the wavelength modulation phase shift of tunable vertical cavity surface-emitting lasers (VCSELs)," in "Programme and Abstracts, Conference on Semiconductor and Integrated Optoelectronics," (2008), p. 38.

- M. Ortsiefer, J. Rosskopf, E. Rönneberg, Y. Xu, K. Maisberger, R. Shau, C. Neumeyr, W. Hofmann, G. Böhm, A. Hangauer, J. Chen, R. Strzoda, and M.-C. Amann, "Extended near-infrared wavelength VCSELs for optical sensing," in "IEEE/LEOS International Semiconductor Laser Conference," (2008), pp. 167–168.

- A. Hangauer, J. Chen, and M.-C. Amann, "Square-root law thermal response in VCSELs: Experiment and theoretical model," in "Conference on Lasers and Electro Optics (CLEO)," (2008), p. JThA27.

- A. Hangauer, J. Chen, and M.-C. Amann, "Reconstruction of the transmission from n-th harmonic spectra," in "International Conference on Field Laser Applications in Industry and Research," (2007), pp. post–deadline.

- J. Chen, A. Hangauer, R. Strzoda, and M.-C. Amann, "New method based on wavelength modulation spectroscopy for measurement and characterization of the current to wavelength tuning frequency response of VCSELs," in "Book of Abstracts, 6th International Conference on Tunable Diode Laser Spectroscopy," (2007), pp. C–15.

- A. Hangauer, J. Chen, and M.-C. Amann, "Straightforward modeling of the nth harmonic signals used in wavelength modulation spectroscopy and their mathematical properties," in "Book of Abstracts, 6th International Conference on Tunable Diode Laser Spectroscopy," (2007), pp. D–15.

In der Schriftenreihe des Walter Schottky Instituts der Technischen Universität München sind bisher folgende Bände erschienen:

Vol. 1
Cornelia Engel
Si/SiGe basierende Phototransistoren
131 Seiten
ISBN 3-932749-01-4

Vol. 2
Peter Schittenhelm
Selbst-Organisation und Selbst-Ordnung in Si/SiGe-Heterostrukturen
151 Seiten
ISBN 3-932749-02-2

Vol. 3
Andreas Nutsch
Selektive Epitaxie von (GaIn)(AsP) Schichtstrukturen
129 Seiten
ISBN 3-932749-03-0

Vol. 4
Peter Baumgartner
Optische und elektronische Eigenschaften lasergeschriebener GaAs-Nanostrukturen
180 Seiten
ISBN 3-932749-04-9

Vol. 5
Walter Franz Rieger
Untersuchung der elektronischen und strukturellen Eigenschaften von GaNAlN und deren Legierungen
158 Seiten
ISBN 3-932749-05-7

Vol. 6
Markus Hauser
Oberflächenemittierende Laserdioden mit Mehrfachepitaxie
148 Seiten
ISBN 3-932749-06-5

Vol. 7
Markus Sexl
Verspannte und gitterrelaxierte In(GaAl)As Heterostrukturen
144 Seiten
ISBN 3-932749-07-3

Vol. 8
Christian Obermüller
Photolumineszenszspektroskopie mit optischen Nahfeldmethoden an GaAs-Nanostrukturen
140 Seiten
ISBN 3-932749-08-1

Vol. 9
Edilson Silveira
Inelastische Lichtstreuung an niedrig-dimensionalen Halbleiterstrukturen
104 Seiten
ISBN 3-932749-09-X

Vol. 10
Eberhard Christian Rohrer
Photoleitungs-Spektroskopie von Diamant
153 Seiten
ISBN 3-932749-10-03

Vol. 11
Thomas Wimbauer
Magnetische Resonanz-Untersuchungen an modernen Halbleitermaterialien
125 Seiten
ISBN 3-932749-11-1

Vol. 12
Herbert Verhoeven
Thermische Eigenschaften von CVD-Diamantschichten
154 Seiten
ISBN 3-932749-12-X

Vol. 13
Hans-Christoph Ostendorf
Trennung von Volumen- und Oberflächenrekombination in Silizium
128 Seiten
ISBN 3-932749-13-8

Vol. 14
Martin Städele
Dichtefunktionaltheorie mit exaktem Austausch für Halbleiter
202 Seiten
ISBN 3-932749-14-6

Vol. 15
Helmut Angerer
Herstellung von Gruppe III-Nitriden mit Molekularstrahlepitaxie
144 Seiten
ISBN 3-932749-15-4

Vol. 16
Wolfgang Heller
Spektroskopie einzelner Quantenpunkte in magnetischen und elektrischen Feldern
128 Seiten
ISBN 3-932749-16-2

Vol. 17
Molela Moukara
Pseudopotentiale mit exaktem Austausch
117 Seiten
ISBN 3-932749-17-0

Vol. 18
Ralph Oberhuber
Elektronische Struktur und Transport in verspannten Halbleiterschichtsystemen
110 Seiten
ISBN 3-932749-18-9

Vol. 19
Reiner Pech
High-Energy Boron-Implantation into Different Silicon Substrates
158 Seiten
ISBN 3-932749-19-7

Vol. 20
Christoph Martin Engelhardt
Zyklotronresonanz zweidimensionaler Ladungsträgersysteme in Halbleitern, Effekte der Elektron-Elektron-Wechselwirkung und Lokalisierung
317 Seiten
ISBN 3-932749-20-0

Vol. 21
Eduard Neufeld
Erbium-dotierte Si/SiGe-Lichtemitter und -Wellenleiter
136 Seiten
ISBN 3-932749-21-9

Vol. 22
Gert Schedelbeck
Optische Eigenschaften von Halbleiternanostrukturen hergestellt durch Überwachsen von Spaltflächen
154 Seiten
ISBN 3-932749-22-7

Vol. 23
Jürgen Zimmer
Optoelektronisches Verhalten von Dünnschichtbauelementen aus amorphem und mikrokristallinem Silizium
171 Seiten
ISBN 3-932749-23-5

Vol. 24
Berthold Schmidt
Leistungsoptimierung abstimmbarer InGaAsP/InP Halbleiterlaser
85 Seiten
ISBN 3-932749-24-3

Vol. 25
Jianhong Zhu
Ordering of self-assembled Ge and SiGe nanostructures on vicinal Si surfaces
120 Seiten
ISBN 3-932749-25-1

Vol. 26
Gerhard Groos
Herstellung und Charakterisierung von Silizium-Nanostrukturen
168 Seiten
ISBN 3-932749-26-X

Vol. 27
Uwe Hansen
Theorie der Reaktionskinetik an Festkörperoberflächen
119 Seiten
ISBN 3-932749-27-8

Vol. 28
Roman Dimitrov
Herstellung und Charakterisierung von AlGaN/GaN-Transistoren
196 Seiten
ISBN 3-932749-28-6

Vol. 29
Martin Eickhoff
Piezowiderstandsmechanismen in Halbleitern mit großer Bandlücke
151 Seiten
ISBN 3-932749-29-4

Vol. 30
Nikolai Wieser
Ramanspektroskopie an Gruppe III-Nitriden
161 Seiten
ISBN 3-932749-30-8

Vol. 31
Rainer Janssen
Strukturelle und elektronische Eigenschaften amorpher Silizium-Suboxide
275 Seiten
ISBN 3-932749-31-6

Vol. 32
Martin W. Bayerl
Magnetic resonance investigations of group III-nitrides
155 Seiten
ISBN 3-932749-32-4

Vol. 33
Martin Rother
Elektronische Eigenschaften von Halbleiternanostrukturen hergestellt durch Überwachsen von Spaltflächen
196 Seiten
ISBN 3-932749-33-2

Vol. 34
Frank Findeis
Optical spectroscopy on single self-assembled quantum dots
156 Seiten
ISBN 3-932749-34-0

Vol. 35
Markus Ortsiefer
Langwellige Vertikalresonator-Laser-dioden im Materialsystem InGaAlAs/InP
152 Seiten
ISBN 3-932749-35-9

Vol. 36
Roland Zeisel
Optoelectronic properties of defects in diamond and AlGaN alloys
140 Seiten
ISBN 3-932749-36-7

Vol. 37
Liwen Chu
Inter- und Intraband Spektroskopie an selbstorganisierten In(Ga)As/GaAs Quantenpunkten
124 Seiten
ISBN 3-932749-37-5

Vol. 38
Christian Alexander Miesner
Intra-Valenzbandspektroskopie an SiGe-Nanostrukturen in Si
100 Seiten
ISBN 3-932749-38-3

Vol. 39
Szabolcs Kátai
Investigation of the nucleation process of chemical vapour deposited diamond films
178 Seiten
ISBN 3-932749-39-1

Vol. 40
Markus Arzberger
Wachstum, Eigenschaften und Anwendungen selbstorganisierter InAs-Quantenpunkte
236 Seiten
ISBN 3-932749-40-5

Vol. 41
Markus Oliver Markmann
Optische Eigenschaften von Erbium in $Si/Si_{1-x}C_x$, $Si/Si_{1-x}Ge_x$ und Si/SiO_x Heterostrukturen
182 Seiten
ISBN 3-932749-41-3

Vol. 42
Rainer Alexander Deutschmann
Two dimensional electron systems in atomically precise periodic potential
210 Seiten
ISBN 3-932749-42-1

Vol. 43
Uwe Karrer
Schottky-Dioden auf Galliumnitrid: Eigenschaften und Anwendungen in der Sensorik
182 Seiten
ISBN 3-932749-43-X

Vol. 44
Günther Anton Johann Vogg
Epitaxial thin films of Si and Ge based Zintl phases and sheet polymers
169 Seiten
ISBN 3-932749-44-8

Vol. 45
Christian Strahberger
Vertikaler Transport und extreme Magnetfelder in Halbleitern
167 Seiten
ISBN 3-932749-45-6

Vol. 46
Jan Schalwig
Feldeffekt-Gassensoren und ihre Anwendung in Abgas-nachbehandlungssystemen
125 Seiten
ISBN 3-932749-46-4

Vol. 47
Christopher Eisele
Novel absorber structures for Si-based thin film solar cells
126 Seiten
ISBN 3-932749-47-2

Vol. 48
Stefan Hackenbuchner
Elektronische Struktur von Halbleiter-Nanobauelementen im thermodynamischen Nichtgleichgewicht
213 Seiten
ISBN 3-932749-48-0

Vol. 49
Andreas Sticht
Herstellung und Charakterisierung von dünnen Silizium/Siliziumoxid-Schichtsystemen
166 Seiten
ISBN 3-932749-49-9

Vol. 50
Giuseppe Scarpa
Design and fabrication of Quantum Cascade Lasers
193 Seiten
ISBN 3-932749-50-2

Vol. 51
Jörg Frankenberger
Optische Untersuchungen an zwei-dimensionalen Ladungsträgersystemen
158 Seiten
ISBN 3-932749-51-0

Vol. 52
Doris Heinrich
Wavelength selective optically induced charge storage in self-assembled semiconductor quantum dots
144 Seiten
ISBN 3-932749-52-9

Vol. 53
Nicolaus Ulbrich
Entwurf und Charakterisierung von Quanten-Kaskadenlasern und Quantenpunktkaskaden
133 Seiten
ISBN 3-932749-53-7

Vol. 54
Lutz Carsten Görgens
Analyse stickstoffhaltiger III-V Halbleiter-Heterosysteme mit hochenergetischen schweren Ionen
116 Seiten
ISBN 3-932749-54-5

Vol. 55
Andreas Janotta
Doping, light-induced modification and biocompatibility of amorphous silicon suboxides
180 Seiten
ISBN 3-932749-55-3

Vol. 56
Sebastian Tobias Benedikt Gönnenwein
Two-dimensional electron gases and ferromagnetic semiconductors: materials for spintronics
198 Seiten
ISBN 3-932749-56-1

Vol. 57
Evelin Beham
Photostromspektroskopie an einzelnen Quantenpunkten
186 Seiten
ISBN 3-932749-57-X

Vol. 58
Po-Wen Chiu
Towards carbon nanotube-based molecular electronics
116 Seiten
ISBN 3-932749-58-8

Vol. 59
Tobias Graf
Spin-spin interactions of localized electronic states in semiconductors
194 Seiten
ISBN 3-932749-59-6

Vol. 60
Stefan Klein
Microcrystalline silicon prepared by hot wire CVD: preparation and characterisation of material and solar cells
157 Seiten
ISBN 3-932749-60-X

Vol. 61
Markus Krach
Frequenzverdreifacher mit Anti-Seriellem Schottky-Varaktor für den Terahertzbereich
156 Seiten
ISBN 3-932749-61-8

Vol. 62
Ralph Thomas Neuberger
AlGaN/GaN-Heterostrukturen als chemische Sensoren in korrosiven Medien
153 Seiten
ISBN 3-932749-62-6

Vol. 63
Sonia Perna
Wasserstoff-Passivierung von trikristallinem Silizium durch hydrogenisiertes Siliziumnitrid
136 Seiten
ISBN 3-932749-63-4

Vol. 64
Oliver Schumann
Einfluss von Stickstoff auf das Wachstum und die Eigenschaften von InAs-Quantenpunkten
148 Seiten
ISBN 3-932749-64-2

Vol. 65
Gerhard Rösel
Entwicklung und Charakterisierung von Typ-II-Heterostrukturen für die Abstimmregion in abstimmbaren Laserdioden
101 Seiten
ISBN 3-932749-65-0

Vol. 66
Angela Link
Zweidimensionale Elektronen- und Löcher-Gase in GaN/AlGaN Heterostrukturen
156 Seiten
ISBN 3-932749-66-9

Vol. 67
Matthias Sabathil
Opto-electronic and quantum transport properties of semiconductor nanostructures
156 Seiten
ISBN 3-932749-67-7

Vol. 68
Frank Fischer
Growth and electronic properties of two-dimensional systems on (110) oriented GaAs
139 Seiten
ISBN 3-932749-68-5

Vol. 69
Robert Shau
Langwellige oberflächenemittierende Laserdioden mit hoher Ausgangsleistung und Modulationsbandbreite
198 Seiten
ISBN 3-932749-69-3

Vol. 70
Andrea Baumer
Structural and electronic properties of hydrosilylated silicon surfaces
163 Seiten
ISBN 3-932749-70-7

Vol. 71
Andreas Florian Kreß
Manipulation of the Light-Matter-Interaction in Photonic Crystal Nanocavities
185 Seiten
ISBN 3-932749-71-5

Vol. 72
Markus Grau
Molekularstrahlepitaktische Herstellung von antimonidischen Laserdioden für die Gassensorik
138 Seiten
ISBN 3-932749-72-3

Vol. 73
Karin Buchholz
Microprocessing of silicon on insulator substrates and biofunctionalisation of silicon dioxide surfaces for sensing applications in fluids
170 Seiten
ISBN 3-932749-73-1

Vol. 74
Dominique Bougeard
Spektroskopische Charakterisierung von Germanium-Quantenpunkten in Silizium
154 Seiten
ISBN 3-932749-74-X

Vol. 75
Jochen Bauer
Untersuchungen zum kontrollierten Wachstum von InAs-Nanostrukturen auf Spaltflächen
140 Seiten
ISBN 3-932749-75-8

Vol. 76
Ingo Bormann
Intersubband Spektroskopie an Silizium-Germanium Quantenkaskadenstrukturen
124 Seiten
ISBN 3-932749-76-6

Vol. 77
Hubert Johannes Krenner
Coherent quantum coupling of excitons in single quantum dots and quantum dot molecules
160 Seiten
ISBN 3-932749-77-4

Vol. 78
Ulrich Rant
Electrical manipulation of DNA-layers on gold surfaces
249 Seiten
ISBN 3-932749-78-2

Vol. 79
René Todt
Widely tunable laser diodes with distributed feedback
152 Seiten
ISBN 3-932749-79-0

Vol. 80
Miroslav Kroutvar
Charge and spin storage in quantum dots
150 Seiten
ISBN 3-932749-80-4

Vol. 81
Markus Maute
Mikromechanisch abstimmbare Laser-Dioden mit Vertikalresonator
170 Seiten
ISBN 3-932749-81-2

Vol. 82
Frank Ertl
Anisotrope Quanten-Hall-Systeme, Vertikale Ultrakurzkanal- und Tunneltransistoren
170 Seiten
ISBN 3-932749-82-0

Vol. 83
Sebastian M. Luber
III-V semiconductor structures for biosensor and molecular electronics applications
212 Seiten
ISBN 978-3-932749-83-4

Vol. 84
Claudio Ronald Miskys
New substrates for epitaxy of group III nitride semiconductors: challenges and potential
207 Seiten
ISBN 978-3-932749-84-1

Vol. 85
Sebastian Friedrich Roth
n- and p-type transport in (110) GaAs substrates, single- and double-cleave structures
138 Seiten
ISBN 978-3-932749-85-8

Vol. 86
Mario Gjukic
Metal-induced crystallization of silicon-germanium alloys
309 Seiten
ISBN 978-3-932749-86-5

Vol. 87
Tobias Zibold
Semiconductor based quantum information devices: Theory and simulations
151 Seiten
ISBN 978-3-932749-87-2

Vol. 88
Thomas Jacke
Weit abstimmbare Laserdiode mit vertikal integriertem Mach-Zehnder-Interferometer
165 Seiten
ISBN 978-3-932749-88-9

Vol. 89
Nenad Ocelić
Quantitative near-field phonon-polariton spectroscopy
174 Seiten
ISBN 978-3-932749-89-6

Vol. 90
Kenji Arinaga
Control and manipulation of DNA on gold and its application for biosensing
111 Seiten
ISBN 978-3-932749-90-2

Vol. 91
Hans-Gregor Hübl
Coherent manipulation and electrical detection of phosphorus donor spins in silicon
162 Seiten
ISBN 978-3-932749-91-9

Vol. 92
Andrea Friedrich
Quanten-Kaskaden-Laser ohne Injektorbereiche
140 Seiten
ISBN 978-3-932749-92-6

Vol. 93
Oliver Dier
Das Materialsystem (AlGaIn) (AsSb): Eigenschaften und Eignung für GaSb-basierte Vertikalresonator-Laserdioden
174 Seiten
ISBN 978-3-932749-93-3

Vol. 94
Georg Steinhoff
Group III-nitrides for bio- and electrochemical sensors
197 Seiten
ISBN 978-3-932749-94-0

Vol. 95
Stefan Harrer
Next-generation nanoimprint lithography: Innovative approaches towards improving flexibility and resolution of nanofabrication in the sub-15-nm region
161 Seiten
ISBN 978-3-932749-95-7

Vol. 96
Stefan Ahlers
Magnetic and electrical properties of epitaxial GeMn
184 Seiten
ISBN 978-3-932749-96-0

Vol. 97
Emanuele Uccelli
Guided self-assembly of InAs quantum dots arrays on (110) surfaces
172 Seiten
ISBN 978-3-932749-97-1

Vol. 98
Shavaji Dasgupta
Growth optimization and characterization of high mobility two-dimensional electron systems in AlAs quantum wells
152 Seiten
ISBN 978-3-932749-98-8

Vol. 99
Werner Hofmann
InP-based long-wavelength VCSELs and VCSEL arrays for high-speed optical communication
142 Seiten
ISBN 978-3-932749-99-5

Vol. 100
Robert Lechner
Silicon nanocrystal films for electronic applications
227 Seiten
ISBN 978-3-941650-00-8

Vol. 101
Nebile Işık
Investigation of Landau level spin reversal in (110) oriented p-type GaAs quantum wells
114 Seiten
ISBN 978-3-941650-01-5

Vol. 102
Andreas Florian Härtl
Novel concepts for biosensors using diamond-based field effect transistors
255 Seiten
ISBN 978-3-941650-02-2

Vol. 103
Felix Florian Georg Hofbauer
Realization of electrically tunable single quantum dot nanocavities
160 Seiten
ISBN 978-3-941650-03-9

Vol. 104
Dominic F. Dorfner
Novel photonic biosensing based on silicon nanostructures
169 Seiten
ISBN 978-3-941650-04-6

Vol. 105
Till Andlauer
Optoelectronic and spin-related properties of semiconductor nanostructures in magnetic fields
157 Seiten
ISBN 978-3-941650-05-3

Vol. 106
Christoph Bihler
Magnetic semiconductors
190 Seiten
ISBN 978-3-941650-06-0

Vol. 107
Michael Huber
Tunnel-Spektroskopie im Quanten-Hall-Regime
164 Seiten
ISBN 978-3-941650-07-7

Vol. 108
Philipp Achatz
Metal-insulator transition and super-Conductivity in heavily boron-doped diamond and related materials
151 Seiten
ISBN 978-3-941650-08-4

Vol. 109
Sebastian Strobel
Nanoscale contacts to organic molecules based on layered semiconductor substrates
140 Seiten
ISBN 978-3-941650-09-1

Vol. 110
Ying Xiang
Semiconductor nanowires and templates for electronic applications
152 Seiten
ISBN 978-3-941650-10-7

Vol. 111
Michael Kaniber
Non-classical light generation in photonic crystal nanostructures
177 Seiten
ISBN 978-3-941650-11-4

Vol. 112
Martin Hermann
Epitaktische AlN-Schichten auf Saphir und Diamant
216 Seiten
ISBN 978-3-941650-12-1

Vol. 113
Dominik Heiss
Spin storage in quantum dot ensembles and single quantum dots
196 Seiten
ISBN 978-3-941650-13-8

Vol. 114
Tillmann Christoph Kubis
Quantum transport in semiconductor nanostructures
253 Seiten
ISBN 978-3-941650-14-5

Vol. 115
Lucia Steinke
Magnetotransport of coupled quantum Hall edges in a bent quantum well
194 Seiten
ISBN 978-3-941650-15-2

Vol. 116
Christian Lauer
Antimonid-basierte Vertikalresonator-Laserdioden für Wellenlängen oberhalb 2 µm
180 Seiten
ISBN 978-3-941650-16-9

Vol. 117
Simone Maria Kaniber
Optoelektronische Phänomene in hybriden Schaltkreisen aus Kohlenstoffnanoröhren und dem Photosystem I
136 Seiten
ISBN 978-3-941650-17-6

Vol. 118
Martin Heiß
Growth and properties of low-dimensional III-V semiconductor nanowire heterostructures
172 Seiten
ISBN 978-3-941650-18-3

Vol. 119
Sandro Francesco Tedde
Design, fabrication and characterization of organic photodiodes for industrial and medical applications
277 Seiten
ISBN 978-3-941650-19-0

Vol. 120
Danche Spirkoska Jovanov
Fundamental properties of self-catalyzed GaAs nanowires and related heterostructures
200 Seiten
ISBN 978-3-941650-20-6

Vol. 121
Jürgen Sailer
Materials and devices for quantum Information processing in Si/SiGe
158 Seiten
ISBN 978-3-941650-21-3

Vol. 122
Ilaria Zardo
Growth and raman spectroscopy studies of gold-free catalyzed semiconductor nanowires
184 Seiten
ISBN 978-3-941650-22-0

Vol. 123
Andre Rainer Stegner
Shallow dopants in nanostructured and in isotopically engineered silicon
185 Seiten
ISBN 978-3-941650-23-7

Vol. 124
Andreas J. Huber
Nanoscale surface-polariton spectroscopy by mid- and far-infrared near-field microscopy
144 Seiten
ISBN 978-3-941650-24-4

Vol. 125
Marco Andreas Höb
Funktionalisierung von Gruppe IV-Halbleitern
186 Seiten
ISBN 978-3-941650-25-1

Vol. 126
Daniel Claudio Pedone
Nanopore analytics – electro-optical studies on single molecules
114 Seiten
ISBN 978-3-941650-26-8

Vol. 127
Casimir Richard Simeon Katz
Multi-alloy structures for injectorless Quantum Cascade Lasers
131 Seiten
ISBN 978-3-941650-27-5

Vol. 128
Barbara Annemarie Kathrin Baur
Functionalization of group III-nitrides for biosensor applications
215 Seiten
ISBN 978-3-941650-28-2

Vol. 129
Arne Laucht
Semiconductor quantum optics with tailored photonic nanostructures
232 Seiten
ISBN 978-3-941650-29-9

Vol. 130
Jia Chen
Compact laser-spectroscopic gas sensors using Vertical-Cavity Surface-Emitting Lasers
150 Seiten
ISBN 978-3-941650-30-5